Integratie van hartklepbeweging in patiënt-specifieke numerieke simulaties van de bloedstroming in het menselijk hart: strategieën en uitdagingen

Integrating Valve Leaflet Motion into Patient-Specific Numerical Blood Flow Simulations of the Human Heart: Strategies and Challenges

Alessandra M. Bavo

Promotoren: Prof. dr. ir. P. Segers, Prof. dr. ir. J. Vierendeels, Prof. dr. ir. J. Degroote
Proefschrift ingediend tot het behalen van de graad van
Doctor in de Ingenieurswetenschappen: Biomedische Ingenieurstechnieken

Vakgroep voor Elektronica en Informatiesystemen
Voorzitter: Prof. dr. ir. Rik Van de Walle
Faculteit Ingenieurswetenschappen en Architectuur
Academiejaar 2016-2017

UNIVERSITEIT GENT

Supervisors:

Prof. dr. ir. Patrick Segers
Prof. dr. ir. Jan Vierendeels
Prof. dr. ir. Joris Degroote

Research lab:

Institute Biomedical Technology
Biofluid, Tissue and Solid Mechanics for Medical Applications (bioMMeda)
Ghent University
De Pintelaan 185 - Blok B
B–9000 Gent
Belgium

Members of the exam committee:

Chairman:	
Prof. dr. ir. Daniel De Zutter	Faculty of Engineering and Architecture, UGent
Secretary:	
Prof. dr. ir. Peter Troch	Faculty of Engineering and Architecture, UGent
Reading committee:	
Prof. dr. ir. Raoul Van Loon	Swansea University, United Kingdom
Prof. dr. ir. Alberto Redaelli	Politecnico di Milano, Italy
Prof. dr. ir. Peter Troch	Faculty of Engineering and Architecture, UGent
Other members:	
Prof. dr. Pascal Verdonck	Faculty of Engineering and Architecture, UGent
Dr. ir. Gianluca De Santis	FEops bvba, Ghent, Belgium
Prof. dr. Ernst Rietzschel	Faculty of Medicine and Health Science, UGent

Just because something doesn't do what you

planned it to do, doesn't mean it's useless.

Thomas A. Edison

Preface

The story of how I came to Ghent for a PhD is known to anybody who spent more than two minutes talking to me in the last four years. So, I will tell it once more.

"Once upon a time, there was a young student doing her Master thesis in London, when, by chance, for a lucky coincidence or for some other reasons, she found out that Professor Segers (who she knew from her Erasmus in Gent) was coming to her lab in the UK for a symposium. In less than an hour, she managed to talk to her thesis supervisor and set up a meeting, and this is how I got here".

After four years of PhD, there is a long list of people I need to thank.
In the first place, I want to thank Patrick for believing in me from the first moment, without even knowing me. Next to the scientific guidance, extremely fast proof-reading of text, papers and presentations, he supported me during all these not-always-easy four years. Even when difficulties seemed to be too big, he always had few minutes to listen to my complaints and had his optimistic approach to push me forward to the solution.
Probably not even half of this work would have been possible without Jan and Joris. I would to thank Jan for the very productive talks and discussions we had over my work. His great technical knowledge and critical mind were of fundamental importance in the understanding of all the non-obvious results I obtained in these years (and there were many). Of my three co-promoters, I think Joris is the one I mentioned the most when talking to my family. I want to thank him for his worldwide and almost 24/7 support for technical troubles, brainstorming sessions and discussions when my research was stuck.
Thanks to Alison from the Gorman's research group for hosting me 6 months at UPenn and providing me with the data I needed for my work.
Thanks to Saskia for the administrative support, thanks to her efficiency Belgian bureaucracy scares me a little bit less.

Thanks to the jury members of this PhD committee for their interest in this work, their comments and suggestions.
Thanks also to my thesis students, Giorgia and Celine, who taught me how to communicate to other people my technical knowledge in a (hopefully) understandable manner.

Thanks to all my past and present colleagues of bioMMeda, especially the members of the awesome office, Margo, Daniela, Danilo, Darya, Giorgia, Hisham, David, Giuseppe, Wouter and Liesbeth for the endless talks, the birthday cakes, chocolate and the rain in the office. The life in the office would have been very boring without you. A special thanks goes to Danilo, for all the dinners, talks, trips, the Caribbean sun and the mathematical support.

I want to thank my Gentenaar friends, Dagmara, Marlet, Jaime, Ali, Kristof, Piotr, Sibel and all the others, it is because of them if I am still here and I learned to like Belgium. Thanks also to my Italian friends, who are still there even if we barely see each other. Thanks to Rossella, Claudia, Vale and Federico who don't mind about the distance and every time we talk it looks like we saw each other the day before.

Per finire, vorrei ringraziare la mia famiglia, nonni, zii e parenti, per essermi sempre stati (virtualmente) vicini anche se in realtà nessuno avesse ben capito quel che sono andata a fare in Belgio. Grazie in particolare ai miei genitori e al Fra, per aver sempre creduto in me, per avermi supportato in tutto questo tempo nonostante la distanza e le difficoltà. Senza di loro non avrei mai potuto fare quel che ho fatto ed essere quello che sono.

Last but not least, grazie a Davide, per una lunghissima serie di motivi che non verrà riportata qui. Grazie per la costanza e la pazienza di voler affrontare la distanza (grazie Ryanair!), grazie perchè sopportare tutti i giorni una che deve finire il PhD non è cosa da poco.

Ale
Gent, December 2016

Samenvatting
Summary

Samenvatting

Inleiding

Cardiovasculaire aandoeningen zijn wereldwijd de meest voorkomende doodsoorzaak. Bij vele van deze aandoeningen speelt de dynamica van de bloedstroming (i.e. de hemodynamica) een cruciale rol in het ziekteproces en deze wordt idealiter mee in acht genomen bij de diagnose en in de behandeling van de ziekte. De beschikbare beeldvormingstechnieken zoals computed tomography (CT), magnetic resonance imaging (MRI) en ultrageluid zijn vaak niet in staat om het stromingsveld in voldoende detail te visualiseren en kwantificeren. Numerieke stromingsdynamica (computational fluid dynamics (CFD)) technieken in combinatie met medische beeldvorming laten toe om meer gedetailleerde kwantitatieve informatie te bekomen over de hemodynamica. Een bijkomend voordeel van computersimulaties is dat ze de mogelijkheid bieden om andere condities te bestuderen dan die van de patiënt op het ogenblik waarop de meting werd uitgevoerd. Deze simulaties bieden dan ook interessante mogelijkheden in de planning van procedures, het individualiseren van de behandeling, het ontwerp van medische hulpmiddelen et cetera.

In toepassingen waarbij de hartkleppen in beschouwing dienen genomen te worden, staan technische uitdagingen nog steeds de berekening van patiënt-specifieke stromingsvelden in de weg. De krachten en spanningen die de bloedstroming op de klepblaadjes uitoefent, veroorzaakt de beweging van de klepblaadjes van de natuurlijke (of kunstmatige) hartklep en dit is een typisch voorbeeld van een fluïdum-structuur interactie fluid-structure interaction (FSI) vraagstuk. Een dergelijk vraagstuk numeriek oplossen is zeer uitdagend omwille van, onder andere, de zeer complexe geometrie en materiaaleigenschappen van de klepbladen, de grote bewegingen waaraan deze onderworpen zijn, de complexe kinematica en het contact van de klepbladen. In deze thesis zullen we (i) een systematische en diepgaande vergelijking maken van twee verschillende FSI modelleringstechnieken die gebruikt

kunnen worden om de stroming door een aortaklep te simuleren en (ii) een nieuwe methodologie en CFD model voorstellen om intraventriculaire en transmitrale stroming te beschrijven waarbij de beweging van het ventrikel en de mitralisklep worden voorgeschreven op basis van data bekomen uit three-dimensional (3D) gesegmenteerde (slokdarm) ultrageluidbeelden.

De 3 belangrijkste onderzoeksdoelen zijn:

1. *Een evaluatie maken van de haalbaarheid van een arbitrary Lagrangian-Eulerian (ALE) aanpak voor FSI simulaties van bloedstroming door de aortaklep en een inschatting maken van de impact op de resultaten;*

2. *Een nieuwe techniek ontwikkelen voor CFD simulaties waarbij de bewegende grenzen van het stromingsdomein voorgeschreven worden op basis van patiënt-specifiek ultrageluidbeelden met als doel de intraventriculaire hemodynamica te bestuderen;*

3. *Het aantonen van het klinisch potentieel en relevantie van de modellen door deze te testen op verschillende patiënt-specifieke casussen.*

Na het eerste, inleidende deel waarin vooral de achtergrond van dit werk gesitueerd wordt, bestaat de hoofdtekst van deze thesis uit twee delen (II en III). Hieronder staat een korte samenvatting van elk deel en hoofdstuk als leidraad voor de lezer van deze thesis.

Deel 1: Achtergrond

Hoofdstuk 1: Het menselijk hart

Het onderzoeksgebied van deze thesis is breed maar is hoofdzakelijk gefocust of het modelleren en simuleren van hartkleppen en intraventriculaire bloedstroming. Om de klinische achtergrond van dit werk te verduidelijken wordt in het eerste hoofdstuk een basis gegeven van de anatomie, fysiologie en pathologie van het humane hart en zijn onderdelen. De complexiteit en werking van de hartkleppen (meer specifiek de mitralis- en aortakleppen) en van het linkerventrikel worden eveneens beschreven. De meest voorkomende aandoeningen van de hartkleppen worden besproken evenals een beknopt overzicht van de beschikbare klepprothesen. Aangezien aandoeningen van de hartkleppen vaak gepaard gaan met een cardiomyopathie wordt eveneens een kort overzicht van de meest voorkomende hartaandoeningen gegeven.

Hoofdstuk 2: Numerieke methodes en strategieën voor simulatie van intracardiale en transvasculaire bloedstroming

Aangezien numerieke simulaties het hoofdonderwerp zijn van deze thesis, wordt in dit hoofdstuk een overzicht geven van de belangrijkste technieken die gebruikt worden om de stromingsdynamica van het cardiovasculair systeem te berekenen. Bij volwaardige FSI simulaties van de aortakleppen wordt de beweging van de kleppen bekomen door de koppeling van het fluïdum en structureel domein zodanig dat ten allen tijde een evenwicht van de spanningen en verplaatsingen ter hoogte van het contact tussen beide domeinen wordt bereikt. Een andere aanpak om intraventriculaire stroming te bestuderen bestaat uit het gebruik van een CFD analyse waarbij de beweging van de vervormbare structuren wordt voorgeschreven op basis van a priori bekomen medische beelden. De verschillende technieken die gebruik worden om het fluïdumrooster te discretizeren worden eveneens besproken en hun respectievelijke voor- en nadelen worden in meer detail besproken. Deze samenvatting heeft niet de ambitie om een volledig naslagwerk te zijn, maar eerder om de essentiële achtergrond te voorzien die nodig is om de onderwerpen besproken in deze thesis te begrijpen.

Deel 2: Fluïdum-structuur interactie simulaties op bioprosthetische aortakleppen

Hoofdstuk 3: FSI simulaties van de aortaklep

In de voorbije jaren werden een aantal numerieke simulatie studies uitgevoerd om geïdealiseerde, natuurlijke of kunstmatige aortakleppen te bestuderen. Hoofdstuk 3 biedt een overzicht van de tweedimensionale en driedimensionale modellen die in de literatuur gebruikt werden om de FSI simulaties van aortakleppen uit te voeren. Binnen de context van dit werk zal dit literatuuroverzicht zich vooral focussen op de details in verband met de discretisatie van het rekenrooster waarbij extra aandacht wordt geschonken aan de keuzes die hieromtrent gemaakt werden in de verschillende FSI studies. Wanneer beschikbaar en relevant, zullen ook de resultaten van de druk, het stromingsveld en de wandschuifspanning op de klep gerapporteerd worden.

Hoofdstuk 4: Vergelijking tussen de IB en ALE

Bij het opzetten van een FSI simulatie dienen enkele beslissingen gemaakt te worden zodanig dat de meest geschikte aanpak voor elk

individueel geval wordt gekozen. Bij het simuleren van flexibele hartklepblaadjes is het bijvoorbeeld van groot belang welk type discretisatie voor het fluïdum domein wordt gebruikt. Deze discretisatie kan beschreven worden aan de hand van een ALE of Euleriaanse formulering. Het gebruik van de ALE techniek heeft voordelen gerelateerd aan de theoretische precisie van de resultaten, zeker in de nabijheid van de bewegende oppervlakken. De drukken en de wandschuifspanningen in het bijzonder zijn meer accuraat wanneer ze berekend worden met de ALE techniek. Deze techniek heeft echter het nadeel dat wanneer er grote vervormingen optreden, zoals het geval is bij de hartkleppen, het fluïdum rekenrooster zwaar verstoord kan worden. Dit is het tegenovergestelde van de Euleriaanse techniek waarbij geen problemen met de roosterbeweging zijn, maar de nauwkeurigheid in druk en wandschuifspanning lager zijn.

In dit hoofdstuk worden de resultaten van twee FSI simulaties op dezelfde aortaklep, maar met andere fluïdum discretisatie schema's vergeleken om de performantie van een ALE-gebaseerde FSI oplossing te vergelijken met die van een Euleriaanse FSI oplossing. Deze vergelijking werd in 2D en 3D uitgevoerd. In 2D konden geen significante verschillen aangetoond worden tussen beide methodes. In 3D daarentegen belemmerden technische moeilijkheden betrouwbare resultaten voor de aortaklepsimulaties voor zowel een ALE als een immersed boundary (IB) formulering. De belangrijkste hindernis in de 3D arbitrary Lagrangian-Eulerian Fluïdum-Structuur Interactie (arbitrary Lagrangian-Eulerian fluid-structure interaction (ALE-FSI)) is te wijten aan de grote vervorming van het fluïdum domein. Voor de 3D Immersed Boundary Fluïdum-Structuur Interactie (immersed boundary fluid-structure interaction (IB-FSI)), zijn de beperkingen gerelateerd aan de keuze van het programma. Het bleek namelijk niet mogelijk om de volledige test te simuleren zolang het programma (nog) niet geoptimaliseerd is en er werden moeilijkheden vastgesteld zowel bij het opleggen van het fluïdum-structuur contact als bij het definiëren van de zogenaamde volume-of-fluid functie. De voor- en nadelen van beide technieken worden in dit hoofdstuk nog eens vermeld samen met hun belangrijkste beperkingen en de onderliggende hypotheses en benaderingen worden benadrukt en besproken.

Hoofdstuk 5: Analyse van de samendrukbaarheid en andere mogelijke oorzaken van suboptimale resultaten in FSI simulaties

Een van de belangrijkste veronderstellingen waarop de simulaties van hoofdstuk 4 steunen is de invoering van een artificiële samendrukbaarheid in de FSI simulaties. Deze hypothese geldt zowel wanneer de

IB als de ALE techniek gebruikt wordt, maar in beide gevallen voor verschillende redenen.

In het geval van de IB-FSI techniek wordt een kleine hoeveelheid samendrukbaarheid van het fluïdum toegestaan om de berekening te stabiliseren en te versnellen. In dit hoofdstuk worden enkele uitgevoerde testen beschreven waarmee nagegaan werd of de invoering van de samendrukbaarheid een invloed had op de resultaten van de simulaties. Deze bijkomende testen werden uitgevoerd aangezien de geïntroduceerde waarden van de samendrukbaarheid groter waren dan de in literatuur gerapporteerde waarden. Anderzijds werd nagegaan of de vertraging bij het openen van de klep (in het geval van de IB) kon gerelateerd worden aan de samendrukbaarheid of een andere reden aan de basis lag van dit fenomeen. De tests toonden aan dat de geïntroduceerde samendrukbaarheid geen sterke invloed had op de resultaten van de simulatie bij het gebruik van de IB-FSI techniek. De geobserveerde vertraging kan toegeschreven worden aan andere fenomenen dan de samendrukbaarheid: ten eerste leidt het gebruik van een enkele laag lineaire continuüm elementen tot een toegenomen buigstijfheid van de klep. Ten tweede is de randvoorwaarde van gelijke snelheid (opgelegd voor het contact algoritme) tussen het fluïdum en het vast domein ter hoogte van het contact niet optimaal en zorgt deze voor oscillaties met hoge frequentie en de waargenomen vertraging bij het begin van de simulatie.

In het geval van een ALE-FSI simulatie kan de samendrukbaarheid gebruikt worden in de fluïdum solver om de onsamendrukbaarheid hypothese tijdelijk te omzeilen. Hierdoor kunnen oscillaties in het drukveld omwille van de grote verplaatsingen van de structuur vermeden worden en kan de numerieke tijdstap verkleind worden. De samendrukbaarheid die geïntroduceerd wordt in de ALE casussen verdwijnt van zodra de koppelingsiteraties ter hoogte van het contact geconvergeerd zijn, waardoor deze geen effect heeft op de uiteindelijke resultaten. De toevoeging van de artificiële samendrukbaarheid in de 3D ALE-FSI simulatie had echter geen positieve invloed op de uitkomst van de simulatie aangezien de vervorming van het rooster nog steeds te groot was om deze succesvol uit te voeren.

Deel 3: Numerieke stromingsdynamica simulaties met voorgeschreven wandbeweging

Hoofdstuk 6: Intraventriculaire stroming: visualisatietechnieken en numerieke modellen

De analyse van de intraventriculaire stroming biedt unieke inzichten in de hemodynamica van het hart en heeft het potentieel om de diagnose en de inschatting van de graad van ventriculaire (dys)functie te verbeteren. De verschillende klinische beeldvormingstechnieken die in staat zijn om deze stroming te visualiseren worden kort beschreven in het eerste deel van dit hoofdstuk.

De combinatie en integratie van medische beeldvorming met numerieke stromingsdynamica technieken maakt het mogelijk om patiënt-specifieke modellen te maken die meer gedetailleerde en kwantitatieve informatie kunnen geven over de cardiale hemodynamica die anders niet meetbaar zijn in de patiënt zoals intraventriculaire drukgradiënten, wervels of wandschuifspanningen. In het tweede deel van dit hoofdstuk wordt een overzicht gegeven van de meest gebruikte numerieke technieken voor intraventriculaire stromingsanalyse.

Hoofdstuk 7: Patiënt-specifieke CFD simulaties van de intraventriculaire hemodynamica gebaseerd op 3D ultrageluidbeelden

In hoofdstuk 7 wordt een nieuwe techniek om patiënt-specifieke intraventriculaire stroming gebaseerd op real-time slokdarmechografie beelden (real-time transesophageal echocardiographic images (rt-TEE)) besproken en geïllustreerd aan de hand van een test casus. De volledige procedure werd specifiek ontwikkeld voor bewegende linkerventrikels en mitralisklepblaadjes, te beginnen van de patiënt-specifieke gesegmenteerde ultrageluidbeelden. De gesegmenteerde beelden bepalen de positie van de mitralisklep en het linkerventrikel op discrete tijdspunten in de hartcyclus. In een stap voorafgaand aan de eigenlijke berekening wordt een tijdsinterpolatie uitgevoerd met behulp van een 3de orde spline voor elke punt van de gesegmenteerde oppervlakken zodat de knooppositie in functie van tijd volledig beschreven is. Tijdens de simulaties wordt de verplaatsing van de buitenwand uitgedrukt als een lineaire combinatie van de verplaatsingen van de dichtstbijzijnde punten van de gesegmenteerde oppervlakken. De identificatie van deze dichtstbijzijnde punten, de verplaatsing van de randen en de barycentrische coördinaten worden elke tijdsstap aangepast zodat het eindresultaat voldoende glad is. Bij elke verplaatsing van de buitenwand werd het volume-rekenrooster

navenant aangepast met behulp van een veermodel en het rooster werd deels vervangen indien nodig. Het model werd toegepast op ultrageluidbeelden van een patiënt (met een hypertrofisch ventrikel maar fysiologische ejection fraction (EF)) en de resultaten hiervan worden eveneens in dit hoofdstuk besproken. Ook al werd het model nog niet gevalideerd, toch kan besloten worden dat de resultaten realistisch zijn en in goede overeenstemming met de gediagnoseerde pathologie en zijn typische presentatie. De toegevoegde waarde van het model wordt ook besproken vanuit een methodologisch standpunt.

Hoofdstuk 8: Patiënt-specifieke CFD simulaties van de intraventriculaire hemodynamica gebaseerd op 3D ultrageluidbeelden: vergelijking van 3 klinische casussen

In dit hoofdstuk wordt een uitbreiding van het model beschreven in hoofdstuk 7 gepresenteerd evenals zijn toepassing op 3 verschillende patiëntcasussen. De patiënten werden geselecteerd op basis van de verschillen in de anatomie en functie van het linker hart. De eerste casus betreft een patiënt met een gereduceerd ventrikelvolume maar normale EF. De tweede patiënt heeft eveneens een gereduceerd ventrikelvolume maar hier was ook de EF lager dan de fysiologische EF. In de derde casus tenslotte is het ventrikel gedilateerd en is de EF extreem laag. De Intraventriculaire drukken, snelheden en wervels werden in alle drie de gevallen berekend en de waargenomen verschillen worden in dit hoofdstuk besproken.

Deel 4: Conclusies

Hoofdstuk 9: Conclusies en toekomstperspectieven

De belangrijkste conclusies van dit doctoraat worden samengevat in dit hoofdstuk met een speciale focus op de twee belangrijkste hoofdstukken (II en III).

Er kan op basis van deze conclusies besloten worden dat de drie onderzoeksvragen beantwoord werden. Ten eerste werd een kritische analyse gemaakt van de twee simulatie methodes voor FSI simulaties waarbij de beperkingen en voordelen van beide technieken op een rijtje werden gezet. Ten tweede werd een nieuwe CFD aanpak ontwikkeld die in staat is om intraventriculaire stroming te bestuderen op patiënt-specifieke basis. Het model is gebaseerd op pre-operatieve patiënt-specifieke ultrageluidbeelden en werd volledig geïmplementeerd in een ALE context. Hoewel het model nog verdere validatie vereist, kunnen veelbelovende resultaten in een preliminaire studie gerapporteerd

worden. De analyse bevestigde de toepasbaarheid van het model op verschillende patiënten en was in staat de abnormale stromingsvelden in pathologische ventrikels weer te geven.

Summary

Introduction

Cardiovascular diseases are the leading cause of death worldwide, including both cardiac and vascular disorders. In many of these disorders, the dynamic of blood flow (i.e. the hemodynamics) plays a key role in the patho-physiological process and should be considered in the treatment of the disease. Often, available imaging techniques such as computed tomography (CT), magnetic resonance imaging (MRI) or ultrasound are limited in the capability to visualize and quantify the flow in sufficient detail. To resolve these imaging-related limitations, computational fluid dynamics (CFD) techniques can be used in conjunction with medical imaging to provide detailed quantitative information on the hemodynamics. An additional benefit of computer model simulations is that it allows for the testing of conditions other than the condition of the patient at the moment of measurement, providing options to include fluid mechanical analysis in for instance, treatment planning, individualizing treatment, medical device design, etc.

Technical challenges still hamper the computation of patient-specific flow fields in applications involving heart valves. The leaflets of the native (or prosthetic) heart valves move in response to the forces and stresses exerted on the leaflets by the fluid flow, and are a typical example of an fluid-structure interaction (FSI) problem. Solving this problem numerically is challenging due to the very complex geometry and material properties of the leaflets, their large motion and complex kinematic and their contact, among others. In this PhD thesis, we provide (i) a systematic and in depth comparison of two different FSI modelling strategies to solve the fluid flow through the aortic valve and (ii) a methodology and CFD model for the simulation of intraventricular and transmitral flow with imposed motion of the ventricle and mitral valve leaflets based on three-dimensional (3D) segmented (transoesophageal) ultrasound images.

The main research goals are:

1. *Evaluate the feasibility of the arbitrary Lagrangian-Eulerian (ALE) technique for FSI simulations of blood flow through aortic valves and assess the impact of the modeling choices on the final results;*

2. *Develop a new technique for CFD simulations with prescribed moving boundaries based on patient-specific ultrasound images to study intraventricular hemodynamics;*

3. *Demonstrate the potential clinical use and relevance of such a model by testing it on different patient-specific cases.*

After the first part with the background, the main body of this thesis is conceptually subdivided in two parts (II and III). In the following, a summary of the content of each part and chapter is provided, as a guide for the reader of this dissertation.

Part 1: Background

Chapter 1: The human heart

The research of this thesis is oriented towards the modelling and simulation of heart valves and intraventricular blood flow. Chapter one briefly introduces the main topics necessary to understand the clinical background of this work. The basis of anatomy, physiology and pathology of the human heart and its structures is provided. The complexity and the functions of the valvular structures (focusing on the mitral and aortic valves) and the left ventricle are described. The major valvular pathologies are detailed in the chapter and a brief overview about valvular prosthetic devices is provided. A brief summary of the most typical cardiac disorders is provided.

Chapter 2: Numerical methods and strategies for the simulation of intracardiac and transvalvular blood flow

As numerical simulations are the main topic of this dissertation, this chapter provides an overview of the main techniques to compute the fluid dynamics in the cardiovascular system. In case of full FSI simulations on aortic valves the motion is obtained thanks to the coupled solution of a fluid and a structural domain, such that the equilibrium of stresses and displacements at their interface is reached at all times. Another approach to study the intraventricular flows

is to make use of CFD analysis where the motion of the deformable structures is prescribed as known a priori from medical images. The different options available to discretize the fluid grid are discussed and details are provided on the advantages and disadvantages of each technique. This review does not intend to be fully exhaustive, but it aims to provide the essential information for the basic understanding of the concepts explained in the text.

Part 2: Fluid-structure interaction simulations on bioprosthetic aortic valves

Chapter 3: FSI simulations on aortic valves

In the past decades, a number of numerical simulation studies have been performed to analyze the performance of idealized, native or prosthetic aortic valves. Chapter three provides an overview on the two-dimensional (2D) and 3D models described in literature to perform FSI simulations on aortic valves. For the purpose of this work, the review focuses in particular on the mesh discretization, highlighting the choices made in the different FSI studies. When available and deemed relevant, results of the pressure, flow field and wall shear stress on the valve are reported.

Chapter 4: Comparison between IB and ALE techniques for the mesh representation

When setting up an FSI simulation, several choices are made with the aim to select the most suitable approach for the case of interest. In particular, to simulate flexible leaflet cardiac valves, the type of discretization of the fluid domain is crucial. This can be described with an ALE or an Eulerian formulation. The use of the ALE technique has advantages related to the intrinsic theoretical accuracy of the results, especially in the vicinity of the moving surfaces. In particular, pressures and wall shear stress (WSS) are more precise when calculated with this approach. However, the technique shows disadvantages in case of large displacement of the boundaries, as in the case of heart valves, as the fluid mesh can become highly distorted. In contrast, no mesh-motion issues are present with the Eulerian approach, but this comes at the cost of a less accurate calculation of the variables at the interface, such as pressure and WSS.

In this chapter we compare the results of the same aortic valve model on which FSI simulations based on the two different fluid grid discretizations have been realized, in order to compare the performance

of an ALE-based FSI solution and an Eulerian-based FSI approach. The comparison is done for a 2D and 3D case. In 2D no significant differences between the two methods are detected, while the 3D model reveals technical difficulties in both ALE and immersed boundary (IB) formulation, which impeded trustworthy results for the aortic valve simulation. In the 3D arbitrary Lagrangian-Eulerian fluid-structure interaction (ALE-FSI) the major limitation remains the excessive deformation of the fluid grid. For the 3D immersed boundary fluid-structure interaction (IB-FSI), the limitations encountered are mainly related to the choice of the solver. In fact, it was not possible to complete the simulated test case as the solver is not optimized (yet), technical difficulties were observed in both imposing the fluid-structure constraint and defining the volume-of-fluid function. The advantages/disadvantages of the two approaches are reported, the major limitations, hypothesis and approximations introduced are highlighted and discussed.

Chapter 5: Analysis of compressibility and other possible sources of suboptimal results in FSI simulations

One of the main hypothesis needed for the simulations in chapter 4 is the introduction of artificial compressibility in the FSI simulations, both in the IB and in the ALE technique, for different purposes.

In the IB-FSI case, a small degree of fluid compressibility is allowed to stabilize and speed up the simulation. In this chapter, a set of additional simplified tests has been performed to test if the introduction of the compressibility affects the results of the simulation, as the amount of compressibility introduced in our case was higher than reported values in literature. Furthermore, these tests aimed to explore whether the time delay detected in the valvular opening (for the IB case) could have been related to the compressibility or to other reasons. Tests demonstrated that the introduced compressibility in the IB-FSI case does not excessively influence the outcomes of the simulation. The time delay observed in the simulated leaflet motion can be ascribed to other factors: in the first place, the use of one-layer-thickness of linear continuum elements for the valvular leaflets increases the bending stiffness of the valve. Second, the no-slip condition constraint (enforced via the contact algorithm) between the fluid and the solid at the interface is not optimized and generated high frequency oscillations and a time delay at the onset of the simulation.

In the ALE-FSI case, the compressibility can be artificially included in the fluid solver to temporary mitigate the incompressibility

hypothesis which can generate spurious oscillations in the pressure field due to the large displacements of the structure and to allow a reduction of the computational time-step size. The compressibility introduced in the ALE case disappears once the coupling iterations at the interface are converged, therefore this quantity does not have any influence on the final result of the simulation. However, in our case the introduction of the interface artificial compressibility (IAC) in the 3D ALE-FSI did not improve the final outcome, as the mesh deformation was still too large to allow for the completion of the simulation.

Part 3: Computational fluid-dynamic simulations with prescribed moving boundaries

Chapter 6: Intraventricular flow: visualization techniques and numerical models

The analysis of intraventricular flow features provides physical insights on the hemodynamics of the heart and may potentially enhance the assessment of ventricular (dys)function and diagnosis. Multiple clinical imaging techniques are capable of visualizing the flow, the most widespread are briefly discussed in the first section of this chapter.

The combination/integration of clinical images and computational techniques allows for the realization of patient-specific computational models, which can provide more detailed and quantitative information on cardiac hemodynamics under precise conditions that are otherwise not easily measurable in a patient, such as intraventricular pressure gradients, vortex quantification or WSS. In the second section of this paragraph, a review of the main numerical techniques for intraventricular flow analysis is provided.

Chapter 7: Patient-specific CFD simulation of intraventricular hemodynamics based on 3D ultrasound imaging

In chapter 7, a novel technique to model patient-specific intraventricular flow, based on real-time transesophageal echocardiographic images (rt-TEE) ultrasound is described in full details and a test case is reported as example. The entire procedure has been developed ad hoc for moving left ventricular walls and mitral valve leaflets, starting from patient-specific segmented ultrasound images.

Briefly, the segmented images provide the position of the mitral valve (MV) and left ventricle (LV) at discrete time-points of the

cardiac cycle. In a pre-processing step, a time interpolation with 3rd order splines is performed for each point of the segmented surfaces, to obtain the node position as a function of time. During the simulation, the displacement of the outer wall of the computational domain is expressed as a linear combination of the displacement of the nearest points of the segmented surfaces. The identification of the nearest points, the update of the boundaries and the use of barycentric coordinates are performed adaptively every time-step to ensure the smoothness of the final result. Every time the outer wall was moved, the volume mesh was deformed accordingly using a spring model and remeshing was enabled in the fluid domain. The model has been applied to the ultrasound images of one patient (with hypertrophic ventricle but preserved ejection fraction (EF)) and the results have been provided. Even though the model has not been validated yet, the results obtained are realistic and in good agreement with the diagnosed pathology and its typical manifestations. The added value of the model is discussed, especially from a methodological point of view.

Chapter 8: Patient-specific CFD simulation of intraventricular hemodynamics based on 3D ultrasound imaging: comparison of three clinical cases

The model described in chapter 7 is extended and applied to a set of images obtained in three cases. The patients have been selected for their different clinical portrait. The first case shows a small ventricle, affected by hypertrophy but with a preserved EF. The second patient also shows ventricular hypertrophy but has an impaired EF, while the third case presents a dilated ventricle and extremely low values of the EF. Intraventricular pressures, velocity and vortex structures were calculated and the differences between the three cases are discussed.

Part 4: Conclusions

Chapter 9: Conclusions and future perspectives

The main conclusions of this PhD thesis are summarized in this section, with specific comments for the two main parts (II and III). The three research goals have been reached.

In the first place, a critical analysis of the simulation methods for FSI cases has been made, highlighting the limitations and advantages of two of the available approaches. Second, we realized a novel CFD approach to analyze intraventricular flows on a patient-specific basis.

The model is based on patient-specific pre-operative images and it is fully implemented within an ALE framework. Even though the model still lacks in-depth validation, the results are promising. In the third place, the model has been used to simulate the intraventricular flow field in three patients with different cardiac pathologies. The analysis verified the applicability of the model to different data-sets, and provided preliminary results on the abnormal flow patterns in pathological ventricles.

Table of contents

Abbreviations

Abbreviations

2D	two-dimensional
3D	three-dimensional
4D	four-dimensional
AL	anterior leaflet
ALE	arbitrary Lagrangian-Eulerian
ALE-FSI	arbitrary Lagrangian-Eulerian fluid-structure interaction
AO	aorta
AR	aortic root
AV	aortic valve
BHV	biological heart valve
BS	Bezier splines
CEL	coupled Eulerian-Lagrangian
CFD	computational fluid dynamics
CMR	cardiac magnetic resonance
CSM	computational solid mechanics
CT	computed tomography
D	diameter
DCM	dilated cardiomyopathy
ECG	electrocardiography
EF	ejection fraction
FD	fictitious domain
FEM	finite element method
FSI	fluid-structure interaction
FVM	finite volume method

HCM	hypertrophic cardiomyopathy
HV	heart valve
HVDs	heart valve diseases
IAC	interface artificial compressibility
IB	immersed boundary
IB-FSI	immersed boundary fluid-structure interaction
IQN-ILS	interface Quasi-Newton method, with a Least-Square method for the approximation of the Inverse of the Jacobian
L	length
LA	left atrium
LV	left ventricle
LVAD	left ventricular assist device
LVOT	left ventricle outflow tract
MHV	mechanical heart valve
MRI	magnetic resonance imaging
MV	mitral valve
NCS	Natural cubic splines
NS	Navier-Stokes
P1	Patient 1
P2	Patient 2
P3	Patient 3
PDEs	partial differential equations
PIV	particle imaging velocimetry
PL	posterior leaflet
rt-TEE	real-time transesophageal echocardiographic images
RVOT	rapid valve opening time
TAVI	transcatheter aortic valve implant
UDF	user-defined function

VOF	volume-of-fluid
WSS	wall shear stress
XFEM	extended finite elements method

Introduction

Rationale

Cardiovascular diseases are the leading cause of death worldwide, including both cardiac and vascular disorders. Some diseases, congenital or genetic, affect newborns or young individuals, but most cardiovascular diseases only appear later in life. In many of these disorders, the dynamics of blood flow (i.e. the hemodynamics) play a key role in the patho-physiological process (e.g. susceptibility to atherosclerosis in zones with low/oscillatory wall shear stress, susceptibility to thrombosis in zones with stagnant flow) and should be considered in the treatment of the disease.

Degenerative heart valve diseases have a significant prevalence in the elderly population (above 75y) reaching 13% in the western world. In the US only, it has been estimated that about 25% of the population above 65 years is prone to aortic sclerosis [1][2]. Prosthetic heart valves have been studied since they were first developed and implanted in the 1950s and are still one of the most effective and widely used techniques to treat valvular diseases, using either a mechanical or a biological prosthetic heart valve. The first is realized in poly-carbon, which guarantees good durability of the device, and has also acceptable properties in terms of bio-compatibility. However, the valve does result in distorted hemodynamics of the region of the implant as it does not resemble the physiological situation, which might reflect in long-term complications for the patient [3]. Furthermore, the implant of a mechanical heart valve (MHV) requires a life-long treatment of the patient with anti-coagulant drugs, to avoid blood clotting on the metallic surfaces of the valve. The biological heart valve (BHV) is commonly made of decellularized bovine pericardium or porcine valvular tissue, anchored on a stent/graft structure for mechanical support. This device guarantees more physiological hemodynamics of the region after the implant and does not require anti-coagulant treatment, but the BHV has durability problems: the life-span of the

device is 10-15 years, as the decellularized biological tissue loses its mechanical properties with time and a second implant is required.

More and more, valve sparing, valvular repair and less invasive (transcatheter) implant techniques are being explored, such as transcatheter aortic valve implant (TAVI) [4] for the transcatheter replacement of the aortic valve and MitraClip® (Abbott Vascular, CA, USA) for the transcatheter repair of the mitral valve. Despite the presence of a less invasive procedure and the reduction of the artificial material implanted in the patient, some of these techniques might (severly) affect the local hemodynamics (e.g. the mitral clip technique). The design, optimization and testing of novel prosthetic devices or treatments has been targeted, to constantly improve the quality of therapy for a better follow-up of the patient.

Valvular pathologies are often accompanied by cardiomyopathies, cardiac diseases affecting the muscular walls of the heart. On the long term, cardiac pathologies can result in reduced cardiac performance, abnormal geometries and increased load for the cardiac muscle. With the standard clinical imaging procedures, the cardiomyopathies are often detected at a late stage, when the disease is in an advanced state and remodeling already occurred. Nowadays, it is possible to investigate cardiac abnormalities by analyzing the flow patterns in the heart. This can be done (almost) routinely thanks to a number of clinical imaging techniques which allow for the reconstruction of the velocity flow field in the heart. Recent studies are investigating the relationship between abnormal flow patterns and early diagnosis of cardiomyopathies. If the correlation can be demonstrated, the use of the intraventricular flow results in a powerful early diagnostic tool, to improve the treatment of the patient and its follow-up.

In both valvular and ventricular applications, the integration of numerical simulations and clinical images in the scientific field have enhanced the opportunities to study the flow field in the cardiac region. The significant improvement of the computing capacity allowed for new and broader perspectives for the integration of computational tools in the clinical reality. Numerical simulations can have multiple applications in the cardiovascular field. Virtual testing and design optimization of new or existing devices provide performance details, reducing the time and the costs of experimental tests and manufacturing of prototypes. Computational models can be patient-specific (or device-specific): as such, the geometry is derived from clinical images and allow for a more realistic evaluation of the physical problem under investigation. Possible application of patient-specific simulations in

the clinical context can be, among others, the virtual planning of a surgical technique or device implant. In case of intraventricular flow analysis, for example, imaging techniques alone often cannot provide sufficiently detailed information about the hemodynamics of the region, as the quality of the data is affected by temporal and spatial resolution problems, the field of view can be limited and the noise included in the images may be significant. Numerical simulations can fill the gap where the clinical images cannot provide information, for example allowing to calculate fluid-dynamic variables not available elsewhere from in vivo diagnostic images (e.g. stress/strain in the tissues, wall shear stress (WSS) and detailed pressure field).

The focus of this dissertation is on the analysis and development of numerical techniques and models to gain a deeper understanding in the patho-physiology of the heart, with a particular attention for the integration of heart valves and valve leaflet motion into numerical blood flow simulations making use of arbitrary Lagrangian-Eulerian (ALE) approaches. The goal of this research is two-fold: on the one hand, we questioned the fluid-structure interaction (FSI) approach to study aortic valves and investigated the effects that the modeling choice for the fluid grid discretization has on the obtained results. On the other hand, a new methodology has been developed to study the intraventricular flows in the left heart, accounting for the motion of the mitral valve leaflets. In particular, a computational fluid dynamics (CFD) model with moving boundaries, based on patient-specific, pre-operative ultrasound images, has been developed. The methodology has been applied to different pathological scenarios to compare the fluid dynamics of different cases.

Research goals

The three main research goals are:

1. *Evaluate the feasibility of the ALE technique for FSI simulations of blood flow through aortic valves and assess the impact of the modeling choices on the final results;*

2. *Develop a new technique for CFD simulations with prescribed moving boundaries based on patient-specific ultrasound images to study intraventricular hemodynamics;*

3. *Demonstrate the potential clinical use and relevance of such a model by testing it on different patient-specific cases.*

Outline

This thesis is subdivided in four parts. As the field of interest investigated in this work is broad, both from the methodological and the clinical point of view, part I provides a brief summary on the anatomical, physiological and pathological background (chapter 1) which is fundamental to understand the clinical rationale and clinical motivations behind this work. Chapter 2 provides an overview on the numerical techniques used in the thesis, focusing on the crucial concepts discussed in the dissertation. In particular, as we want to investigate the fluid dynamics of the human heart, details are provided on the CFD techniques used, in particular in cases where the motion of the boundaries is included in the calculation. Both FSI and CFD simulations with moving boundaries are described, so the techniques available for the treatment of the fluid grid and fluid equations discretization are explained.

The main body of this work comprises parts II and III, which include the two main topics investigated in this dissertation. The second part (part II) provides the discussion on heart valve FSI simulations. In chapter 3, a literature review on the topic is provided, highlighting the methodological choices adopted in each case, to support the discussion of chapter 4. Here, the methodology used to study aortic valves is investigated in details. The same aortic valve model is studied with two different approaches, the immersed boundary (IB) and the ALE method for the mesh representation. The FSI simulation is performed in the two cases and considerations about advantages and disadvantages of both methods are provided. One of the major assumptions commonly introduced in IB-based simulations of aortic valves (as we also did in chapter 4) is the introduction of a (limited) compressibility of the blood. Therefore in chapter 5 the effects of the introduction of this artificial compressibility are analyzed.

Whereas part II provides a discussion of the modeling choices that can be made when performing simulations of heart valves, part III provides the description of a new methodology, developed to perform patient-specific CFD simulations on moving ventricles and mitral valves based on clinical images. Chapter 6 provides an introduction on intraventricular flow analysis and a review of the principal modeling techniques which have been reported in literature. Chapter 7 includes the detailed description of the developed methodology, starting from the use of ultrasound images through all the steps necessary to complete the patient-specific model to simulate intraventricular

flows. Finally, in chapter 8, the model is used to analyze the hemodynamics of the left ventricle in three different patient-specific cases: one patient with a hypertrophic ventricle with preserved ejection fraction (EF), one with a hypertrophic ventricle with reduced EF and one patient with a dilated ventricle. The results are compared to available literature reports.

In part IV, the most important conclusions of this dissertation are listed and some future perspectives are considered.

Each chapter is part of the entire thesis and the PhD project, but can be read and understood independently.

List of publications

First author peer-reviewed papers

- A. M. Bavo, G. Rocatello, F. Iannaccone, J. Degroote, J. Vierendeels and P. Segers, 'Fluid-Structure Interaction Simulation of Prosthetic Aortic Valves: Comparison between Immersed Boundary and Arbitrary Lagrangian-Eulerian Techniques for the Mesh Representation', *Plos One*, vol. 11, no. 4, e0154517, 2016
- A. M. Bavo, A. M. Pouch, J. Degroote, J. Vierendeels, J. H. Gorman, R. C. Gorman and P. Segers, 'Patient-specific CFD simulation of intraventricular haemodynamics based on 3D ultrasound imaging', *BioMedical Engineering OnLine*, vol. 15, no. 1, p. 107, 2016
- A. M. Bavo, A. M. Pouch, J. Degroote, J. Vierendeels, J. H. Gorman, R. C. Gorman and P. Segers, 'Patient-specific CFD models for intraventricular flow analysis from 3D ultrasound imaging : comparison of three clinical cases', *Journal of Biomechanics*, 2016

Conference contributions

- A. M. Bavo et al., 'Patient specific CFD simulations of intraventricular hemodynamics based on 3D ultrasound imaging', SB3C 2016, National Harbor, MD, USA
- A. M. Bavo et al., 'Patient-specific CFD simulations of intraventricular hemodynamics', Belgian National Day 2015, Brussels, Belgium
- A. M. Bavo et al., 'Computational fluid dynamic simulation of a moving valve: initial report', CFD in Medicine and Biology 2015, Albufeira, Portugal

- A. M. Bavo et al., 'FSI simulation of bioprosthetic aortic valves: comparison between IB and ALE formulation for the mesh representation', CMBE 2015, Paris, France
- A. M. Bavo et al., '3D fluid-structure interaction simulations of a commercial bioprosthetic valve', ECFD IV 2014, Barcelona, Spain
- A. M. Bavo et al., 'CFD simulations including contact of solid structures for a two dimensional heart valve', ESB 2013, Patras, Greece

I

Background

Chapters

Chapter 1

The human heart

1.1 Anatomy and physiology

A basic understanding of the anatomy and physiology of the cardiovascular system is indispensable for a clear understanding of the applications and motivations of the current work. Therefore, this introductory section provides a summary of the most relevant anatomical and (patho-)physiological background, useful for the understanding of the discussion. The references and text books on which this section is based are reported when appropriate. For a fully detailed description of the anatomy and physiology of the cardiovascular system, the reader is referred to the provided references.

1.1.1 The heart

The heart is a hollow muscle located in the chest, internally subdivided in four chambers (Fig. 1.1). It is vertically subdivided by the septum, a thick muscular wall which completely separates the left and the right heart. Functionally, the left and right heart act as two pumps placed in series, with the left heart supplying blood to the systemic circulation and the right heart to the pulmonary circulation. Each half is further subdivided in two chambers, the atria, located in the upper part and the ventricles, located in the lower part. Each atrium communicates with the corresponding ventricle with an unidirectional valve. These atrio-ventricular valves are called mitral and tricuspid valve, for the left and the right side respectively. The ventricles

are connected to the great vessels and to the circulation with two additional valves, known as semilunar valves, due to the shape of their leaflets. They are called the aortic and pulmonary valves for the left and the right heart, respectively. The heart valves are passive structures, their kinematics is driven by the pressure gradients across the valvular structure and no external energy is required for their motion. The main function of the heart valves is to guarantee the unidirectionality of the blood flow during the entire cardiac cycle [8].

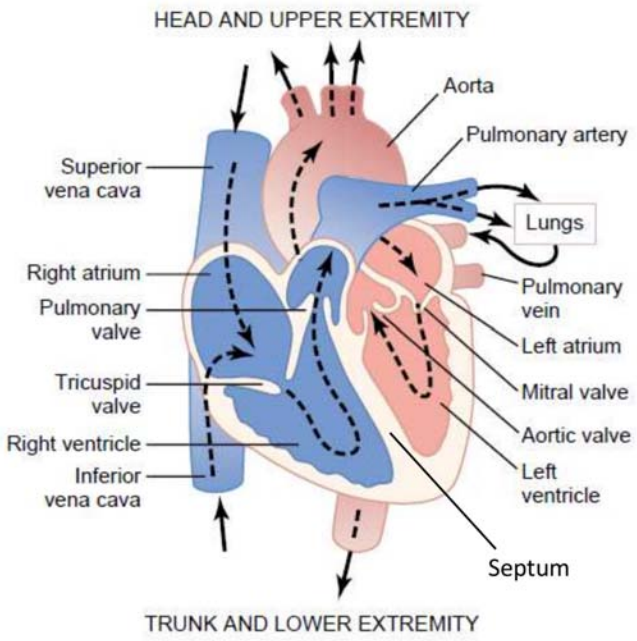

Figure 1.1: Schematic internal view of the heart (adapted from [8])

The right heart collects the oxygen-depleted blood rich in waste products from the peripheral organs through the superior and inferior vena cava and pumps it into the lungs via the pulmonary artery, where, thanks to the gas exchange, it becomes higlhy oxygenated and releases the carbon dioxide and the waste products of cellular metabolism. This circuit is known as the pulmonary circulation. From the lungs, the oxygenated blood reaches the left heart through the pulmonary veins, from which it is pumped into the aorta and the systemic circulation, to provide oxygen at the tissue level. The differences between the left and the right heart are physiologically related to the different pressure range they have to generate. To

overcome the systemic peripheral resistance, in fact, the left ventricle has to generate a significantly higher pressure than the right heart, which faces the low resistance offered by the lungs and the pulmonary circulation. In healthy adults, the average pressures in the heart are about ten times larger in the left ventricle than in the right ventricle [8]. This results in anatomical differences between the two halves, but the overall physiology is comparable. The most evident consequence of the different pressure regime of the two parts is the thickness of the ventricular wall, which is significantly higher on the left side, to provide more energy for the blood ejection. For the scopes of this thesis, the structures and the physiology of the left heart will be analyzed.

1.1.2 Aortic valve

The aortic valve (AV) is located between the left ventricle (LV) and the aorta, guaranteeing the unidirectionality of the blood which is ejected into the systemic circulation. The valve is anchored to a complex structure, known as the aortic root (AR). The aortic root provides a connection from the LV to the ascending aorta. It includes the basal ring, the valvular annulus, the sinuses of Valsalva and the sino-tubular junction (Fig. 1.2a). The basal ring is located in the ventricular portion of the aortic root, at this location the transition from the muscular ventricular wall tissue and the fibro-elastic aortic tissue begins. The annulus is a collagenous tissue structure which anchors the leaflets to the cardiac walls. It is a flexible and motile structure which complies with the motion of the valve while providing its structural support. The aortic wall immediately downstream the valve shows three enlargements in correspondence with the three cusps of the valve, called sinuses of Valsalva [9]. Two of the three sinuses host the coronary ostia, from which the coronary arteries arise (Fig. 1.2b), to provide the heart with oxygenated blood and guarantee its functioning. The sinuses and the leaflets are called after the coronary arteries which originate from the sinuses: the left and right sinuses give origin to the left and right coronary artery. The third sinus normally does not present any vessel, this is commonly known as the non-coronary sinus. The sino-tubular junction is the portion of the aorta comprised between the sinuses of Valsalva and the tubular portion of the ascending aortic arch. Due to the semi-lunar shape of the valve, the inter-leaflet triangles are fibrous structures connecting the left ventricle outflow trunk and the ascending aorta. The valvular leaflets are highly flexible and elastic structures which undergo significant displacements during the cardiac cycle. They

are, in good approximation, equal in size, shaped in a half-moon (Fig. 1.2b). Each cusp has two free edges, which are slightly thicker than the remaining of the leaflet and they partially overlap during closure, to increase the support of the valve in the closed position and guarantee the sealing of the valve. At the contact point of the three cusps, a small bulge is present on each leaflet. It is called the nodule of Arantio (Fig. 1.2c) and its main function is to provide additional mechanical support to the tip of the leaflet during the closed phase [9] [10].

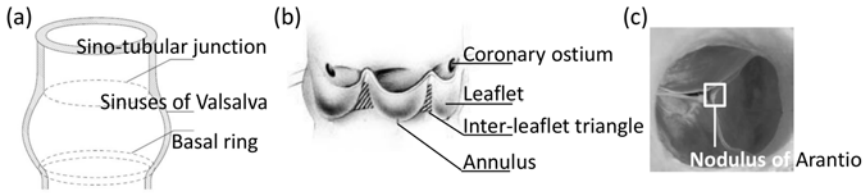

Figure 1.2: Fundamental anatomical components of the aortic root and aortic valve. (a) schematic drawing of the AR, (b) side view of a cut-open AV, (c) top view of the AV (adapted from [9] and [11])

1.1.3 Mitral valve

The mitral valve (MV) is located between the left atrium and ventricle and it is adjacent to the aortic valve. Similar to the AV, the valve is part of a more complex structure, known as the mitral apparatus. It is composed of the valvular leaflets, the annulus, the chordae tendinae and the papillary muscles. The orifice of the mitral valve is wider than the aortic valve and its morphology is more complex. The free edge shows several indentations, the two most profound divide the valve into two asymmetric leaflets (Fig. 1.3 a). The anterior leaflet (AL) is smaller, composed of one lobe and it is attached to the lateral side of the left heart, while the posterior leaflet (PL), on the other hand, is composed of three lobes. It is attached to the portion of the ventricular wall shared with the outflow tract of the left ventricle. The abundant tissue of the mitral leaflets is of extreme importance to guarantee the sealing of the valve in the coaptation zone [12]. The valvular leaflets are supported by the annulus, a D-shaped fibrous structure bridging the valve to the cardiac walls. The edges of the valvular leaflets are connected to the internal wall of the left ventricle with the chordae tendinae and the papillary muscles (Fig. 1.3 b). These structures are peculiar of the atrio-ventricular valves and they are not found in the semilunar valves. The function of the chordae

and papillary muscles is to tether the leaflets and avoid their prolapse into the atrium during the ventricular contraction once the valve is closed. In fact, the elevated pressure gradient which generates at every cardiac cycle across the MV during systole can reverse the valvular leaflets into the atrium resulting in the leakage of the valve. The papillary muscles are conical bundles of muscular fibers, arising from the ventricular surfaces (Fig. 1.4 b). In the left ventricle, typically, two papillary muscles can be found. The chordae arise from the head of these muscles and they connect to both the leaflets of the MV [13]. The number of the chordae and the position of the papillary muscles can vary on an individual base, however this does not have any clinical relevance.

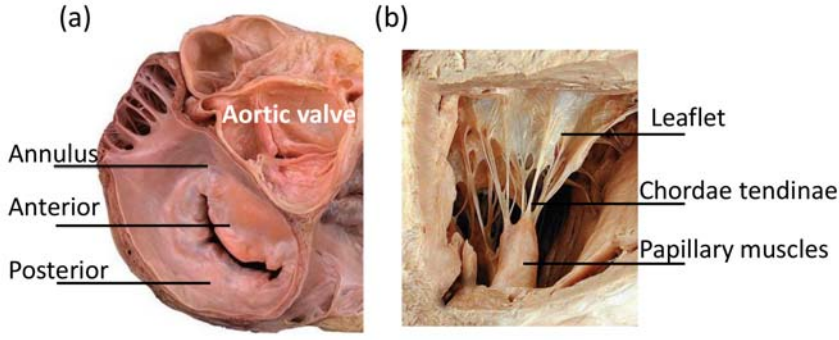

Figure 1.3: Fundamental anatomical components of the mitral apparatus and mitral valve (a) top view, (b) ventricular view (adapted from [11])

1.1.4 Left ventricle

The left ventricle has a conical shape with a rounded head called apex, pointing the diaphragmatic muscle. In Fig. 1.4 a transverse (a) and a sagittal (b) section of the heart are shown.

The muscular wall of the LV is the thickest in the human heart, due to the high pressures that are physiologically generated in this chamber. The internal wall, the endocardium, shows irregular muscular column structures, the trabeculae, which significantly increase the total surface in contact with the blood inside the ventricle. Among their functions, they are thought to reduce the turbulence of the blood in the ventricle [13]. They also provide support during the contraction of the papillary muscles which arise from the endocardium, preventing the bulging of the MV into the atrium and therefore leakage. The ventricular wall is an striated muscular structure, whose contraction is regulated

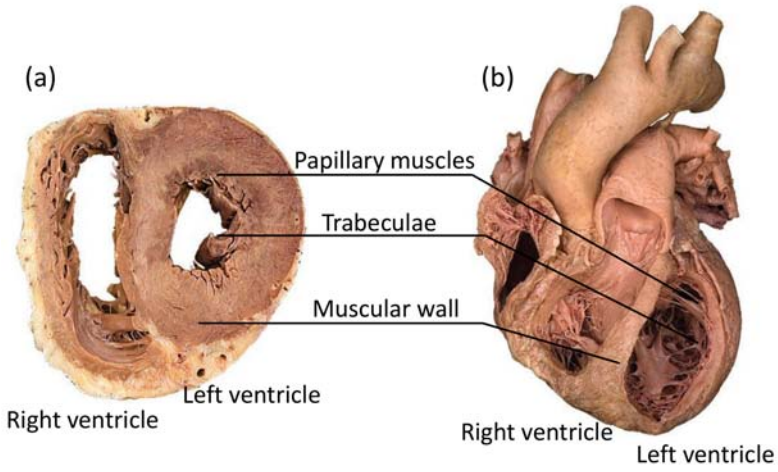

Figure 1.4: Transverse (a) and sagittal (b) section of human heart (adapted from [11])

by bundles of nerves from the autonomic nervous system included in the wall. The signal originates from the sino-atrial node (located in the walls of the right atrium) and it propagates via the His bundle from the atria to the ventricles. The His bundle runs into the septum such that it first excites the apex of the LV before the ventricular walls closer to the outlets [8]. This mechanism provides an optimal squeezing of the heart chambers and avoids stagnation of blood and promotes the washout of the LV.

1.1.5 Cardiac cycle

The cardiac cycle can be subdivided in several phases, which are shown in Fig. 1.5 for the left heart, in relation to the pressure curves (a) in the aorta (red dotted line), LV (blue solid line) and left atrium (blue dotted line), the flow (b) through the aortic (red solid line) and the mitral (blue dotted line) valves, the volume curve (c), the heart sounds (d) and the ECG signal (e).

When the pressure in the left ventricle increases above the atrial pressure, the atrio-ventricular valve (here MV) closes (1). After a short period of isovolumic contraction, during which the ventricle contracts to increase its inner pressure, the ventricular pressure becomes higher than the aortic pressure (2) and the aortic valve opens. During this period, ventricular pressure is higher than the atrial pressure and the mitral valve remains in the closed position. At (2) the systolic phase begins, the ventricle contracts and the blood is ejected into the

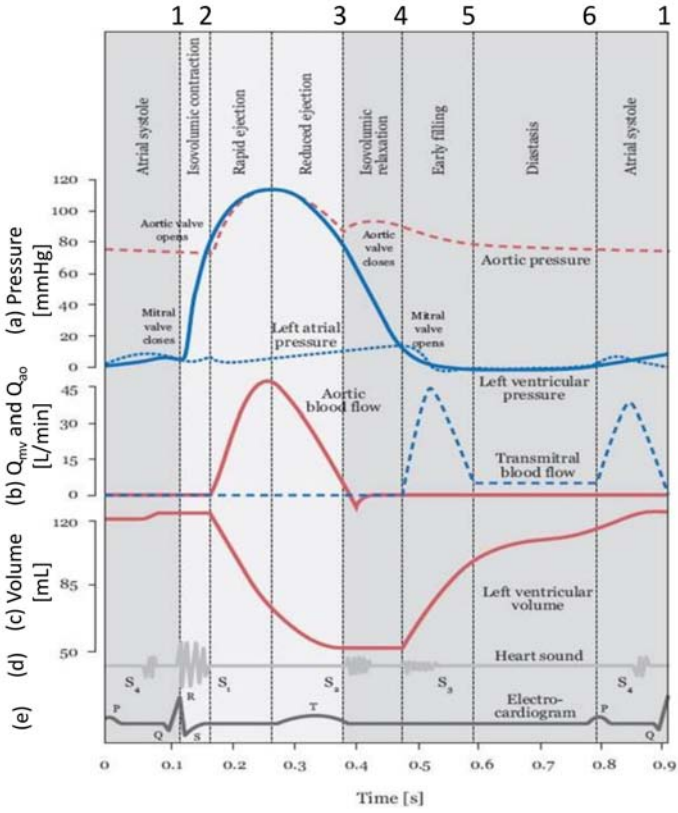

Figure 1.5: Cardiac events during the cardiac cycle. Pressure curves (a): aortic pressure (red dotted line), ventricular pressure (blue solid line), atrial pressure (blue dotted line). Flow through valves (b): aorta (red), mitral (blue dotted line). Ventricular volume curve in red (c). Heart sounds (d) and ECG (e). Adapted from [14][15])

aorta (flow curve in red), with a high velocity jet. The volume of the LV decreases exponentially (from 2 to 3), until the closure of the aortic valve, when the pressure in the aorta overcomes the ventricular pressure (3). During the ejection phase of the ventricle, the atrium is filling with the blood coming from the left and right pulmonary veins, therefore its pressure slightly increases. As long as the ventricular pressure remains higher than the atrial pressure, both valves are closed, and the ventricle experiences a short phase of isovolumetric relaxation, during which the ventricular volume remains constant (from 3 to 4) and the ventricular pressure drops until it becomes lower than the atrial pressure. At this time-point (4), the diastolic phase begins and the mitral valve opens, allowing the blood accumulated

in the atrium to flow into the ventricle (rapid ventricular filling). A first peak is recorded in the flow curve through the MV, the so-called E-peak (flow curve, blue dotted line). The volume of the ventricle has a sudden increase (until 5), followed by a stasis (6) phase and a second filling phase (until 1). The latter is due to a late atrial contraction, which allows for a late ventricular filling, which corresponds to the second peak in the transmitral flow curve. During diastole, thanks to the elasticity of the aorta, the pressure at this location experiences an exponential decrease and the blood is driven from the aorta to the systemic circulation. When the ventricular pressure exceeds the atrial pressure (1) with the start of the next heartbeat, the mitral valve closes and a new cardiac cycle starts [8][15].

1.2 Pathology

1.2.1 Valvular pathologies

The heart valve diseases (HVDs) can be classified in two main groups: stenotic or regurgitant, although some valves can be both stenotic and regurgitant. A stenotic valve (Fig. 1.6 b) has a thicker valvular structure, often showing calcium deposits on the cusps.

The abnormal thickness and the presence of deposits generate an impaired motion of the valve, both in the open and in the closed position. A stenotic open valve shows a smaller orifice, which generates a concentrated hydraulic resistance for the blood flow, resulting in a higher energy expense for the heart. A stiffer valve can also result in a regurgitant valve (Fig. 1.6 c), in the closed position. This is the second pathology that mostly affects the cardiac valves. In this case, the leaflets do not completely seal when the valve is in the closed position, resulting in a leaking valve. Besides calcified leaflets, other prevalent sources of regurgitation can be dysfunction of the valvular apparatus due to cardiac or aortic/pulmonary dilation, disruption of the chordae tendinae for mitral and tricuspid valves among others. The presence of retrograde blood flow decreases the efficiency of the heart, which necessitates higher energy to maintain a physiological cardiac output. The two pathologies can occur simultaneously, resulting in a stenotic-regurgitant valve.

If not treated, the HVDs are most of the times lethal for the patient. The treatment is defined by the cardiologist and/or the cardiac surgeon, on the base of the clinical images acquired and on the patient clinical history. Depending on the pathology, the valvular apparatus can be surgically repaired, to restore the valve functionality,

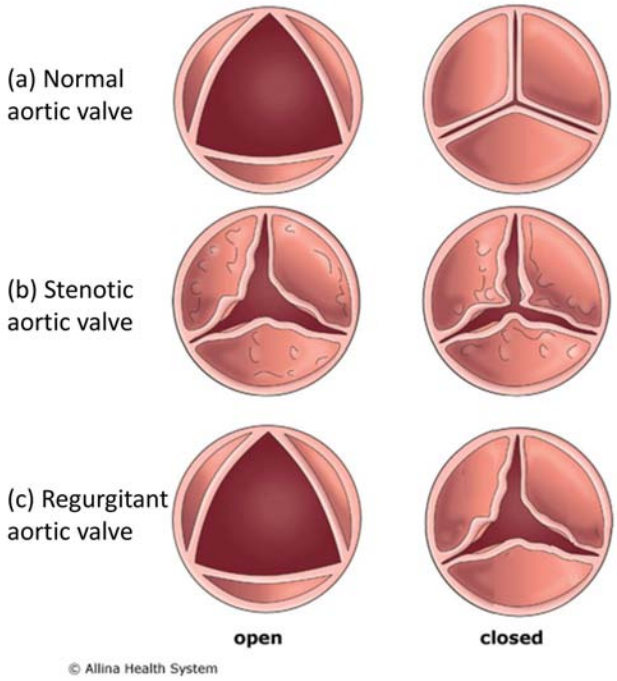

Figure 1.6: Comparison between a physiological (a), stenotic (b) and regurgitant (c) aortic valve (adapted from [16])

or, in most of the cases, the valve is replaced by a prosthetic device. There are two main categories of prosthetic valves which can be implanted with an open-chest surgical procedure, the mechanical heart valve (MHV) and the bio-prosthetic (biological heart valve (BHV)) heart valve (Fig. 1.7).

The MHV are commonly made of poly-carbon, which guarantees good mechanical properties and ensures a reasonable durability for the prosthesis. However, these devices are prone to thrombo-embolic events (blood clotting), and the recipient has to undergo a life-long anticoagulant therapy [18]. BHV, on the contrary, are made of biological tissues, either bovine pericardium or porcine valvular leaflets, normally supported by a stent and/or graft structure. The BHV have much more physiological hemodynamic properties and do not require anticoagulant therapy for the patient. Their durability is lower than MHV: the patient normally requires a re-intervention after 10-15 years [3]. More recently, the transcatheter aortic valve implant (TAVI) valves have been introduced in the clinical practice. This

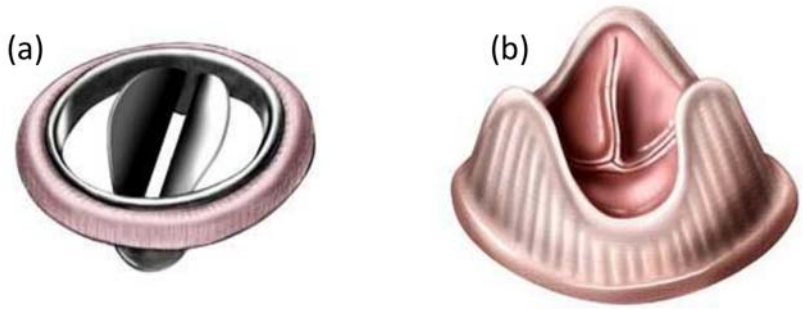

Figure 1.7: Artificial prosthetic valves. (a) Mechanical heart valve. (b) Biological heart valve (adapted from [17])

device consists in a biological valve mounted on a crimped stent and it is deployed in the desired location with a catheter inserted from the femoral artery [4]. The procedure does not require the open-chest surgical procedure, being particularly useful for patients not suitable for highly invasive surgery.

Despite the fact that the valvular prosthesis implant is a life-saving treatment, it involves several disadvantages and possible complications for the patient. The high prevalence of HVDs, the elevated costs of the diagnosis, treatment and follow-up of the patients are all concurrent causes to the great interest in the cardiovascular researches over the past few decades. The results of the effort are evident: the current golden standard for artificial valvular prosthesis is extremely elevated and the mortality related to the surgical intervention or the device itself has dropped dramatically over the years [3].

1.2.2 Epidemiology of heart valve diseases

HVDs are one of the leading death causes worldwide. The degenerative HVDs are age-dependent, thus they represent a serious and growing public-health problem, especially in the Western world [19]. Recent population-based studies demonstrated that the prevalence of the HVDs in the US falls below 2% in subjects of <65 years, but abruptly increases to the 13.2% for subjects >75 years [19] [20]. Besides the clear correlation of HVDs with age, a combination of risk factors increases the risk of cardiovascular degenerative pathologies, for example hypertension, hyperlipidemia, smoking and diabetes [21]. Most of them are general risk factors and are typical for all the cardiovascular diseases, especially for atherosclerosis. The most common

degenerative HVDs are aortic stenosis and mitral regurgitation, which occur in 3 out of 4 cases of HVDs [20]. In the developing countries, the etiology of HVDs is different and the prevalence of degenerative valvular diseases is lower, also due to the lower life expectancy. In these countries, the incidence of rheumatic valvular diseases is of 1 to 7 cases every 1000 [20], due to the high risk of infections, rheumatic fever and poor early diagnostic tests.

1.2.3 Cardiomyopathies

The heart is an optimized physiological system, evolved such that its energy consumption is minimized while providing the required pressure (and flow) to the entire organism. In case of pathologies, the human body and more specifically the heart is capable of adaptation, to guarantee the perfusion of the body and maintain a suitable amount of blood reaching the body districts. This is one of the reasons why patients with underlying cardiac pathologies do not immediately show symptoms and why it is hard to obtain a reliable early diagnosis for these pathologies. The etiology of the cardiomyopathies is often unknown or difficult to investigate. The two most common pathological phenotypes are dilated cardiomyopathy (DCM) and hypertrophic cardiomyopathy (HCM), which can be obstructive or non-obstructive. The two cases are schematically depicted in Fig. 1.8. More cardiac pathologies have been classified which are not listed in this text and the reader is referred to [22] for further details.

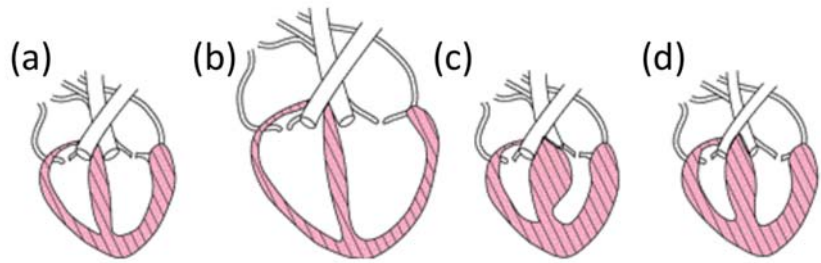

Figure 1.8: Schematic comparison between a normal heart (a), a dilated heart (b) and a hypertrophic heart (c and d) (adapted from [23])

A DCM (Fig. 1.8b) shows a ventricular dilation, with a thinner and enlarged ventricular chamber. The systolic function is impaired, due to the lower contractility of the LV and the larger amount of blood stored in the ventricle during diastole. Often, the dilated cardiomyopathy

is associated with mitral (and/or tricuspid) regurgitation and atrial dilation.

A hypertrophic cardiomyopathy (Fig. 1.8 c-d)presents a thicker ventricular wall, resulting in a thick, stiff and less compliant ventricle [22]. Depending on the location of the thickening, the hypertrophic myopathy can be obstructive (if the enlarged portion is close to the left ventricle outflow tract (LVOT), Fig. 1.8 c) or non-obstructive (apical area, Fig. 1.8 d). Both hypertrophy and dilatation can lead to an impaired stroke volume (the volume of blood ejected into the aorta at each heart beat) and a limited perfusion of the peripheral organs and ejection fraction (EF) (the ratio of stroke volume and ventricular volume at the end of diastole). For further details on these pathologies, the reader is referred to the work of Sisakian et al. and Phelan et al [22][24].

Other myocardial disorders can be related to contractility dysfunctions. Modifications of the contractility of the heart, such as myocardial ischaemia (insufficient oxygen supply to the heart due to a stenosis or necrotic areas of the endocardium which loses motility and muscular function after a myocardial infarction), abnormal electrical conduction of the excitation signal, arrhythmias or cardiac dyssynchrony, lead to a disorganized flow field in the LV and a sub-optimal blood ejection. Especially in ischaemic patients, the necrosis of part of the endocardium generates hypokynetic areas of the ventricular wall, resulting in a non-organized wall motion, a hypomotile ventricle and reduced ventricular function.

Most of the times, valvular and ventricular pathologies are interdependent. The LV has the ability to remodel and adapt its shape to compensate other abnormalities, e.g. a valvular stenosis. In the case of an aortic stenosis, the LV has to overcome a higher hydraulic resistance to maintain a constant stroke volume and cardiac output. Therefore, it can enlarge and/or increase the wall thickness. An overall increase of the systemic pressure could also be detected. An excessive enlargement of the LV can result in a dilated cardiomyopathy, which can influence the function of the MV with its leaflets losing coaptation and sealing, reinforcing the disease and enhancing further dilation.

1.2.4 Epidemiology of cardiomyopathies

The most common cardiomyopathy is DCM, comprising almost 60% of the cardiomyopathies cases worldwide. It is present in both adults and children, with a prevalence of 1:2500 in adult patients.
The prevalence of HCM is estimated to be 0.2%. One third of the

patients do not show any obstruction at the LVOT location, while the remaining two thirds of patients presents high pressure gradient and obstruction of the LVOT due to the hypertrophy [22].

Chapter 2

Numerical methods and strategies for the simulation of intracardiac and transvalvular blood flow

2.1 Introduction

Computational fluid dynamics has a long history in cardiovascular biofluid mechanics as it gives access to an extremely detailed fluid-dynamic analysis of the region under investigation, allowing for the calculation of variables which cannot be measured with any other technique (such as wall shear stress metrics or, to some extent, vortex formation or flow instabilities in the LV). The computational models are based on systems of partial differential equations (PDEs), which govern the physics underlying the described physical problem. For few idealized cases, it is possible to solve these equations analytically, but in most of the cases there is the need of using numerical computation for the system solution. This is especially true for the fluid-mechanical applications studied in this thesis, where sources of complexity are the three dimensionality of the problem, the geometry, the boundary conditions, the material properties and (in most cases) the transient nature of the problem. Under these complex conditions, computational fluid-dynamics for fluid problems or computational

solid mechanics (CSM) for structural problems can provide an approximation of the real solution by discretization of the governing PDEs. When performing a computational simulation, the domain has to be discretized (i.e. subdivided in small elements/volumes in which the equations are solved in their discrete formulation). Of particular interest in this work is the space discretization of the physics laws used in the analysis which can be done using a Lagrangian, Eulerian or arbitrary Lagrangian-Eulerian (arbitrary Lagrangian-Eulerian (ALE)) approach. The three techniques are schematically represented in Fig. 2.1.

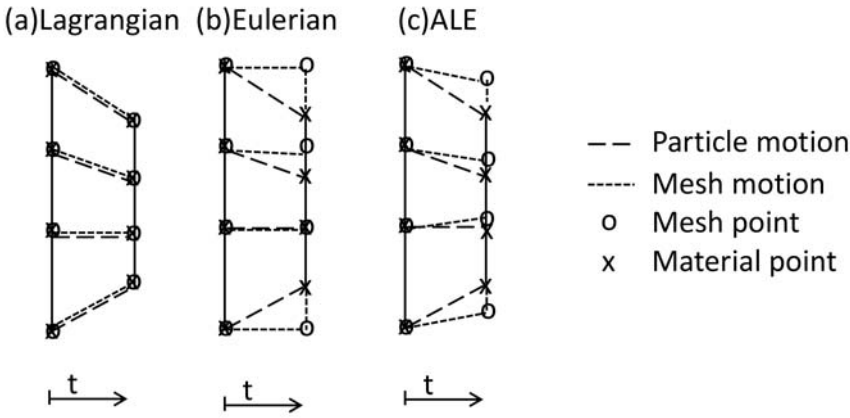

Figure 2.1: Schematic representation of the three different space discretization techniques. (a) Lagrangian, (b) Eulerian (c) ALE method (adapted from [25]).

- *Lagrangian formulation* (2.1 a): with the Lagrangian formulation, the displacement/deformation of the object/material is followed in time by the computational mesh. This results in a deforming and moving mesh with a grid velocity equal to the material velocity. This technique is commonly used for CSM simulations as one of the main advantages is that free moving surfaces are easily traceable over time [25].

- *Eulerian formulation* (2.1 b): in contrast with the Lagrangian approach, the Eulerian technique writes the PDEs as a balance of the material flowing in and out of a control volume fixed in time. This translates in a mesh which does not move, through which the material flows. The technique is commonly used

for computational fluid dynamics (CFD) simulations. Large displacements of particles can be nicely represented with this technique [25].

- *Arbitrary Lagrangian-Eulerian formulation* (2.1 c): the technique combines the two previously described methods, as the name suggests. The fluid grid is allowed to deform with an arbitrary velocity which is not necessarily the material velocity. This technique is commonly used in fluid-structure interaction (FSI) simulations or CFD simulations in which one or more surfaces are allowed to move.

The remaining of this chapter summarizes the most typical (fluid-mechanics) numerical simulations, with a specific focus for cardiovascular applications. The text is mainly based on the work of Degroote et al.* [26] and of Quarteroni et al.† [27], to which the reader is referred for further details.

2.2 Computational fluid-dynamics: solving flow problems in non-deforming domains

2.2.1 Navier-Stokes equations

In pure fluid-dynamic problems, with rigid and stationary boundaries, the PDEs are solved in the Eulerian formulation. Two conservation principles govern the velocity of an isothermal fluid: the conservation of mass and the conservation of momentum. The conservation of mass forces the global mass of the system to be constant in time. This can mathematically be written as:

$$\frac{\partial \rho_f}{\partial t} + \nabla \cdot (\rho_f \vec{v_f}) = 0 \tag{2.1}$$

where ρ_f is the fluid density and $\vec{v_f}$ is the fluid velocity. For incompressible fluids in which the density is constant, the equation can be simplified as:

$$\nabla \cdot \vec{v_f} = 0 \tag{2.2}$$

*J. Degroote, 'Partitioned Simulations of Fluid-Structure Interaction', *Arch Comput Methods Eng*, vol. 20, pp. 185–238, 2013

†A. Quarteroni and L. Formaggia, 'Mathematical Modelling and Numerical Simulation of the Cardiovascular System', in *Modelling of Living Systems, Handbook of Numerical Analysis Series*, P. Ciarlet and J. Lions, Eds., Amsterdam: Elsevier, 2004, pp. 3–127

For a generic flow, the momentum (or Navier-Stokes (NS)) equation can be written as:

$$\rho_f \frac{\partial \vec{v_f}}{\partial t} + \rho_f \vec{v_f} \cdot \nabla \vec{v_f} = \nabla \cdot \bar{\sigma_f} + \vec{f_f} \tag{2.3}$$

where the external forces are separated in surface forces per unit of surface ($\bar{\sigma_f}[N/m^2]$) and body forces per unit of volume ($\vec{f_f}[N/m^3]$). The surface forces are expressed with the Cauchy stress tensor $\bar{\sigma_f}$, as shown in paragraph 2.2.2.

For most cardiovascular applications, the effect of gravity can be neglected and the fluid is considered incompressible. Equation 2.3 can then be written as:

$$\rho_f \frac{\partial \vec{v_f}}{\partial t} + \rho_f \nabla \cdot (\vec{v_f} \vec{v_f}) = \nabla \cdot \bar{\sigma_f} \tag{2.4}$$

2.2.2 Constitutive law

Given the NS equations, it is necessary to link the Cauchy stress components with the kinematic variables (the velocity field in particular) to be able to close the PDEs system and solve the problem. The Cauchy stress tensor can be split in the internal pressure term (p_f) and the shear stress component ($\bar{\tau_f}$) which is caused by the viscous forces. Blood is a Non-Newtonian fluid [28] [29] (for a given hematocrit, the viscosity μ is dependent on a.o. the shear rate), however for simplicity reasons, in this work it will always be assumed as a Newtonian fluid, thus the viscosity is assumed constant and independent of the shear rate. Under the Newtonian fluid assumption, the stress tensor ($\bar{\sigma_f}$) can be rewritten as:

$$\bar{\sigma_f} = -p_f \bar{I} + \bar{\tau_f} = -p_f \bar{I} + 2\mu \bar{\epsilon_f} \tag{2.5}$$

Where $\bar{I}$ is the identity tensor and $\bar{\epsilon_f}$ is the strain rate tensor, calculated as:

$$\bar{\epsilon_f} = \frac{1}{2}[\nabla \vec{v_f} + (\nabla \vec{v_f})^T] \tag{2.6}$$

By including equations (2.5) and (2.6), equation 2.4 becomes:

$$\rho_f \frac{\partial \vec{v_f}}{\partial t} + \rho_f \nabla \cdot (\vec{v_f} \vec{v_f}) = \nabla \cdot (-p_f \bar{I} + \mu \nabla \vec{v_f} + \mu (\nabla \vec{v_f})^T) \tag{2.7}$$

2.3 Solving flow problems in deforming domains: fluid domain discretization

In many cardiovascular problems (e.g. blood flow in a distending aorta, blood flow through valves, blood flow inside a contracting ventricle, ...) there is a substantial interaction between a solid body and fluid, and it is insufficient to just solve the CFD problem. In this case, it is much more accurate to solve both the CFD problem at hand, while also accounting for the deforming structure. This can be done by either prescribing the motion of the deforming structure if this is known a priori, either by simultaneously solving the fluid and the structural mechanics problems. If the fluid domain under investigation moves or deforms and its deformation is known a priori, CFD simulation with prescribed moving boundaries can be performed. This technique cannot be fully considered as an FSI simulation as no calculation of the structural equations is required. The approach does not require any knowledge about the material properties of the structure as only the position of the interface/boundary is of interest.

The major burden of any type of fluid-dynamic simulation with moving boundaries (both prescribed or calculated) is the fluid discretization technique. This can be approached with a conformal method (based on the ALE formulation) or on a fixed grid method (based on the immersed boundary (IB)/fictitious domain (FD) formulation). The following description applies for CFD simulations with moving boundaries and for FSI simulations (with regards to the equations of the fluid domain).

2.3.1 Conformal methods and ALE formulation

As described in chapter 2.1 and Fig. 2.1, with the ALE discretization method the fluid grid is allowed to deform at an arbitrary velocity to guarantee a body fitted (or conformal) fluid grid. The major advantage of a conformal mesh is the correspondence of the moving boundary with the mesh lines, as such the geometrical details (and discontinuities) can be incorporated in the calculation accurately [30]. Furthermore, no approximation is required for the analysis of quantities at the moving boundary, e.g. wall shear stress (WSS), pressures etc.

In the ALE formulation of a deforming fluid grid, the velocity of the moving walls is imposed, in the FSI case the velocity at the interface is equal to the velocity of the solid material at the interface (no slip conditions) to avoid the overlapping of the two domains. The grid velocity $\vec{w}$ has to be included in the NS equations. For a finite

volume discretization, equations 2.1 and 2.3 are integrated over a finite volume V bounded by a surface S and become:

$$\frac{\partial}{\partial t}\int_V \rho_f dV + \oint_S \vec{n}\cdot\rho_f(\vec{v_f}-\vec{w})dS = 0 \tag{2.8a}$$

$$\frac{\partial}{\partial t}\int_V \rho_f\vec{v_f}dV + \oint_S \vec{n}\cdot\rho_f(\vec{v_f}-\vec{w})\vec{v_f}dS = \oint_S \vec{n}\cdot\bar{\sigma_f}dS + \int_V \vec{f_f}dV \tag{2.8b}$$

with $\vec{w}$ the velocity of the boundary of the control volume (which can be a grid wall) and $\vec{n}$ the surface normal unit pointing outward the element. Note that, when applied to a computational mesh, the case $\vec{w} = 0$ yields the Eulerian formulation, while $\vec{w} = \vec{v_f}$ yields the Lagrangian formulation. In the ALE case, $\vec{w}$ is defined at the boundaries and extended to every cell in the domain via extension functions to avoid excessive grid distortion. Different options are available to extend the grid velocity from the moving boundary to the remaining of the domain. A common technique is to make use of the spring method (Fig. 2.2 b), which considers each edge between two computational nodes as a spring. The initial length of the edge corresponds to the equilibrium state of the spring. Any displacement of one of the nodes (on the moving surface) generates a force proportional to the displacement on all the springs connected to the node, such that the new position of the internal nodes is recalculated based on this spring force. Often the spring coefficient is chosen inversely proportional to the length of the edge, such that shorter edges are stiffer and the long edges can adsorb more displacement, towards a grid with a more uniform quality. At the equilibrium the net force on each node due to the springs has to be zero. This is achieved using an iterative procedure [31]. Another technique for the fluid grid deformation is to displace the interior nodes with a Laplace (diffusivity) equation (Fig. 2.2 c). The diffusion parameter can be calculated based on the wall distance (to preserve a good quality mesh in the vicinity of the moving walls) or based on the cell volume, to maintain a uniform mesh (larger elements absorb more deformation than smaller elements) [31].

Despite the use of extension functions, if the movement of the boundaries is too large, the quality of the fluid grid degenerates. If the displacement of a point in one time-step is larger than one time the dimension of the element in the direction of the motion, the volume of the element becomes negative, leading to the failure of the

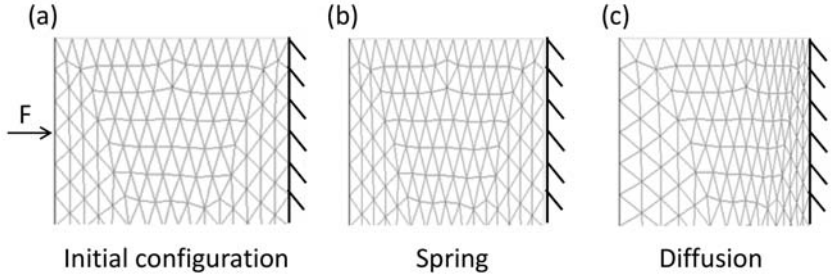

Figure 2.2: Examples of smoothing algorithms available in Fluent. (a) undeformed domain subject to a compression force F. (b) resulting domain using a spring-based smoothing method. (c) resulting domain using a diffusion smoothing method based on the wall distance method.

simulation. To avoid this problem, the mesh has to be partially or globally modified to adjust to the large motion of the boundaries. If the position of the boundaries is known a priori (in CFD with moving boundaries) or can be estimated, one option is to generate a number of intermediate meshes from the initial to the final configuration. Every time the quality of the computational grid falls below a predefined threshold, the fluid grid is replaced with a new high quality mesh with the boundaries located at the current position. The solution of the flow field has to be interpolated from the old to the new mesh. This technique was used for example in CFD simulations with prescribed moving boundaries for the ALE simulation of ventricular dynamics (no valve included) [29] [32]. The approach adopted in this work is the use of the automatic remeshing tools available in Fluent 15.0. Low quality zones of the computational mesh are automatically modified to guarantee a good quality grid. The remeshing process enhances the quality of the fluid grid but increases the computational time for the simulation and introduces numerical diffusion due to the interpolation process necessary to move from the old to the updated mesh.

2.3.2 Fixed grid methods

One of the alternatives to the body fitted discretization methods in case of deforming domains is the use of a fixed fluid grid. The pioneering technique of this category is the IB method, first developed by Peskin in 1972 [33] for heart valve applications. In this method, the solid boundary is modeled by a set of non-conforming interconnected Lagrangian points, moving on top of an Eulerian, finite-difference fixed grid. To account for the presence of the solid, a weighting

function is defined in the vicinity of the solid nodes to interpolate the forces exerted by the Lagrangian bodies on the Eulerian grid. This function results in a body force term $\vec{f}_f$ in the NS equation of the corresponding elements. By doing so, the body force term is spread over a few fluid nodes, resulting in a diffuse solution at the fluid interface. Conversely, the influence of the fluid on the solid is obtained by velocity interpolation from the fluid to the structure. The method implies that the structure is divergence-free, as the velocity is obtained from the incompressible fluid to the structure. The main advantage of this approach compared to the ALE method is the absence of fluid grid motion and deformation, allowing for the simulation of large solid motion/deformation. The most crucial disadvantage is the loss of accuracy at the interface. Furthermore, the accuracy of this method is dependent on the mesh size, and the assumption of a divergence-free structure might not be always adequate. The original IB method was developed to allow the interaction between interconnected points and a fluid. This has been expanded to methods to simulate the interaction of the fluid with points carrying mass, structures with volumes, rigid bodies and slender bodies among other.

A similar methodology in the fixed-grid simulations category is the FD method, initially proposed for FSI of rigid bodies and a fluid [34] and then extended to the interaction of a fluid and flexible bodies [35]. In this method, the region of the fluid mesh occupied by the solid is filled with a fictitious fluid with the same properties of the real fluid. Lagrangian multipliers are used at the interface to track the position of the interface and to force the velocity of the fluid at the interface to be equal to the velocity of the solid. The advantages and disadvantages of this method are comparable to those listed for the IB method.

As the use of fixed grid methodologies to study flexible and motile structures such as heart valves is very promising and interesting, the original IB/FD methods have been modified to improve their performances.

To improve the IB method and solve the diffuse-interface issue which is arising from the use of the interpolation of the body force over a few fluid nodes, a class of sharp-interface methods have been developed. Instead of distributing the body force term on the fluid nodes, this methodology calculates adequate boundary conditions for the fluid nodes in the immediate vicinity of the interface. In these nodes (in yellow, Fig. 2.3a), the velocity $\vec{u}_b$ is calculated as a linear interpolation between the nearest fluid point (in blue, Fig. 2.3a, where

the velocity $\vec{u}_c$ is obtained from the flow field calculation) and the nearest point on the solid interface (in red, Fig. 2.3a, where $\vec{u}_a$ is obtained from the structural calculation).

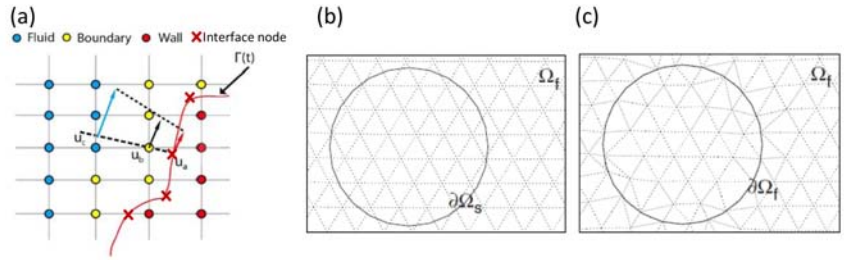

Figure 2.3: (a) Schematic representation of the sharp-interface method. The velocity at the boundary nodes (yellow) is calculated as linear interpolation between the velocity of the fluid (blue) and of the structure (red). Adapted from [36]. (b-c) Fluid FD mesh with local adaptation: from a solid boundary curve $\partial\Omega_s$ intersecting the fluid domain Ω_f (b), the inner fluid curve $\partial\Omega_f$ is created and the mesh adapted (c) (adapted from [37])

In the work of Gilmanov et al. [38], a second order accurate finite-difference method is proposed to implement the incompressible NS equations in a Cartesian domain containing an arbitrary complex IB surface. In this work the reconstruction of the solution is done along the local normal of the body surface.

The advantage of this approach is the presence of a sharper definition of the interface, especially on the fluid domain while preserving the fixed fluid grid. However, the methodology described in Gilmanov et al. is applicable only to Cartesian grids. In the case of a boundary grid which does not undergo significant movement (e.g. the aortic wall compared to the aortic leaflets), a conformal-grid approach for the background grid would be preferable. Therefore, the method described in Gilmanov et al. [38] has been extended to a fully curvilinear staggered discretization approach in the work of Ge et al. [39], resulting in a CURVIB/sharp-interface method. The approach is consistent with the procedure proposed in [38], but the equations have been generalized for a curvilinear body-fitted domain. The sharp-interface formulation of the immersed bodies has been preserved from the previous work, and cardiovascular applications have been reported in [39] and [40].

A similar approach is described in the work of Mittal et al. [41], where a "ghost-cell" method combined with a conformal curvilinear

grid is presented. These advanced IB methods solved the diffuse-interface issue, as no additional body force is added on the fluid domain, avoiding the spurious spreading of the boundary force over the fluid elements. Furthermore, the use of a boundary conformal approach (curvilinear methods) for the background mesh provides a good treatment of the external boundaries for the fluid domain without losing the advantages of a fixed mesh. The use of curvilinear background meshes, however, is limited to relatively simple shapes for the fluid domain and the accuracy of the fluid-structure interface of an immersed body such as a cardiac valve is dependent on the fluid grid size.

Other modifications of the IB/FD methods have been proposed, based on the cut-cells method [42] or local remeshing for the fluid grid [37]. In the latter case, the fluid cells in the surrounding of the solid interface are targeted and subdivided, to obtain a conformal-grid in the vicinity of the interface, without the need of deforming the entire fluid grid. For example, in the work of Van Loon et al. [37], the fundamental concepts adopted to modify the FD method with a local mesh adaptation are detailed. When a solid body intersects the fixed fluid domain (Fig. 2.3b), an inner fluid curve is generated and the fluid node positions are modified such that the fluid grid at the curve is conformal to the solid location (Fig. 2.3c). This technique is computationally not expensive and guarantees a local adaptation of the fluid domain, for a higher accuracy of the solution in terms of pressure jump across the surface and WSS [37]. As disadvantages, this technique could result in irregular, small and distorted fluid elements on the fluid side, especially for three-dimensional (3D) applications.

Other options to improve the performances of the initial FD methods were explored, for example with the so called extended finite elements method (XFEM) for fictitious domains. This method is described in the work of Wall et al. [42] and combines the advantages of the FD formulation with the XFEM developed for crack simulations, without forcing the crack to correspond to the grid line. With this method, the fluid-structure interface is treated as a crack. As the body surface position can be easily and precisely tracked from the structural domain in the FD approach, the formulation of the fluid elements which are crossed by the interface is modified at each time-step. In these elements, enriched finite-element basis functions are defined, obtained as standard basis functions multiplied by a jump function at the interface. The unknown coefficients of the enriched basis functions represent the discontinuities of the interface in the

domain. The main advantage of this technique is the decoupling of the solid and the surrounding fluid without the need to physically subdivide the fluid elements in the neighborhood of the interface, as done in the cut-cell methods.

For simplicity reasons, in the following we generically refer to these methods as IB or fixed grid methods.

2.4 Solving problems in deforming domains: fluid-structure interaction simulations

If the motion/deformation of the structure is not known a priori and it is calculated in the simulation, the mutual interaction between the two domains is computed. This simulation type is known as FSI simulations and it requires the knowledge of the mechanical properties of the solid material. In this section, we will briefly describe the structural equations and the conditions that have to be applied on the interface to couple the two domains.

2.4.1 Computational solid mechanics model

A CSM method is the most common approach for numerical simulations of deforming solid materials. As the Lagrangian method is used in the CSM and structural solver of FSI presented in this work, the equations of the following section are reported in the Lagrangian frame (chapter 2.1). The Lagrangian derivative (material derivative) with this formulation of a generic function y can be calculated as ($\vec{v_s}$ is the velocity of the solid):

$$\frac{Dy}{Dt} = \frac{\partial y}{\partial t} + \vec{v_s} \cdot \nabla y \tag{2.9}$$

The displacement of a solid material $\vec{u_s}$ is determined by the momentum equation:

$$\rho_s \frac{D^2 \vec{u_s}}{Dt^2} - \nabla \cdot \bar{\sigma_s} = \vec{f_s} \tag{2.10}$$

where ρ_s is the density of the material, $\bar{\sigma_s}$ the Cauchy stress tensor of the solid and $\vec{f_s}$ the body forces. In the cases under investigation in this thesis, $\vec{f_s}$ represents gravity, which can be neglected as its effect is generally negligible compared to the other factors present in the problems at hand.

For any solid structure, the configuration $\vec{x}$ at the current time t, is represented as a function of time and of the initial undeformed configuration $\vec{X}$. Therefore, the deformation $\vec{u_s}$ is calculated as the difference between the current and the initial (undeformed) configuration, as:

$$\vec{u_s}(\vec{X}, t) = \vec{x}(\vec{X}, t) - \vec{X} \tag{2.11}$$

The deformation gradient tensor $\bar{F}$ is then equal to $\bar{F} = \frac{\partial \vec{x}}{\partial \vec{X}}$. Its determinant is J, which expresses the relative change of an infinitesimal volume and it is a measure for the local compression of the material.

The Cauchy stress tensor $\bar{\sigma}_s$ links the forces in the deformed configuration to areas in the deformed configuration. The second Piola-Kirchhof stress tensor $\bar{S}_s$ relates the forces and the areas in the reference configuration. The relation between the two tensors is:

$$\bar{S}_s = J\bar{F}^{-1}\bar{\sigma_s}\bar{F}^{-T} \tag{2.12}$$

In large deformation theory, the relation between the second Piola-Kirchhof stress tensor $\bar{S}_s$ and the Green-Lagrange strain tensor is provided by the constitutive law of the material. The Green-Lagrange strain tensor is defined as:

$$\bar{\epsilon_s} = \frac{1}{2}[\nabla\vec{u_s} + (\nabla\vec{u_s})^T + (\nabla\vec{u_s})^T\nabla\vec{u_s}] \tag{2.13}$$

which in case of small deformation can be linearized as:

$$\bar{\epsilon_s} = \frac{1}{2}[\nabla\vec{u_s} + (\nabla\vec{u_s})^T] \tag{2.14}$$

The most simple stress-strain relationship is the one describing the behavior of linear elastic materials, i.e. a constant relation between stress and strain.

2.4.2 Boundary conditions at the FSI interface

In FSI cases, the solid and the fluid equations are solved for a solid (Ω_s) and a fluid (Ω_f) domain, bounded by Γ_s and Γ_f respectively, which share one or more interfaces Γ_i (Fig. 2.4).

Appropriate interface conditions on Γ_i have to be defined to ensure the interaction of the two domains and the equilibrium of the solution at the interface. This can be achieved with different modalities, depending on the adopted techniques to solve the PDEs system.

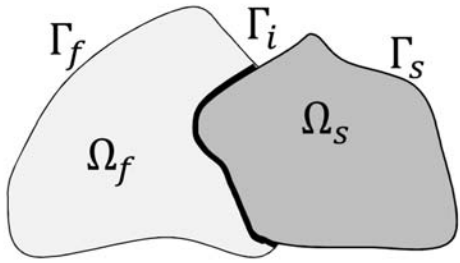

Figure 2.4: Schematic representation of a solid (Ω_s) and a fluid (Ω_f) domain, bounded by Γ_s and Γ_f respectively, which share one or more interfaces Γ_i.

In particular, if the solid and fluid equations are solved simultaneously as one global set of equations, the FSI approach is called monolithic, while if the CFD and CSM equations are solved separate, it is called partitioned. In the monolithic approach, the mutual interaction of the two domains is included into the system's equations, with an overall increase of the stability of the solution. No outer loop iterations are needed at the interface to guarantee the equilibrium conditions between fluid and solid. On the other side, the FSI simulation can be based on a partitioned approach. The fluid and the structural PDE systems are solved separately. At the interface, a Dirichlet-Neumann boundary condition is imposed, to guarantee the continuity of displacements and forces between the two domains. The Dirichlet boundary condition (imposing displacement/velocity) is applied at the fluid interface, while the Neumann condition (imposing traction at the interface) is applied on the solid domain. The equilibrium conditions applied on Γ_i are summarized as:

$$\vec{u_f} = \vec{u_s} \tag{2.15a}$$

$$\bar{\sigma_f} \cdot \vec{n_f} = -\bar{\sigma_s} \cdot \vec{n_s} \tag{2.15b}$$

with $\vec{n}_{f/s}$ the normal of the interface element pointing outward of the respective domain. Equation 2.15a forces the positions of the fluid at the interface to be equal to the position of the solid at the same location. Equation 2.15b forces the equilibrium of the traction forces at

the interface. A partitioned coupling system provides higher flexibility over the simulation: it is in fact possible to combine existing CSM and CFD codes to separately solve the two problems and coupling them at the fluid-structure interface. However, the requirement of coupling iterations at the interface increases the computational time [43] and can have a negative effect on the stability of the solution.

Most of the partitioned FSI approaches can be classified as an explicitly (weakly) or implicitly (strongly) coupled formulation. In explicit coupling codes, one coupling iteration (fluid – solid – next time-step) is performed at the interface, resulting in one iteration per time-step. This results in a faster solution, which does not, however, necessarily guarantee the equilibrium condition at the interface (equations 2.15a and 2.15b) nor a stable solution. In implicit (strongly) coupled algorithms, on the other hand, the equilibrium conditions at the interface are imposed on both the fluid and the solid domain. The presence of an iterative process (coupling iterations) at the interface guarantees the convergence of the boundary conditions at the interface, resulting in an equilibrium condition of forces and displacements at every time-step. There are several techniques which can be adopted to iteratively solve the equilibrium at the interface. The reader is referred to [26] for more details.

The solution of the PDEs system for the FSI simulation can be solved with different approaches. For the purposes of this thesis, the description of the techniques used in the described works is provided. In depth analysis is beyond the scopes of this work and references are provided for further details.

2.4.3 Overview of the techniques and algorithms used in this work

In this work, new techniques have been developed starting from existing procedures. All the models presented in Part II are based on existing numerical algorithms. The comparison of ALE- and fixed grid-based solvers for heart valves with flexible leaflets has been introduced for the first time in this work. Concerning Part III, the described CFD model with prescribed moving boundaries is based on segmented images obtained with a validated automatic segmentation method published in the work of Pouch et al., [44]. The candidate did not contribute to the development of this segmentation tool. All the simulations are performed within the well-known finite-volume CFD solver Fluent (ANSYS, Inc., Canonsburg PA, USA). The procedure and methodology described in Part III is original and has

been developed in this work to obtain a CFD model with prescribed moving boundaries to study the intraventricular flows in pathological cases.

For the arbitrary Lagrangian-Eulerian fluid-structure interaction (ALE-FSI) simulations presented in chapter 4, the interface Quasi-Newton method, with a Least-Square method for the approximation of the Inverse of the Jacobian (IQN-ILS) was used [26]. The procedure is based on the interface quasi-Newton iterations and the estimation of the inverse of the Jacobians of the solvers is approximated by means of least-squares models. The resulting FSI simulation is a strongly coupled algorithm which supports the interaction of any CFD and CSM solver, in particular for this work, Fluent 15.0 (ANSYS Inc., Canonsburg PA, USA) and Abaqus 12.0 (Dassault system, Providence, RI, USA) were used. At the interface the Dirichlet-Neumann condition is imposed 2.15a and 2.15b). The solid mesh is modelled in a Lagrangian frame, while for the fluid mesh an ALE approach is adopted. Therefore, the fluid grid is allowed to deform in the vicinity of the solid mesh and the remaining of the mesh is moved according to a spring smoothing method (Fig. 2.2 b). The advantages of the selected numerical scheme are detailed in the work of Degroote et al., [26][45]. The solvers and the numerical scheme have been tested in different application fields, including cardiovascular applications [46][47].

For the immersed boundary fluid-structure interaction (IB-FSI) simulations presented in chapter 4, one of the modules available in the commercial software Abaqus was used, in particular the coupled Eulerian-Lagrangian (CEL) module. It is an extension of Abaqus/Explicit and it combines Eulerian and Lagrangian elements for different materials in the same simulations, which result, in case of a fluid and a solid, in FSI simulations. The approach is monolithic, with the solid and the fluid equations solved simultaneously [48]. The discretization of the fluid grid is obtained with Eulerian elements. To account for the presence of the solid in the fluid domain, a volume-of-fluid (VOF) function is defined in the fluid domain. The function assumes a value of 0 if the cell is empty (fully "covered" by the solid) or 1 if it is filled with fluid (no solid overlap). A value between 0 and 1 can be assigned if the structure partially overlaps with the fluid cell (Fig. 2.5). The imposition of the equilibrium conditions at the interface is obtained by enforcing a contact function between the solid and the fluid domain.

For the CFD simulations described in chapters 7 and 8, Fluent 15.0 (ANSYS Inc., Canonsburg PA, USA)was used for the calculations.

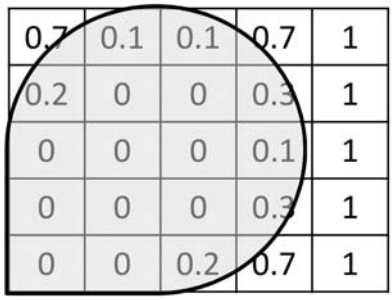

Figure 2.5: Schematic description of the VOF function. In grey the cells "covered" by the solid.

The additional functions described in chapter 7 and in appendix A are implemented via user-defined function (UDF)s, which are external functions available in Fluent, to allow the user to modify the solver.

2.5 Discretization schemes

2.5.1 Finite volumes and finite elements

In this work, all the CFD equations are discretized with a finite volume method (FVM). The mesh is considered as a set of control volumes and all the quantities (variables calculated in Fluent such as pressures and velocities) are calculated in the center of each cell. For the solution, the face-centered values (needed to solve the set of equations) are obtained using interpolation. All the CSM and IB-FSI described in this work are obtained with a finite element method (FEM) available in Abaqus (Standard and Explicit). The computational mesh is subdivided in a set of elements and in each element the solution is formulated based on expansion basis functions [49].

2.5.2 Time discretization

In all the described CFD simulations, ALE-FSI simulations and CSM simulations the time domain is discretized with a first order implicit backward scheme. On the contrary, for the IB-FSI simulations an explicit time integration scheme is used. Given an ordinary differential equation:

$$\frac{dy}{dt} = f(y) \tag{2.16}$$

for which the initial values y_0 and t_0 are known, an (Euler) implicit time integration scheme expresses the approximated value of $y(t + \Delta t)$ as 2.17

$$y(t + \Delta t) = y(t) + \Delta t \cdot f(y(t + \Delta t)) \tag{2.17}$$

This discretization is called implicit, as iterations are required to calculate the new value of y for every time-point until convergence is reached. If the (Euler) explicit time integration scheme is used, the approximated value of $y(t + \Delta t)$ becomes 2.18

$$y(t + \Delta t) = y(t) + \Delta t \cdot f(y(t)) \tag{2.18}$$

In this case, on the contrary, no iterations are required and the new value of y can be directly calculated.

II

FSI simulations on bioprosthetic aortic valves

Chapters

Chapter 3

FSI simulation of aortic valves

3.1 Introduction

With more than 25% of the elderly population (>75y) being prone to aortic valve diseases in the US alone [1][2], there is a great interest in the investigation of the valvular structures and their fluid mechanics. In particular, the optimization of prosthetic devices is of great interest, as the replacement of the valvular apparatus is one of the most common treatments for valvular pathologies (chapter 1.2). Prosthetic heart valves have been used and studied since the 1950s, when they were firstly developed and implanted [50]. Despite the long clinical experience and knowledge of the devices, there are still several drawbacks that need to be investigated in order to improve the performance and the outcomes of the surgical implantation. The more recent biological prosthetic valvular devices, manufactured with biological tissues (Fig. 1.7b), have been developed to guarantee a greater biocompatibility and a reduced interference with the haemodynamics of the AR when compared to the mechanical prosthetic valves. Nevertheless, they show durability issues as the tissue deteriorates with time, losing their mechanical properties. In this work, the attention is focused on biological prosthetic aortic devices, analyzed with FSI simulation to investigate the mutual interplay of the soft tissues and the blood flow [36][39][51][52][53][54][55].

In the past decade, a number of numerical simulations have been performed to analyze the performance of idealized, native or prosthetic

aortic valves. The most commonly adopted discretization technique for the fluid domain is the IB/FD approach, as it reduces the computational complications related to the fluid grid motion. In fact, only the structural grid deforms, it has lower computational cost, and there are no issues related to a highly deformed fluid grid, making the technique more suitable for problems where the structural domain undergoes large displacements, as in case of heart valve dynamics studies [36][51] [52] [53] [54] [55] [56][57]. However, for a biomedical application such as heart valve (HV), with analysis of quantities such as wall shear stresses and pressures, the choice can have some disadvantages.

As abnormal WSS regimes can provoke valve calcification [58] [59] [60], the accuracy of WSS on the valvular leaflets can have a clinical and diagnostic importance. Therefore, the velocity field near the valvular leaflets has to be highly resolved and the location of the surface has to be known exactly [61]. Furthermore, the ALE technique guarantees a good representation for the pressure field, whereas the IB methods do not always ensure pressure stability at the interface, especially if large pressure differences have to be sustained [37][62]. These considerations suggest that, apart from the mesh motion issues, the ALE technique would be preferable to perform heart valve simulations as the interface is sharply defined, and the formulation allows to compute a realistic pressure field, especially if pressure jumps across the interface are involved. An alternative would be to discretize the fluid grid with an Eulerian approach, while allowing a local mesh refinement in the proximity of the moving walls, in order to improve the quality of the definition of the surface in the fluid domain and overcome some of the major limitations of the IB formulation [37].
In the remainder of this section, a brief state of the art of FSI simulations for BHV is presented. It does not intend to be exhaustive, it has the scope to provide a brief overview on the current status of the research in the field. In particular, the solution methods are highlighted, when available.

3.2 State of the art: IB-FSI simulations

3.2.1 2D models

Since the technique was firstly explored in the work of Peskin [33], the majority of the published works on FSI simulations of aortic valves rely on the IB method for the fluid discretization [51] [52][53] [54] [56][57] [63]. Both two-dimensional (2D) and 3D models are available. In the work of De Hart et al.,[64], a two-dimensional model of a

simplified heart valve is presented. The fluid domain consists of a straight tube with semi-circular enlargements (sinuses of Valsalva), discretized with a fixed Eulerian grid, while the flexible structure is anchored at the annulus location and it is free to move on top of the fluid grid (Fig. 3.1a) with a FD approach. Its effects on the blood are included via Lagrangian multipliers. The systolic phase was simulated and the major features of the obtained flow field were validated with an in vitro experimental set-up. An example of the resulting velocity flow field is shown in Fig. 3.1b. The method has been extended to the 3D case and simulation of a 3D heart valve [56].

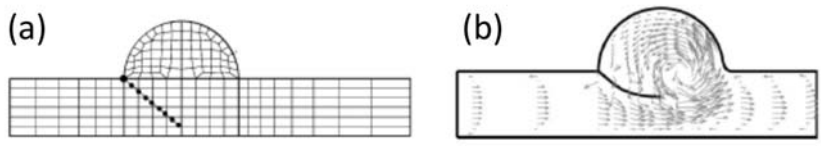

Figure 3.1: (a) Computational domain (b) velocity vectors during the deceleration phase (adapted from [56])

In the work of van Loon et al. [37], the authors developed a procedure to implement (at least in 2D) a technique based on the fictitious domain approach with a local remeshing at the interface (chapter 2.3.2). This technique allows for a better representation of the pressures and the WSS at the interface between the solid and the fluid, as compared to the standard FD approach [37]. In Fig. 3.2 the streamlines (a) and the pressures (b) in a 2D fluid domain in which a flexible slab is allowed to move are reported. The technique allows for realistic pressure distribution especially in the region across the thin valve [59]. In this work the contact of solid bodies is explicitly discussed and included in the computation [65].

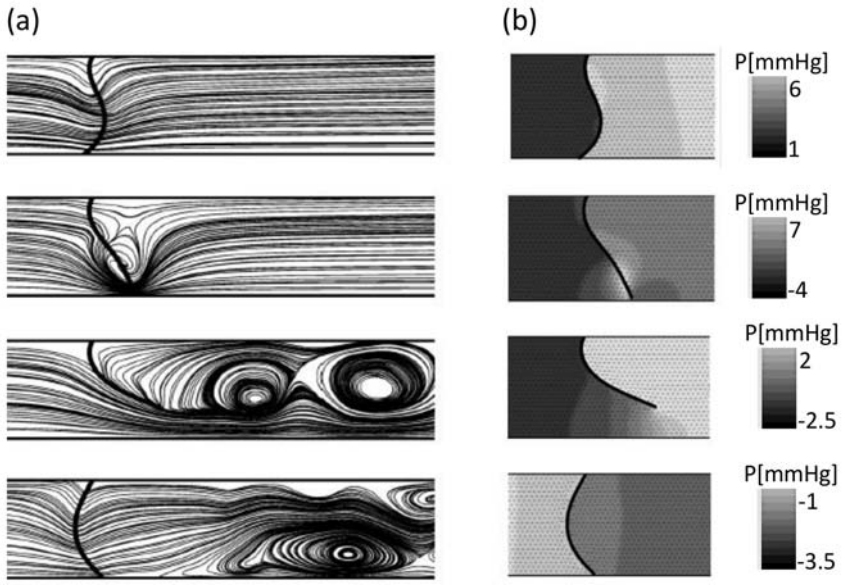

Figure 3.2: (a) Velocity streamlines and solid slab position at four time points, (b) corresponding pressure distribution in the domain (adapted from [59])

Similar tests on 2D flexible thin structures is presented in the work of Dos Santos et al.,[55], where the fluid domain is modelled with a FD scheme (the kinematic continuity is enforced via Lagrangian multipliers). No adaptation of the mesh is proposed, but the comparison of the FD model and the corresponding ALE model show good agreement (Fig. 3.3), at least in terms of displacements and velocities in the 2D case. No pressure comparison is reported in this work. The contact detection is included in the FSI algorithm and does not rely on the contact capabilities of the structural solver [55].

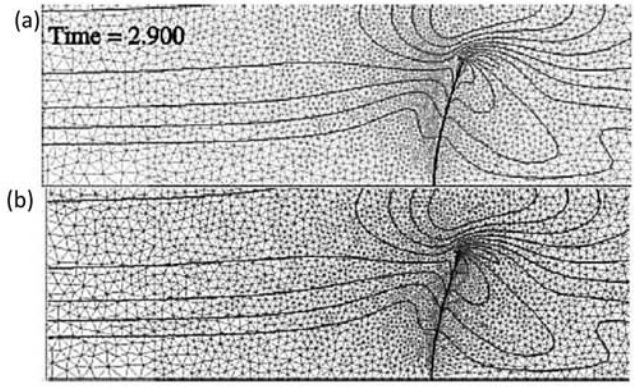

Figure 3.3: Comparison of velocity iso-values for a moving slab in a fluid domain, modeled with (a) the FD method and (b) the ALE method (adapted from [55])

3.2.2 3D models

In recent years, more complex and complete 3D simulations have been proposed. In the work of Marom et al. [54] the authors propose a quite complete 3D model of the aortic root and the aortic valve, whose leaflets are modeled with a fiber-reinforced material model, to provide a more physiological mechanical response. The elasticity of the aortic root is also taken into account, with a hyperelastic and isotropic behavior. The geometry of the aorta is simplified to a straight tube with enlargements for the sinuses and it is based on geometric relationships and normal dimensions, while the valve is simplified but without symmetry assumptions (Fig. 3.4a). To enhance convergence, a limited amount of compressibility of the fluid is introduced. The effects of the introduction of artificial compressibility in FSI simulations is discussed in more detail in chapter 5. The fluid grid is a non-uniform Eulerian mesh, very refined in the vicinity of the moving walls (aortic walls and valvular cusps). The FSI algorithm chosen is a weakly coupled partitioned solver, with no coupling iterations at the interface. The structural equations are solved by Abaqus 6.10(Simulia, Providence, RI, USA), while FlowVision HPC 3.08 (Capvidia, Leuven, Belgium) was the flow solver. FlowVision Multi-Physics manager (Capvidia, Leuven, Belgium) managed the coupling of the two codes. The WSS on the valvular leaflets are reported in Fig. 3.4b at peak of systole, with a maximum value of about 20Pa, while in Fig. 3.4c the resulting pressure distribution in the AR is shown.

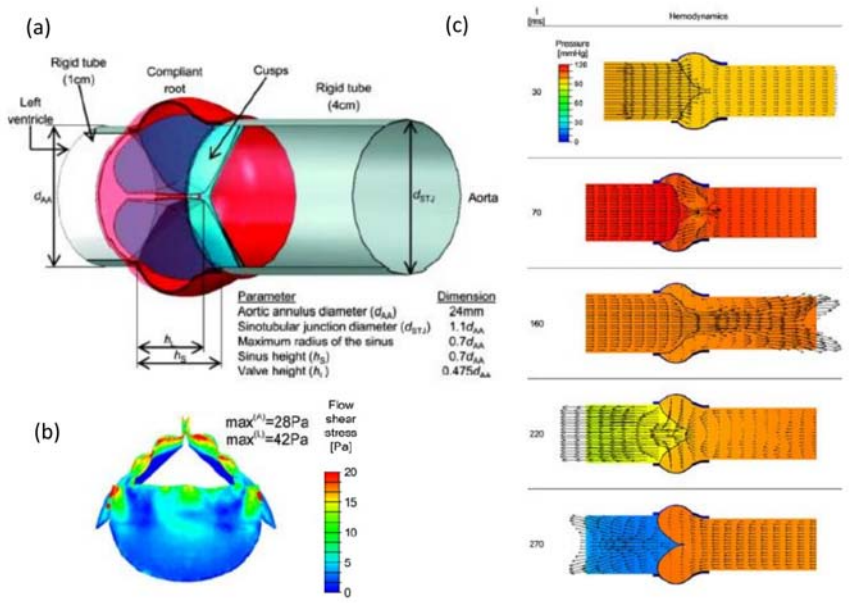

Figure 3.4: (a) 3D geometry of the aortic root and aortic valve, (b) WSS on the valvular leaflets at peak systole, (c) pressure distribution and velocity vectors on the midplane of the valve at five time-points of the cardiac cycle (adapted from [54])

To improve the performances of the IB methods and to guarantee an adequate representation of the interface, a number of sharp-interface IB methods have been proposed (chapter 2.3.2). Among others, [39] and [36] propose a curvilinear staggered grid discretization approach to solve the NS equations. The method is based on the work of Gilmanov et al.[38], in which the immersed surface is triangulated and its nodes constitute a set of Lagrangian control points to track the position of the surface itself. The method has been successfully applied to simulate MHV [39] and BHV [36]. In Fig. 3.5a, the model of the BHV is reported, while in Fig. 3.5b, the instantaneous local shear is reported at the midplane of the valve at four time-points during systole.

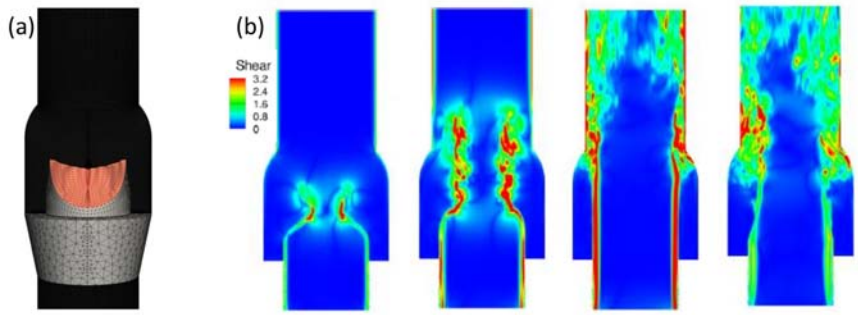

Figure 3.5: (a) 3D model of a BHV inserted in a simplified aortic root geometry, (b) maximum instantaneous local shear over the midplane at four time-points in systole (adapted from [36])

Commercial software are available to perform FSI simulations. In the work of Sturla et al.[53], the explicit, finite-elements software LS-DYNA (LSTC, Livermore CA, USA) has been used. It is a weakly coupled solver, using a penalty-based coupling approach for the fluid-structure interaction. LS-DYNA provides the possibility of a combined approach for the simulation: it is in fact possible to use the ALE approach to model the elasticity of the aortic walls and the IB technique to simulate the large displacements of the valve. In this work, a limited amount of compressibility was added to the fluid domain to improve the stability of the solver. The geometrical model used is simplified, but it includes the curvature of the proximal aortic arch, to add asymmetric features to the downstream boundary conditions. As shown in Fig. 3.6a, the computational domain includes the aortic valve and aortic root (with the curvature of the proximal arch. In Fig. 3.6b and c the pressures and velocities are reported.

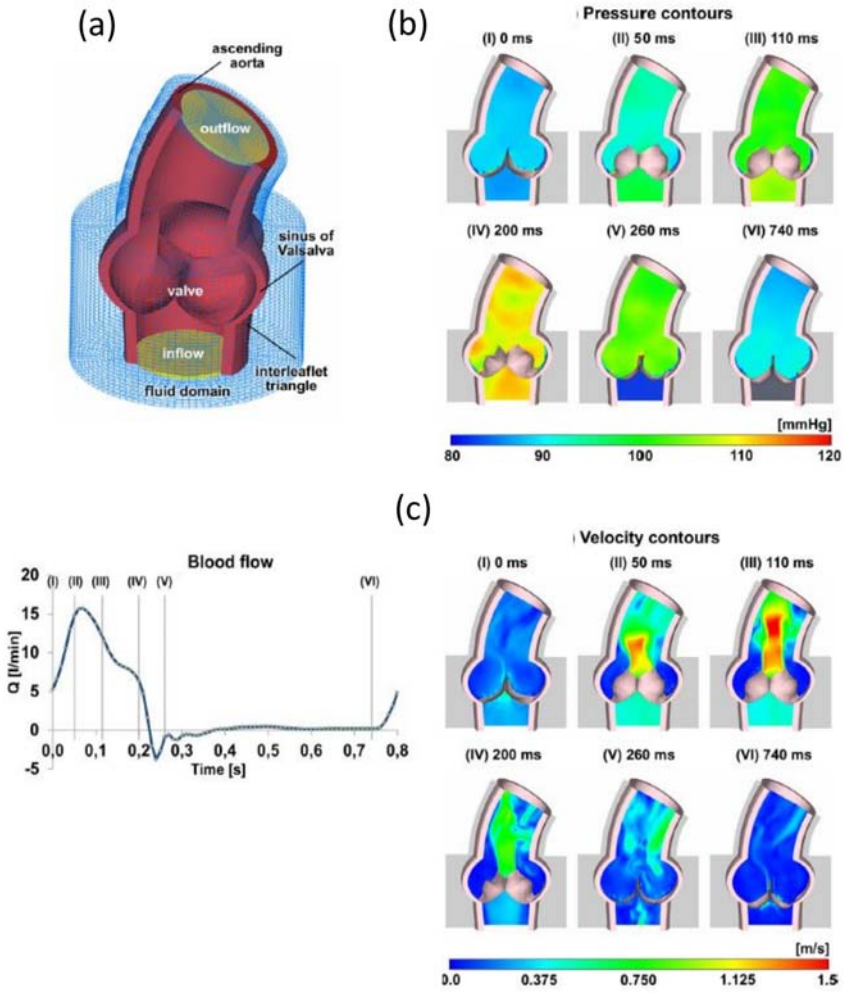

Figure 3.6: (a) Computational domain of the aortic root and the valve, (b) pressure field and (c) blood velocity on a longitudinal section at six time-points indicated in the graph (adapted from [53])

LS-DYNA is also used in the work of Wu et al.[57], where the aortic root of a patient is reconstructed from computed tomography (CT) clinical images (Fig. 3.7a). The valve, on the other side, is derived from a real prosthetic device. Before the FSI simulation, the valve is deployed in the aortic root with a CSM simulation (Fig. 3.7b), to provide the initial stress conditions on the stent struts of the valve and on the aortic walls as initial conditions. The resulting pressure field (Fig. 3.7 c), the velocity contour on a vertical section (Fig. 3.7 d) and the velocity streamlines (Fig. 3.7e) are displayed.

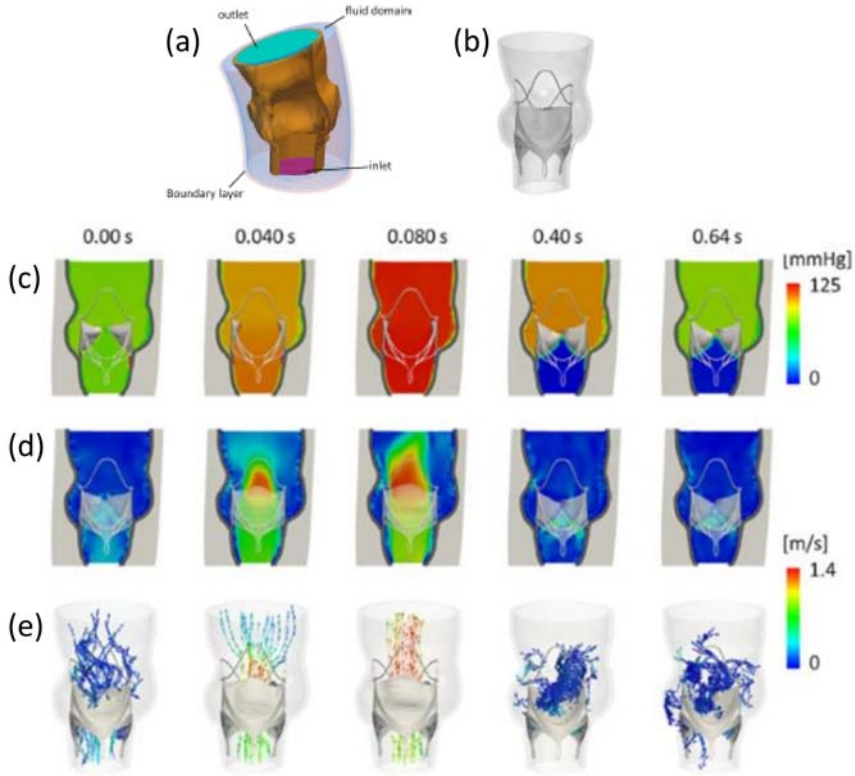

Figure 3.7: (a) Patient-specific geometry reconstruction, (b) prosthetic valve virtually implanted in the AR, (c) Pressure distribution on a vertical section, (d) velocity contours on a section and (e) streamlines in the AR (adapted from [57])

3.3 State of the art: ALE-FSI simulations

3.3.1 2D models

While the ALE approach has been successfully used for vascular simulations [43] [66], only few studies are reported in literature on valvular simulations.

A 2D model of a native AV based on the ALE formulation is reported in [67]. The geometry is proposed in Fig. 3.8a, and consists of a section of a pre-existing 3D model. The FSI simulation is performed with the commercial software ADINA (ADINA R&D, Watertown, MA), with a strongly coupled and partitioned coupling algorithm between the Lagrangian structural solver and the ALE-based fluid solver. The results are shown only for the peak of systole and during

diastole (Fig. 3.8 b-c). Among the goals of this work is the quantification of the WSS on both sides of the valvular leaflets. In this case, the peak value is about 3.5Pa. No indication is provided on the contact treatment during diastole.

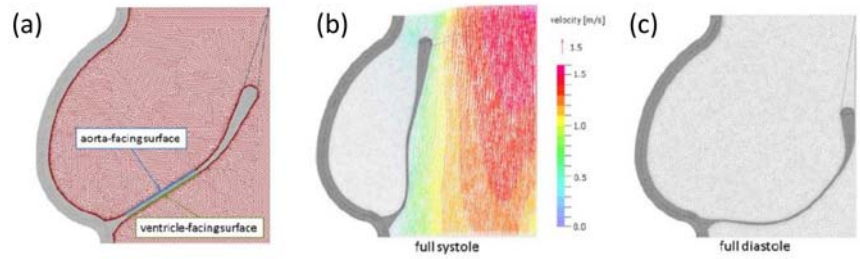

Figure 3.8: (a) 2D fluid and solid mesh, (b) velocity vectors at peak systole, (c) velocity vectors during diastole (adapted from [67])

A 2D model of the AV with flexible leaflets (Fig. 3.9a) based on the ALE formulation can be found in the work of Chandra et al. [60], the FSI simulation is performed with the commercial software ADINA (ADINA R&D, Watertown, MA), with a strongly coupled and partitioned coupling algorithm between the Lagrangian structural solver and the ALE-based fluid solver. In this work, the cycle is limited to the systolic phase and no contact of the leaflets is considered. Despite the two-dimensionality of the problem and the simplifications related to the valvular material properties and boundary conditions, the study proposes a comparison between a healthy HV and a bicuspid (two valvular leaflets instead of three) valve, with different levels of calcification. The results identify the differences in WSS magnitude and pulsatility in different regions of the leaflets and calculated, together with the WSS, significant parameters to classify the valvular pathology. In Fig. 3.9b the WSS at peak of systole is shown (peak of WSS on the ventricular side of the valve of about 8Pa) and in Fig. 3.9c-e the velocity contours are shown for a natural physiological AV during systole.

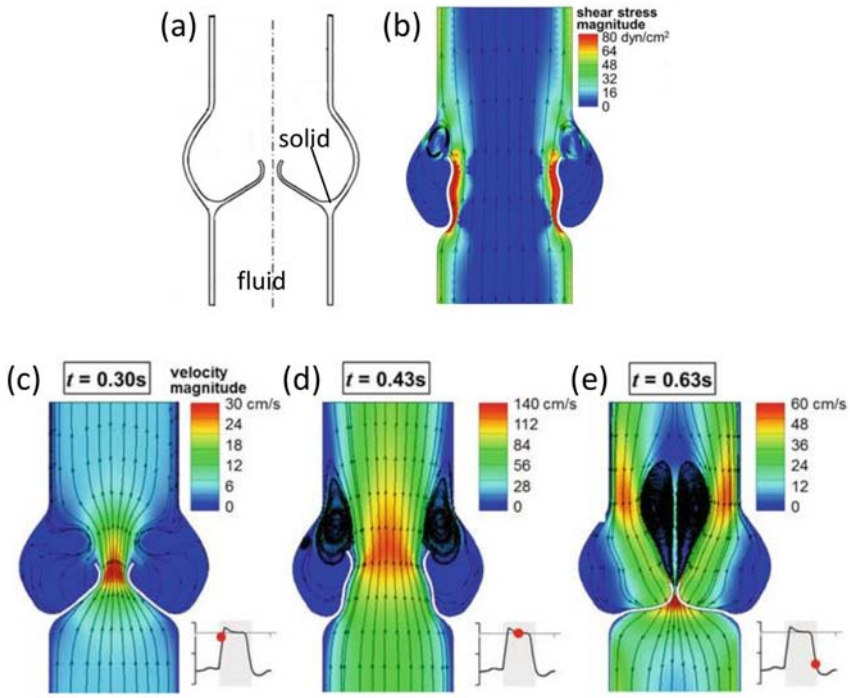

Figure 3.9: (a) 2D geometry. (b-d) velocity contour at three time-points in systole. (e) WSS at peak systole. (adapted from [60])

3.3.2 3D models

More recently, the same research group published a study on 3D FSI simulations of native aortic valves based on the ALE approach [61]. From the numerical point of view, the FSI algorithm chosen is a strongly coupled, partitioned coupling algorithm, provided by the commercial software ANSYS 15.0 (ANSYS, Inc., Canonsburg, PA, USA). The three-dimensional model assumes the symmetry of the valve and the aortic root (Fig. 3.10a). The material of the leaflets is non-linear, while the distensibility of the aorta is taken into account with a linear elastic and isotropic material. The full cardiac cycle is simulated and the results provided the flow field in the entire domain. The velocity streamline on a vertical section are reported in Fig. 3.10b. The WSS on the cusps was also analyzed, the total WSS on the ventricular side of the leaflets is shown in Fig. 3.10c, with a peak of about 12Pa at the free edge of the leaflets at peak systole.

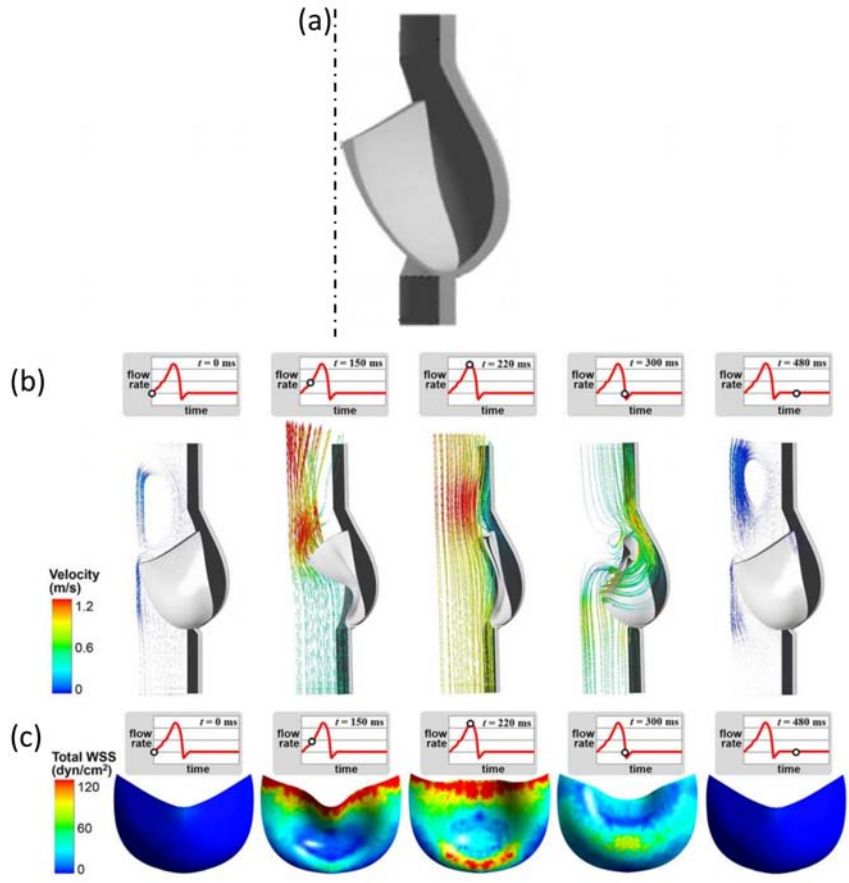

Figure 3.10: (a) 3D symmetric geometry. (b) velocity streamlines on a vertical section at five time-points in systole. (c) WSS at peak systole on the ventricular side of the valvular leaflets (adapted from [61]).

In [61], the contact of the valve during diastole is enforced between the leaflet and the symmetry plane with frictionless properties, probably managed with automatic functions available in the commercial software.

3.4 Overview

The most relevant features of the described models available in literature are briefly summarized in table 3.1.

Table 3.1: Overview of the FSI simulations described in Chapter 3

		Code	Discretization method	FSI method	Geometry	Contact	Constitutive law – valve	Constitutive law – aorta	Peak Re	Compressibilty
2D	De Hart 2000 [62]	Based on [33]	FD	Monolithic	2D Simplified	No	Linear elastic - massless	Rigid	800	N/A
	Van Loon 2004 [35]	Based on [33] + local remeshing	FD with local remesh	Monolithic	Straight tube with slender body	Ad hoc	Hyperelastic, neo-hookean	Rigid	1000	N/A
	Dos Santos 2008 [53]	In house	FD(valve) + ALE(wall)	Strongly coupled partitioned - Lagrangian multipliers	Straight tube with slender body	Ad hoc	Linear elastic	Rigid	N/A	N/A
3D	Marom 2013 [52]	Abaqus and FlowVision	FD	Partitioned, weakly coupled	Idealized but no valvular symmetry	Master-slave algorithm	Fiber reinforced material	Isotropic hyperelastic	<3000	Yes
	Borazjani 2013 [34]	Based on [37]	CURVIB/sharp interface	Strongly coupled stabilized with Aitken acceleration technique	1/3 symmetry and straight tube	Ad hoc	Anisotropic Fung-type non-linear + damping	Rigid	6000	N/A
	Sturla 2013 [51]	LS-Dyna	ALE+IB	Strongly coupled	Asymmetric MR-based	Automatic scale-penalty contact method	Hyperelastic anisotropic	Linear elastic isotropic	4500	Yes
	Wu 2016 [55]	LS-Dyna	ALE+IB	Strongly coupled	Patient-specific aorta and device-specific valve	Self contact	Elastic model (silicon)	Aorta: elastic; stent (Nitinol): superelastic properties	N/A	Yes
2D	Weinberg 2010 [65]	Adina	FE ALE	Strongly coupled	2D Simplified and symmetric	N/A	Exponential Mooney-Rivlin material	Rigid	N/A	N/A
	Chandra 2012 [58]	Adina	ALE	Strongly coupled	2D Simplified and symmetric	No / systole only	Isotropic and linear elastic	Isotropic and linear elastic	N/A	N/A
3D	Cao 2015 [59]	ANSYS	ALE	Strongly coupled	1/3 symmetry and straight tube	Frictionless	3 parameter incompressible Mooney-Rivlin model	Linear elastic isotropic	6262	N/A

Chapter 4

Comparison Between IB and ALE Techniques for the Mesh Representation.

In this chapter the implementation of a model of a biological prosthetic aortic valve with flexible leaflets is proposed in both a 2D and 3D scenario. In particular, the goal is to perform comparable simulations with the ALE-based technique available within our group [45] and the IB techniques as present in the commercial solver Abaqus/CEL, release 12.0. This chapter is based on the published paper *"Fluid-structure interaction simulation of prosthetic aortic valves: comparison between immersed boundary and arbitrary Lagrangian-Eulerian techniques for the mesh representation"*[*] [5].

4.1 Introduction

From a methodological point of view, the choice of the fluid discretization has a great importance when performing FSI simulations of HV, as described in chapter 3. The goal of this section is to describe the

[*] A. M. Bavo, G. Rocatello, F. Iannaccone, J. Degroote, J. Vierendeels and P. Segers, 'Fluid-Structure Interaction Simulation of Prosthetic Aortic Valves: Comparison between Immersed Boundary and Arbitrary Lagrangian-Eulerian Techniques for the Mesh Representation', *Plos One*, vol. 11, no. 4, e0154517, 2016

same aortic valve model in the two cases, comparing the performances of an ALE-based FSI solution and an Eulerian-based FSI approach. In Fig. 4.1, the IB and the ALE fluid domain are represented in the case of a 2D heart valve, in the undeformed (left panel) and deformed (right panel) configuration.

After a first simplified 2D case, the aortic geometry was considered in a full 3D set-up. The model was kept as similar as possible in the two settings, to better compare the simulations outcomes. Although for the 2D case the differences were unsubstantial, in our experience the performance of a full 3D ALE-FSI simulation was significantly limited by the technical problems and requirements inherent to the ALE formulation, mainly related to the mesh motion and deformation of the fluid domain. As a secondary outcome of this work, it is important to point out that the choice of the solver also influenced the reliability of the final results.

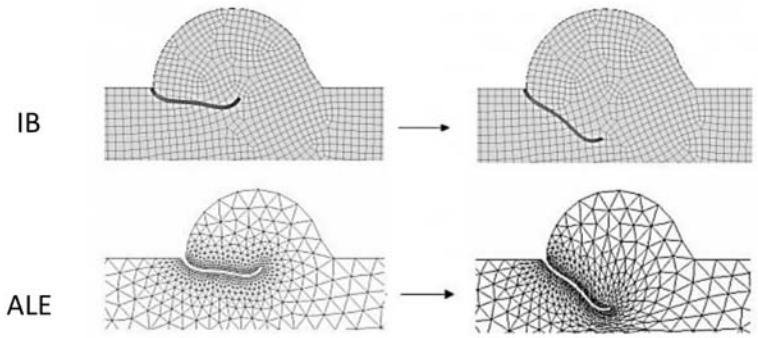

Figure 4.1: Grid formulation for the IB (upper panel) and the ALE (lower panel) methods, in two consequent time-steps (from left to right) for the 2D aortic valve with flexible leaflets.

4.2 Materials and methods

4.2.1 FSI solver

In this work, all the IB-based simulations were performed within the Abaqus/CEL environment, an extension of the module Abaqus/Explicit version 12.0 (Dassault Systèmes, Providence, RI, USA). This module does not couple multiple software products, but solves the interaction simultaneously within Abaqus [48], imposing the interaction between the two domains with contact constraints (chapter 2.4.3). The ALE simulations were performed with a strongly

coupled and partitioned solver, which makes use of an in-house written coupling algorithm (using IQN-ILS, as implemented in Tango [45]) to couple any two black box solvers. In particular, Fluent (Ansys, release 15.0) and Abaqus/Standard version 12.0 (Dassault Systèmes, Providence, RI, USA) were used in this work (chapter 2.4.3). The convergence criterion for the coupling algorithm in the case of interest was the reduction of the norm of the change in interface displacement with a factor 10000 relative to the value obtained in the first coupling iteration. The performance of this FSI framework has been tested and verified in numerous works with different applications, including the biomedical field [45] [47][46]. With regard to the deforming domain of the ALE-FSI simulation, the mesh deformation was managed by the solver Fluent. Separate tests were performed to identify the most adequate set of parameters for the smoothing algorithms necessary to preserve a good quality of the fluid mesh.

4.2.2 2D and 3D models

A Carpentier-Edwards PERIMOUNT Aortic Heart Valve (Edwards, Lifesciences LLC, Irvine, CA, Fig. 4.2a) was scanned (Fig. 4.2b) with a μCT scan Triumph-II imaging system (TriFoil Imaging, Chatsworth, CA).

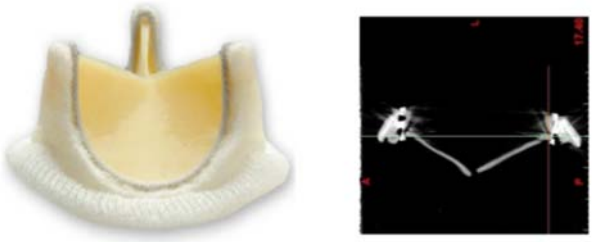

Figure 4.2: (a) Carpentier-Edwards PERIMOUNT aortic heart valve. (b) μ CT scan of the prosthetic device

The obtained images were segmented with the commercial software Mimics (Materialise NV, Leuven, Belgium) to obtain the desired 3D volume and geometry Fig. 4.3 (a). To obtain the entire domain, the valve was placed into a straight and rigid tube ($length(L) = 130mm$) with three hemispherical enlargements Fig. 4.3 (b-c), diameter $diameter(D) = 20mm$), to represent the sinuses of Valsalva [68]. The 2D model was obtained as an idealized section of

this geometry, and included two symmetric leaflets placed in a straight rigid tube with two enlargements Fig. 4.3(d). The dimensions were consistent in the IB and ALE models, and were chosen according to literature data.

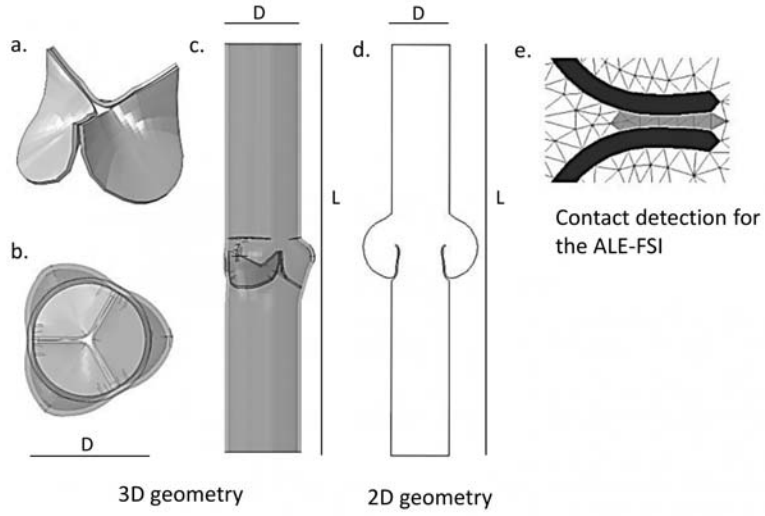

Figure 4.3: (a) Geometry of the bioprosthetic valve, (b,c): Three-dimensional geometries of the entire domain, (d) Two-dimensional domain. (e) Contact detection function for the ALE-FSI simulation. In black the leaflets, in white the fluid domain, and in grey the cells detected for contact.

The structural mesh was similar in both models and consisted of quadrilateral or hexahedral solid elements, for 2D and 3D simulations respectively. C3D8R elements were chosen for the 3D IB-FSI simulation. A set of separated tests revealed no difference between different types of elements for the case under investigation (in terms of valvular opening time). Due to the requirements imposed for the generation of an adequate fluid mesh in the IB-FSI case, it was necessary to reduce the number of the solid elements in the IB-FSI case to consequently increase the element size. More details are provided in the following sections. The fluid mesh of the ALE simulation consisted of triangular (2D) or tetrahedral (3D) elements with a higher cell density in the vicinity of the valve. Due to the ALE formulation, it was possible to obtain a non-uniformly spaced fluid grid, which reduced the overall number of elements for this mesh. The fluid mesh of the IB-FSI was made of quadrilateral 2D) or hexahedral (3D) elements. To have a satisfactory definition of the initial VOF in the IB method, a homogeneously refined fluid mesh had to be generated. This resulted in

a much more refined mesh for the IB-FSI than for the ALE-FSI. To limit the global number of Eulerian elements in the IB-FSI simulation, the fluid domain was shortened to 30 mm. The final mesh used for the IB-FSI simulation resulted in a denser and larger mesh, if compared to the mesh used in the ALE-FSI case, as reported in Table 4.1. In Fig. 4.1 (upper panel and lower panel), the 2D fluid meshes for ALE-FSI and IB-FSI are reported, respectively. The 2D meshes are reported in Fig. 4.1, in Fig. 4.4 the 3D meshes are reported in both cases.

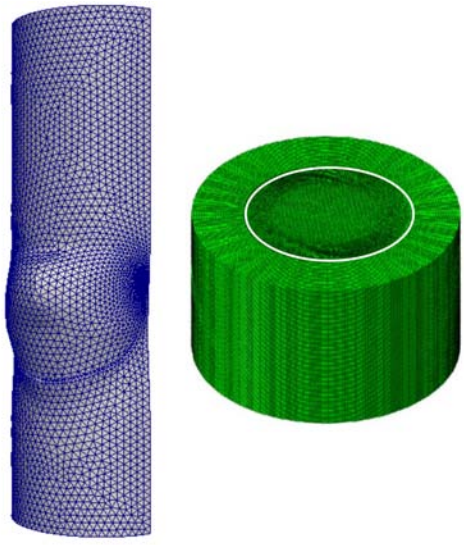

Figure 4.4: 3D meshes for (a) the ALE-FSI simulation (1/3 of the geometry) and (b) the IB-FSI simulation (location of the aortic wall in white).

Adequate dimensions of the meshes were chosen for the different set-ups. The number of elements is listed in Table 4.1. For the ALE simulations, the initial dimension of the fluid meshes is reported, as the remeshing of the domain was enabled and the number of cells thus varied during the simulation.

4.2.3 Material properties and boundary conditions

The leaflets tissue was modelled as linear and elastic (Young modulus $E = 1MPa$, Poisson ratio $\nu = 0.45$) [52][64] and a thickness of 0.5mm, while the elasticity of the aorta was neglected and the arterial walls were assumed to be rigid [69]. For the comparison purpose of this work we considered these simplifications to be justified, while for a more refined model the elasticity of the wall has to be included and

Table 4.1: Number of the mesh elements in the different set-up.

	2D		3D	
	ALE-FSI	IB-FSI	ALE-FSI	IB-FSI
SOLID	500	300	5200	1250
FLUID	2400	3500	150000	1150000

more realistic material models of the soft tissues are necessary [36] [53] [70] [71].

The blood was modelled as a Newtonian fluid ($\rho = 1060Kg/m3$, $\mu = 0.003Pa \cdot s$). In the IB-based simulation, a compressibility factor was added to the fluid to enhance the convergence of the solution [52] [53] [57]. This coefficient was set by imposing a speed of sound in the fluid $c_f = 157m/s$ in the 2D case, and of $15.7m/s$ in the 3D case (with the effective value being in the order of $1570m/s$ [72]). Chapter 5.2 is dedicated to discuss the effects of this choice.

A physiological transvalvular pressure difference curve was applied at the ventricular side of the domain, while the aortic outlet was kept at a reference pressure. Before the loading cycle, the pressure was gradually increased until the initial pressure was reached to provide a good initial condition for the simulation [73] and to reduce the influence of the compressibility of the flow [53].

A no-slip condition was imposed on the walls, while the fluid-structure interaction condition was enforced in the leaflets' region.

In the ALE-FSI, a fixed time-step size was chosen. To capture the dynamics of the valve motion and to guarantee the contact detection in the structural solver a time-step of 0.1 ms was selected. The time integration scheme used was a first-order, implicit method. In the IB-FSI an automatic and adaptive time-step was selected and an explicit integration scheme was used. An initial time-step size of 0.1 ms was chosen, coherently with the ALE-FSI. The time-step size was then automatically calculated and updated throughout the simulation by the solver.

4.2.4 Contact

The management of the contact in the two models was substantially different. The solid-solid contact in the IB-FSI was directly managed by the solver Abaqus via a default contact penalty method [48]. The contact in the ALE-FSI was not available automatically: an *ad hoc*

function was introduced to detect the areas experiencing contact, to hamper the motion of the valve and to preserve a one-layer-cell gap between the leaflets. During contact, in fact, the leaflets of the valve should close completely, and, due to the ALE formulation, this would result in the generation of highly distorted elements and, ultimately, the splitting of the fluid domain and failure of the simulation. To avoid this phenomenon, it was necessary to preserve a layer of fluid cells in the contact area of the leaflets. The kinematic constraint to hamper the motion of the valve was imposed in the structural solver with the default contact algorithm available in Abaqus/Standard. The properties of the contact were consistent with the properties of the contact definition of the IB-FSI. A minimum threshold distance between the leaflets was imposed, to preserve a gap during the diastole to avoid excessive fluid mesh distortion and mesh motion issues. However, on the fluid side, the presence of the gap introduced an unwanted and artificial leakage of the valve when it was in the closed configuration. The valve leakage can be reduced by modifying the physical properties of the cells located in the area during the coaptation phase. The hydraulic resistance was increased in these cells, to reduce the overall backflow during diastole. This could be obtained by implementing a specific external function (UDF) in the fluid solver, which detected the cells of the gap and modified their properties, with a process similar to the technique reported in the work of Wriggers et al.[74]. This function was activated only during the closed phase of the valve, when the leaflets came closer than a predefined threshold. This technique does not intend to mimic any physiological phenomenon and the permeability coefficients were chosen as a trade-off between the reduction of the backflow and the stability of the solution process. The 2D visualization of the contact function is depicted in Fig. 4.3e. The cells marked in grey were selected for contact after the kinematic constraint was imposed to preserve a minimal fluid gap and avoid the domain splitting. The permeability of these cells was modified to artificially increase their hydraulic resistance to the flow.

4.3 Results

In this section, we report the comparison between the most significant results of the two techniques in the 2D and 3D case.

4.3.1 2D simulations

The open valve was assumed to be the initial configuration. Being already open, the valve did not offer any resistance to the fluid during

the opening phase, therefore we report the results of the closing phase only, until early diastole. The results of the two simulations were comparable in terms of velocity magnitude and leaflets displacements. The flow decelerated when the pressure drop across the valve reversed, and the valve started to close (Fig. 4.5(a)). After about $0.4s$ the valve was in the closed position and a small central leakage was detected (Fig. 4.5b). The IB-FSI simulation showed a time delay in the kinematics of the valve: in this case, in fact, the leaflets reached the closed position with a delay of maximum $50ms$ in comparison to the ALE-FSI. As visible from Fig. 4.5(c), the 2D case was not suitable to simulate the diastolic configuration of the valve. In diastole, the pressure drop across the valve is significant, and the thin 2D structure was not able to keep the closed configuration, even in presence of the contact condition. For this reason, the 2D simulation was limited to the closing phase of the valve, and only one cardiac systole was simulated.

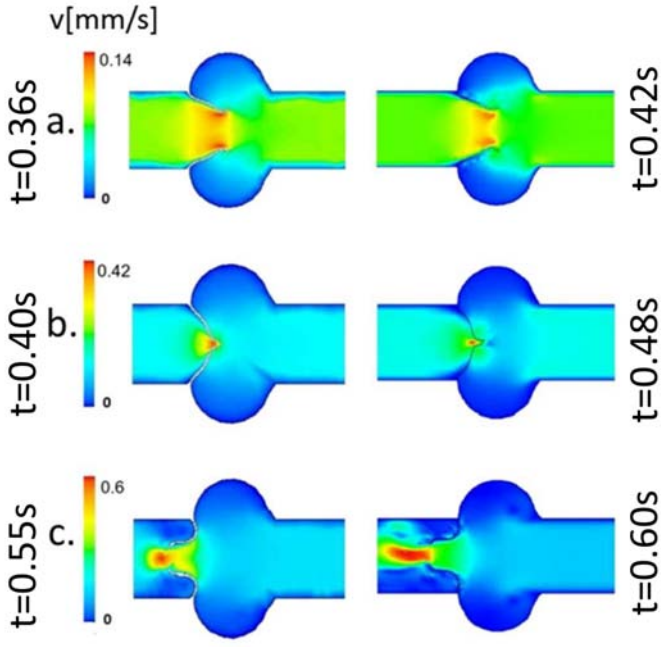

Figure 4.5: Comparison between the ALE and the IB results at (a) late systole, (b) closure phase, (c) early diastole

The IB-FSI simulation was performed with a speed of sound in the blood $c_f = 157.0m/s$, coherent with previously reported values

[53] [57] [75] [72]. This value had to be reduced to $c_f = 15.7m/s$ for the 3D set-up. To verify the influence of the increased compressibility assumption, the comparison between the two cases ($c_f = 157m/s$ versus $c_f = 15.7m/s$) was performed in the 2D model. Further discussion on the influence of the compressibility factor is reported in chapter 5.

In Fig. 4.6 the displacement of the nodulus of Arantio of the valve is reported (Fig. 4.6a), for the ALE-FSI (solid line) and for the IB-FSI (red and black for the simulations with $c_f = 157m/s$ and $c_f = 15.7m/s$, respectively). The delay of both the IB-FSI simulations with respect to the ALE-FSI is visible, while no difference in the timing is detected for the different values of the speed of sound. The delay of the IB-FSI is visible also in Fig. 4.6b, in which we report the velocity profiles during the closure phase in different sections for the ALE-FSI at $t = 0.36s$, for the IB-FSI with $c_f = 157m/s$ at $t = 0.36s$ and at $t = 0.42s$. The velocity profiles of the two types of simulations are comparable only when the IB-FSI has a time-delay of about 50ms over the ALE-FSI.

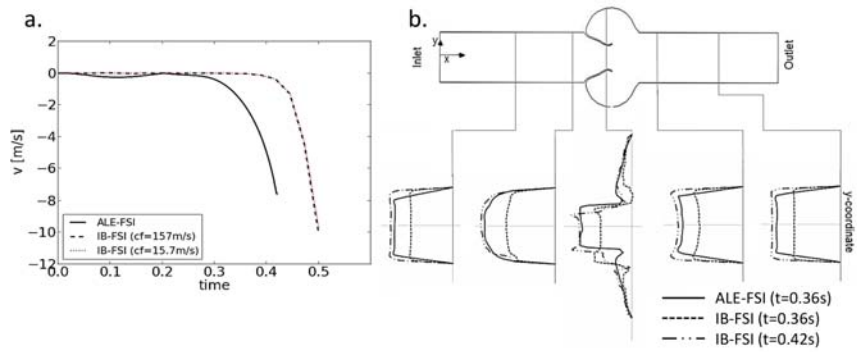

Figure 4.6: (a) Comparison of the displacement of the nodulus of Arantio in the ALE-FSI case (solid line) and in two IB-FSI simulations, obtained with $c_f = 157m/s$ (dotted black line) and $c_f = 15.7m/s$ (dotted red line). (b) Velocity profiles in different sections.

4.3.2 3D simulations

The initial configuration for the 3D model was assumed to be the closed position, being the prosthetic valve in this configuration during the scanning. The major issue encountered in this comparative work was related to the difficulties in simulating the opening of the 3D valve in the ALE-FSI case. The fluid grid underwent severe deformation in a limited amount of time. Significant remeshing and smoothing

algorithms to preserve a good quality grid for the fluid domain was not sufficient to ensure the convergence of the problem. The ALE-FSI failed at the early opening phase ($t = 0.024s$) because of the generation of negative volume cells. One leaflet and the negative cell at this time-point are reported in Fig. 4.7.

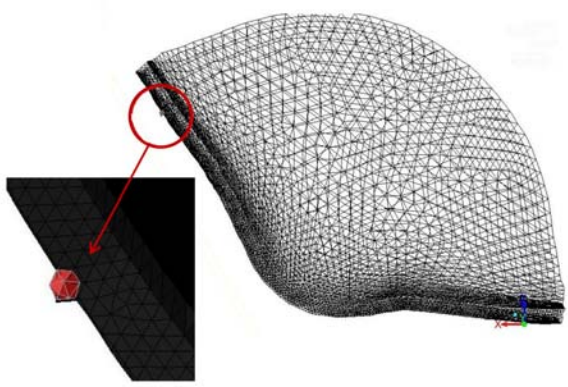

Figure 4.7: Mesh of one of the valvular leaflet at the occurrence of the inverted element (circle). Zoom: negative volume cells.

In Fig. 4.8(a), the maximum open configuration achievable with the ALE-FSI is reported. On the contrary, the valve in the IB-FSI reached the fully open configuration. Due to the limited availability of the ALE-FSI results, the comparison between the two methods was reduced to the early systolic phase. In Fig. 4.8 the results are shown for time $t = 0.024s$ (Panels d, e, g, h, j, k, m and n), and for time $t = 0.07s$ (panels c, f, i, l and o), time point in which the IB valve was in the same configuration as the ALE-based valve. At $t = 0.024s$ the ALE-based simulation (Fig. 4.8) showed higher velocities as compared to the Fig. 4.8(c) (same time-point in the IB-FSI). Also, the deformation of the valve leaflets was different: the valve in Fig. 4.8a and d has the classic bulged shape of the leaflets protruding into the aortic region during the opening phase, while in Fig. 4.8b and e the valve is almost in the initial position. To have a similar open configuration in the IB-FSI in terms of valve position and velocity field it was necessary to wait until $t = 0.07s$, thus the delay that the IB-FSI has in comparison to the ALE-FSI was detected also in the 3D set-up. In Fig. 4.8(e) a layer of higher velocities is detected in the proximity of the walls, as in Fig. 4.6 b. This phenomenon was detected in all the time-points of the IB-FSI simulations and is related to a visualization

issue of the software (it should not have any influence on the results) [48]. At this stage of the cardiac cycle, no blood recirculation in the Valsalva sinuses area was detected, as the leaflets were still in the opening phase. The recirculation zone formation was present in a later phase of the systole, when the AV started the closure phase. As this effect was only visible in the IB-FSI, the results are not reported here. The considerations about the pressure distribution of Fig. 4.8 (panels from j to l) are similar to those for the velocities in Fig. 4.8, panels d-f. At time $t = 0.024s$ (Fig. 4.8(d), (g) and (j)) the difference in the pressure distribution in the two simulation types is evident. It is also possible to notice the presence of a thin layer of low pressure in the neighbourhood of the walls (leaflets and aortic root) in the IB-FSI, which is not visible in the ALE-FSI result. Furthermore, some variations of the pressure are visible in the area downstream the valve in the IB-FSI. In Fig. 4.8 panels m-o, the comparison of the shear stress component $\sigma_{1,2}$ is proposed for the two models. In the zone between the leaflets, an area with higher $\sigma_{1,2}$ values was detected in the two set-ups, related to the higher velocity of the fluid. On the aortic side of the leaflets a small area with higher $\sigma_{1,2}$ values was detected, due to the velocity of the opening leaflets. The presence of localized values of $\sigma_{1,2}$ at the aortic walls in the IB-FSI is related to the presence of visualization artefacts [48].

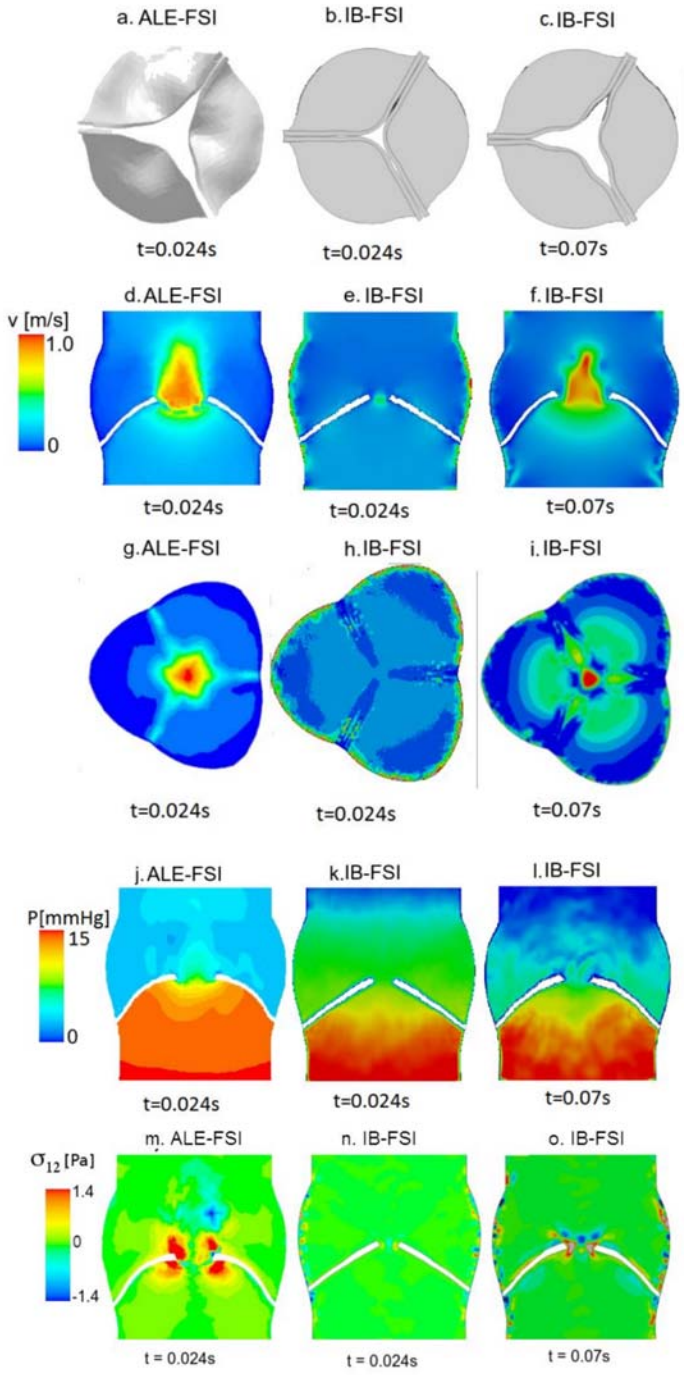

Figure 4.8: (a) Maximum open configuration achieved with the ALE technique at $t = 0.024s$. (b) IB-FSI valve at $t = 0.024s$. (c) IB-FSI valve at $t = 0.07s$. (d-f) Velocity profile on a longitudinal section. (g-i) Velocity profile on the cross section, (j-l) pressure distribution on a section. (m-o) Shear stress $\sigma_{1,2}$ on a section.

Comparing the rapid valve opening time (RVOT) of the IB-FSI ($200ms$) with literature data (reported range 45 to $65ms$, both from structural [76] [77] [78] and from FSI [52] [53] [54] simulations), the time delay previously described in the 2D comparison was even more pronounced in the 3D case. To verify the source of delay, a pure structural simulation was performed on the same geometry. The model was consistent with the IB-FSI simulations in terms of geometry, mesh, material and element type. In the structural case the loading pressure curves were directly applied on the leaflets surface, while in the FSI case are applied at the inlet and outlet of the fluid domain. In Fig. 4.9(left panel), the displacement of the Nodulus of Arantio is reported for the IB-FSI and the structural simulation. The obtained RVOT in this case was about $80ms$, significantly closer to the expected value but remaining outside the physiological range for this parameter. For the sake of completeness, in Fig. 4.9 (right panel) we report the displacement of the valve during systole (up to the beginning of diastole) obtained with the IB-FSI [79]. The flow field results are omitted for conciseness reasons.

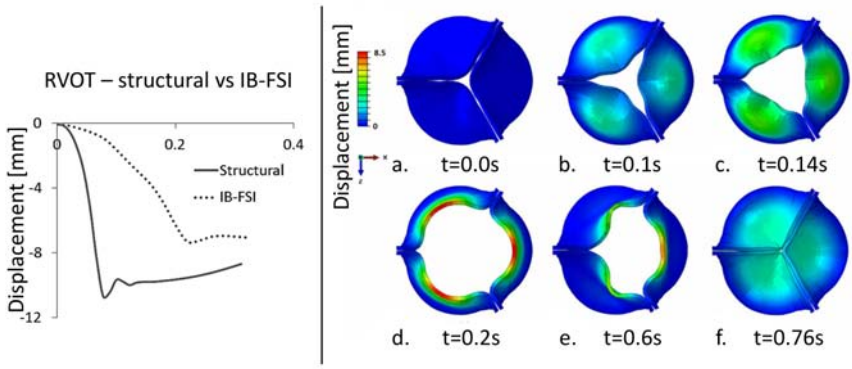

Figure 4.9: Left panel: displacement of the nodulus of Arantio, comparison between an IB-FSI and a structural simulation. Right panel: kinematic of the leaflets in significant time-points of the heart cycle until diastole (IB-FSI). The colour scale indicates the magnitude of the displacement calculated from the initial configuration.

Focussing on the leaflet kinematics resulting from the IB-FSI simulations, the opening phase lasted from $t = 0s$ to $t = 0.2s$ Fig. 4.9 (a-d), with the typical orifice shape that was detected in the AV opening. At $t = 0.2s$ the valve was in its fully open configuration Fig. 4.9 (d). As shown in Fig. 4.9 (e), when the ΔP across the valve

reversed, the leaflets movement ceased to be symmetric ($t = 0.6s$). This was also verified by following the displacements of the central part of the aortic leaflet (nodulus of Arantio). At $t = 0.76s$ the valve was in the fully closed position, with the contact enforced in the coaptation zone Fig. 4.9 f. A residual central opening was visible. To investigate the unexpected asymmetric motion of the valve, a separate test on the diastolic phase was performed, where the valve was kept in the closed position and the pressure on the aortic side was gradually raised from the reference pressure to a value of $120mmHg$, while the ventricular pressure was kept at the reference pressure. By analysing the definition and the evolution of the VOF in this set-up, a loss of void (Eulerian cells in which no fluid is defined, in white in Fig. 4.10 was detected on the ventricular side of the valve. In Fig. 4.10, this phenomenon is illustrated in more details in Fig. 4.10a the initial definition of the VOF is shown. By increasing the transvalvular pressure (Fig. 4.10, panels b and c), the empty cells propagate in the ventricular portion of the fluid domain.

Figure 4.10: Loss of the definition of the VOF in the domain in case of high and reversed ΔP across the valve. In black the cells filled with fluid, in white the cells filled with void.

4.3.3 Computing time

All the IB-FSI simulations were performed on a cluster (3.4 GHz and 5.6GB of RAM), in parallel on 8 CPUs. All the ALE-FSI were performed on 8 CPUs of a Dell PowerEdge R620 server (2x Intel Xeon E5-2680v2 CPUs at 2.8 GHz). There was a clear advantage in using the IB method in terms of computing time. Despite the use of a much larger computational grid for the Eulerian case (Table 4.1), the simulation resulted to be much faster than the ALE case, as there was no need of remeshing and no issues related to a highly deformed mesh. While the coupling algorithm showed good performance in vascular applications, it might require further adjustment to treat the interaction of complex 3D, thin and highly flexible structures completely immersed in the fluid domain. In Table 4.2 the required time is reported for each case.

Table 4.2: Computational time required by the two techniques. In the 3D case, for the ALE the time of the partial simulation is reported, while for the IB-FSI the time for the complete simulation is listed.

2D		3D	
ALE-FSI	IB-FSI	ALE-FSI	IB-FSI
48h	1h	11d (early opening)	30h (entire systole)

4.4 Discussion

4.4.1 2D simulation results

In the 2D case, the comparison of the two models provided similar results, despite the presence of some time delay in the IB-FSI case. The kinematics of the valve was comparable to the literature data [60] [64][80] and the discretization technique does not introduce significant differences between the ALE and the IB case. Also, the ALE fluid solver is capable to automatically manage the smoothing and the remeshing of the computational mesh. A simplified but similar comparison can be found in [55], showing an analogous behaviour of a 2D flexible slab moving in a fluid domain with the ALE or the Eulerian approach. Even though the time required for the IB-FSI (1 hr) was lower than for the ALE-FSI (48 hrs), to our experience the latter was still considered to be in a reasonable range for an FSI simulation. Due to the simplified model and its 2D nature, it was not possible to simulate the diastolic phase: the two thin structures of the leaflets could not bear the high pressure difference imposed across the valve, and even with the imposition of the contact constraints they reversed into the ventricle. The same behaviour was detected in both the IB- and ALE-FSI simulations during diastole. A similar behaviour is described in [55] for a very flexible beam immersed in a pulsatile flow, even in presence of contact conditions. To further verify that this inability to simulate the diastolic phase was not related to the FSI technique as such or the way the contact between structures was defined, a pure structural 2D simulation was performed in Abaqus/Standard in which the geometry, element type, material properties and the contact properties were consistent with the FSI simulations. A transvalvular pressure difference was imposed between both sides of the leaflets. Two different cases were tested to check the potential impact of the definition of the contact properties: in the first case a gap between the leaflets was allowed (as done in the ALE-FSI), in the second case no gap was kept and the valve could completely

close. In all the tested cases the structure reversed in the ventricular side of the tube during diastole. Therefore, we could conclude that the buckling of the structure was mainly related to the two dimensionality of the problems, and not on the fluid grid discretization or the contact function used. We hypothesize that this phenomenon was no shortcoming of the numerical codes, but rather due to the fact that a closed valve in the 2D configuration was physically not possible under the assumed boundary conditions and leaflet properties, which would lead to valve prolapse [55].

4.4.2 3D simulation results

Even though in theory the ALE-FSI would be preferable to simulate the fluid-mechanics of AV [59] [61], in our experience this approach was significantly limited by the large deformations of the fluid grid, which were the cause of the failure of the simulation. The mesh motion algorithms (Fig. 2.2) tested were the spring-based model and the diffusion model. The required parameters for the two algorithms were chosen according to the characteristic dimensions of the fluid mesh. Several tests were performed to increase the mesh density and decrease the time-step size to avoid the excessive deformation of the mesh, leading to cells with negative volume. As the chosen grid was unstructured and the motion was complex and not known a priori but defined by the interaction of the two domains, it was not possible to calculate the displacement of the structure prior the calculation and adjust the time-step size and dimensions of the fluid grid accordingly [81]. Different initial configurations for the valve have been tested, starting from a slightly open position to a fully open position, but the appearance of negative volume cells arose any time the large displacement of the valve occurred. The simulation with a different coupling algorithm (interface artificial compressibility (IAC)) was also carried out (more details in chapter 5). Besides these aspects, the required computational time for the (partial) ALE-FSI is considered to be excessive compared to the performances. We can therefore conclude that the IB approach is preferred over the ALE approach, at least to study the valuvalr kinematics with the tested fluid mesh motion algorithms in the case of large deformations of thin structures.

With the approach chosen and reported here, it was not possible to generate a complete and reliable ALE-FSI simulation. Alternative solutions to alleviate this problem can be, among others: (1) the use of alternative available smoothing algorithms, for example the solid elastic based smoothing algorithm, (2) the motion of the internal

points of the fluid domain could be controlled by the user, with an approach similar to the method described for example in Schenkel et al., [29] for the moving ventricles (see paragraph 6.3.1 for more details). However, there is no guarantee that these approaches will eliminate the problem of negative cell volumes.

4.4.3 Solver choice

The choice of the solver has an important impact on the outcomes of the model. According to our experience, a solver as Abaqus/Explicit (release 12.0), primarily made to solve pure structural problems, it is not the most appropriate choice in case of IB-FSI simulations for heart valves. In particular, the definition of the VOF in the IB-FSI problem resulted to be the bottleneck of this type of simulation. The material boundary reconstruction performed by Abaqus in the Eulerian elements where the value of the VOF is between 0 and 1 is simplified to a planar facet, resulting in less accurate interface definition in case of complex boundary or large Eulerian elements. To have an adequate definition of the VOF, the size of one fluid element had to be smaller than one third of the structural element [48]. Due to the high complexity of the motion of the structure, the refinement of the fluid mesh had to be done in the three dimensions and extended to the entire region where the valve is expected to be, which is why the Eulerian fluid mesh resulted to be one order of magnitude larger than the ALE-mesh (Table 4.1). By increasing the cells density of the Eulerian mesh, the results showed an improvement, but some of the issues remained, e.g. the loss of void when the pressure drop across the valve reversed. In our opinion, the loss of void could be referred to the VOF definition, which in our case seemed to be not yet satisfactory. This phenomenon had no physiological meaning, therefore the analysis of the results was limited to the opening phase of the valve. In the current study it was not possible to obtain an even more refined fluid grid: the element size would have been too small and the solver would have no longer been able to distinguish two neighbouring nodes. As the valve is a thin and highly flexible structure, shell elements might be a more suitable choice for the model and could remove some constraints on the requirements for the fluid mesh, allowing for larger fluid elements. A separate investigation showed that this type of elements is probably not optimized for fluid-structure contact yet in Abaqus/CEL version 12.0, and therefore the simulation degenerated with distorted elements [79]. The choice of using continuum elements was one of the limiting factors of this work: their small size influenced the dimensions of the fluid domain cells,

leading to the above-mentioned problems related to the VOF. For the same reason, only one layer of cells was present in the thickness of the leaflets: thus a numerical stiffness was introduced in the leaflets, especially regarding the bending modes of the structure. The use of hourglass controls and mass scaling factors did not improve the overall performance of the simulation. The use of quadratic elements is currently not available in Abaqus/Explicit 12.0 [48]. One of the possible alternatives to solve the problems related to the IB-FSI formulation and overcome the correct definition of the VOF would be to allow a partial adaptation of the fluid mesh in the vicinity of the moving walls [59] [54] [55] [39], to guarantee a finer mesh which can follow the movement of the structures and allow a coarser mesh in the remaining of the flow domain. However, this option is not available in a black-box solver such as Abaqus.

4.4.4 Compressibility factor

In the IB-FSI, the equations that are solved for the Eulerian elements are initially written for highly deformable and plastic materials: the fluid-structure interaction is therefore an extreme case in this category, where the plastic material is a fluid. This introduces convergence issues in the IB-FSI model, which were solved with the introduction of a small compressibility of the blood commonly adopted [52] [53] [54] to enhance the convergence of the FSI simulations. In physiology, the speed of sound in the blood c_f is estimated to be $1570m/s$ [72], in our 2D case the amount of compressibility introduced resulted in a $c_f = 157m/s$, which was comparable to the values reported in literature [52] [53] [57]. This was not the case for the 3D setting, where the chosen value for the compressibility of the blood is higher than the values reported in literature ($c_f = 15.7m/svsc_f = 157m/s$). Due to the complexity of the 3D case, the choice of the element type and the requirements for the fluid mesh, the choice of higher values of c_f would lead to instabilities of the simulation. Since reducing of the speed of sound to such a low value could affect the reliability of the results, additional investigations were conducted to verify the validity of our choices. In a set of separate preliminary tests on the 2D set-up, the displacement of the leaflet was monitored to investigate the influence of the augmented compressibility, by performing the same FSI simulation with the two chosen different values for c_f. The results were comparable, both in terms of displacement and opening time, suggesting the independence of the results from the chosen compressibility factor [79], as shown in Fig 4.6a. The Mach numbers obtained in all the presented simulations were within the range of 0.006

to 0.06, falling in the range of incompressible flow. By comparing the obtained Mach number with the results available (where the compressibility was included), the results showed a good agreement [53] [60] [75] [72]. To further verify the influence of the compressibility factor in the case of interest, a separate test of numerical experiments is reported in chapter 5. The mass flow balance of the simulations was verified, the imbalance between inlet and outlet was below 1% of the outlet flow throughout the duration of the simulation for the worst case of $c_f = 15.7m/s$.

4.4.5 Time delay

In both the 2D and 3D simulations, the IB-FSI showed a time delay in the valve kinematics, when compared to the ALE-FSI in the 2D case, or to literature data in the 3D set-up. In the 3D case this delay was significant: the calculated RVOT was about 200ms, against an average of 55 ms of RVOT from previous FSI studies in the literature [52] [53] [76] [77] [78]. In vitro studies conducted on a similar type of valve on a pulsatile artificial circulation system report a RVOT for a Carpentier Edwards Perimount Magna valve of 48±10ms [82] [83]. The comparison of the opening time of the aortic valve with in vivo reports is more challenging, as the boundary and working conditions are not easily comparable. Typically, the ultrasound recordings are performed in the case of (stenotic) pathologies. Nevertheless, values of 57.5±11.1 ms [53] [84] are reported. All available data thus seem to indicate that the opening time of about 200 ms, resulting for our 3D IB-FSI simulations, is an overestimation, although it is to be stressed that the only conclusive experiment would be a one-on-one comparison between experimental observations and numerical simulations using an identical set-up (valve and cardio-vascular geometry, liquid properties, ...) and boundary conditions.

Several tests were performed to verify the origin of the delay: despite the artificial compressibility factor was shown to be not relevant for the IB, it might still have a residual effect when dealing with complex highly dynamic events such as the valve motion [79]. The choice of the elements type also played an important role: due to the impossibility of using shell elements in Abaqus/CEL, it was necessary to use solid continuum elements for the solid domain of the 3D case. Furthermore, only one layer of elements was allowed in the thickness of the leaflets, due to the fluid discretization requirements (as explained in the previous section). To verify the assumption on the number of elements in the thickness of the valve, two additional structural (CSM) simulations were performed. Again, the geometry, element

type, material and contact properties were consistent with the IB-FSI set-up. In the first case, a valve with one layer of elements in the thickness was realized, while in the second test two layers of elements were applied in the thickness. The first simulation resulted in a RVOT of 80ms, the second in a RVOT of 40ms. The value obtained for the two-layers-element thickness valve fell within the expected range of RVOT values (40-65ms) [52] [53] [76] [77] [78], while in the other case a longer RVOT was obtained. The use of one layer of elements in the thickness, therefore, introduced numerical stiffness in the valve, compared to the geometry with two layers of elements across the thickness. This tests confirmed that the use of one layer of elements in the thickness of the valve introduced a portion of delay in the valve kinematics. However, the global delay measured in the IB-FSI simulation was more significant than the delay due to the choice of the elements. Therefore, the element choice could not fully explain the origin of the significant time delay in the IB-FSI. To isolate the origin of the time delay, the effect of the fluid-structure interaction contact algorithm was investigated and the results are reported in chapter 5. Tests showed that the use of the contact algorithm to enforce the FSI conditions at the interface in the tested release of Abaqus/CEL 12.0 introduced a time delay in the flow velocity curve comparable to the delay obtained in the IB-FSI case.

4.5 Conclusion

In this chapter we performed a critical comparison between two FSI simulation techniques for a heart valve with flexible leaflets. Several papers are available in the literature reporting results for the IB-FSI simulations, proving that the technique is suitable (within its intrinsic limitations) to model fluid-structure interaction scenarios where large displacements are involved [56] [59] [51] [52] [53] [54] [36] [57] [69]. Over the past few years, particular attention has been focused on improving the computational technique, to obtain a more robust and reliable formulation [6, 12, 13]. To the best of our knowledge, this is the first study systematically comparing the performance of ALE and IB methods for solving the FSI problem of an aortic valve and reporting in detail the pros and cons of both methods for this specific case. In our experience, due to the deformation of the fluid mesh in the ALE formulation in case of large displacements, the simulation of a heart valve with a fluid-structure approach seems to be infeasible using the selected mesh motion techniques and the described approach. However, a 3D ALE-FSI simulation has been presented in a recent

work of Cao et al., 2015 [61]. The FSI simulation of a simplified aortic valve is performed within the commercial suite of ANSYS, which provides the structural and the fluid solvers and the coupling algorithm. From the modelling point of view, the leaflet's material is considered to be non-linear and the structure is discretized with second order tetrahedral elements. A second order time discretization scheme is used.

The IB-FSI provided a solution to the problem for the opening phase, and offers a significant advantage in terms of computational cost, even though the number of elements is much higher in the 3D IB-FSI, compared to the corresponding ALE-FSI. We nonetheless observed a significant time delay in the leaflets motion with the presented IB-FSI simulations and a "loss of void" in the vicinity of the leaflets. In depth analysis led us to conclude that these limitations are related to the solver used (in its particular release version), rather than being intrinsically due to the immersed boundary technique. As such, caution is warranted in extrapolating our observations and conclusions to other numerical solvers and/or software versions and other fluid-structure interaction problems.

Chapter 5

Analysis of compressibility and other possible sources of suboptimal results in FSI simulations

5.1 Introduction

As described in chapter 4, a certain amount of compressibility had to be included in the IB-FSI cases to guarantee the stability of the explicit solver and to reduce the computational time. However, the required amount of compressibility was significant, especially for the 3D scenario (two orders of magnitude in the speed of sound in the fluid). To verify that the addition of large quantities of artificial compressibility does not affect the results of the simulations, additional tests were performed. In paragraph 5.2 the principles underlying the introduction of artificial compressibility in Abaqus/CEL simulations are explained, and the performed tests and results are discussed in details. Concluding, an additional paragraph on the time-delay detected in all the IB-FSI simulations (see previous chapter) is provided.

In ALE-FSI HV simulations, the major encountered difficulty was related to the low quality of the deformed fluid mesh which did not allow to reach a solution for the problem. In this case, the introduction of the artificial compressibility was used to be able

to lower the time-step size used and (in theory) proceed with the simulation [43]. Furthermore, the IAC technique temporarily (see chapter 5.3) mitigates the hypothesis of the fluid incompressibility, which could negatively influence the convergence of the solution. In paragraph 5.3 the principles of the IAC method for partitioned FSI simulations are provided, the results obtained with the technique are provided and the conclusions are discussed.

5.2 Compressibility for the IB-FSI simulations

5.2.1 Working principles

The stability of an explicit solver such as Abaqus/CEL for FSI simulations is secured by artificially introducing a limited amount of compressibility in the simulation, even though the blood is assumed to be an incompressible fluid [53][57][72][75]. The compressibility of a fluid can be introduced by modifying its bulk modulus K_b or the speed of sound in the fluid c_f. The two quantities are related via the density of the fluid ρ by the equation:

$$c_f = \sqrt{\frac{K_b}{\rho}} \tag{5.1}$$

The estimated physiological bulk modulus for blood is between 1 and 2.6 GPa [72], resulting in a c_f of $1570m/s$, assuming a $K_b = 2.6GPa$ and the physiological density of the blood $\rho = 1060kg/m^3$. In previously documented literature works reporting on FSI simulations of cardiac valves the value of K_b had been lowered to 1% of its physiological value [53] [54] [57] [72], to increase the allowed time-step size, reduce the computational time and increase the stability of the simulation. This value of K_b results in a speed of sound in the blood of $157m/s$. In the following, we will refer to the compressibility introduced in our simulations by means of speed of sound in the blood, keeping the physiological value ($c_f = 1570m/s$) and the value reported in literature ($c_f = 157m/s$) as references. As discussed in chapter 4, the 2D simulations were performed with a $c_f = 157m/s$, coherently with the value previously used in literature. The need of a lower value for the speed of sound ($c_f = 15.7m/s$) arose from the 3D test case, as it was not possible to perform the simulation with the higher value (instabilities). This choice was verified with several tests, to ensure that the low value of c_f was not affecting the reliability of the overall FSI simulation. As no reports on a similar

case were found for the solver Abaqus/CEL, further investigations on a simplified 2D case are reported, to ensure that, at least in the cases where the analytical solution is available, the solver provides reliable results.

5.2.2 Simplified 2D case: tests, results and discussion

To isolate the influence of each term of the Navier-Stokes equations and relate each term with the influence of the compressibility factor, additional simplified tests were perfomed. A 2D rigid and straight tube was used for the test cases, to be able to compare the results with the analytical solution. The dimensions and the location of the inlet and outlet surfaces were consistent with the 2D set-up described in chapter 4 and Fig. 4.3 (L = 130 mm, D = 20 mm). The boundary conditions were chosen depending on the type of test performed.

To study the effect of the inertial terms of the Navier-Stokes equations, the fluid was considered inviscid, a sinusoidal pressure curve at the inlet and a constant pressure at the outlet (equal to the mean pressure value of the sinusoidal pressure at the inlet) were imposed. By doing so, if the fluid is incompressible, the Navier-Stoke equation of the momentum (eq. 2.3) can be reduced to:

$$\frac{\partial v}{\partial t} = -\frac{\partial p}{\partial x} \tag{5.2}$$

Where the velocity as a function of time $\frac{\partial v}{\partial t}$ depends only on the pressure distribution $-\frac{\partial p}{\partial x}$. More in detail, the imposed pressure curve (solid line) and the expected velocity curve (dotted line) are reported in Fig. 5.1. In this case, the expected velocity can be calculated analytically. The parameters selected for the generation of the sinusoidal input were consistent with the simulated aortic region, with a period of 0.8s and a mean pressure of 100 mmHg. This resulted in a peak velocity of about 1 m/s for the 2D case under analysis. The speed of sound in the blood used in the test cases were $c_f = 157m/s$ and $c_f = 15.7m/s$, resulting in a Mach number of $Ma = 3.6 \cdot 10^{-3}$ and $Ma = 3.6 \cdot 10^{-2}$, coherent with the Mach numbers obtained from the IB-FSI simulations performed in the 2D and 3D cases discussed in chapter 4.
The use of an initial step in Abaqus/CEL was fundamental. The results shown in the following were obtained after ramping the pressures of the IB simulation from a zero level to the mean pressure value, as also explained in chapter 4.

The analysis of the phase shift of the signals in the tested case provided additional insights on the simulated set-up (Fig. 5.1, left panels). In the worst case scenario, with a mean pressure of 100 mmHg and a $c_f = 15.7m/s$, the velocity curves at the inlet and outlet of the domain were coincident, as shown in fig. 5.1b. Therefore, the wavelength of the signal in this case was still much longer than the domain of the simulation and the compressibility has no significant effect ($\lambda/L >> 1$). The comparison between the expected analytical solution and the curves obtained with different values of c_f is shown in Fig. 5.1c. In this case, the phase shift between the analytical solution and the calculated solution was also negligible, with a maximum difference of 1.1% between the calculated curve and the analytical curve. By lowering the c_f even further, a mismatch in the amplitude of the curve was detected. In dotted line, the curve obtained with $c_f = 8m/s$ is reported, the Mach number in this case was about 0.09. As the first ten harmonics of the fundamental frequency have an influence on the arterial waveform [85], we tested the influence of the compressibility using the 5th, the 10th and the 20th harmonic as an inlet pressure profile. All the simulations were performed with a $c_f = 15.7m/s$. The maximum error (defined as $\frac{v^{max}_{analytic} - v^{max}_{calculated}}{v^{max}_{analytic}} \cdot 100$) obtained for the 5th, the 10th and the 20th harmonic were respectively 5.9%, 9.4% and 19.4%. Despite the presence of 5.9% maximum error, the calculated 5th harmonic had no significant phase shift between inlet and outlet, and between these and the analytical solution. When going to higher harmonics, the shape of the calculated waves changed compared to the expected curve. In Fig. 5.1d-f the graphs of the inlet and outlet velocity of the 5th, 10th and 20th harmonic are reported. Note that the time scale and velocity scale differ for each graph.

While the contribution of the 20th harmonic on the cardiac pressure wave can be neglected, the 10th harmonic could still have some influence on the results. In the worst case of $c_f = 15.7m/s$, having an inlet signal with a frequency of $f = 12.5Hz$ led to a maximum error of almost 10% and a waveform of the calculated velocity slightly different from the expected curve.
In conclusion, for an inviscid fluid and for a pure sinusoidal inlet signal, the changes of the speed of sound in the blood did not affect the results for the range of values discussed in the paper (Fig. 5.1, left panels). However, using a more complex input signal such as a physiological pressure curve, some residual effects could be still present, due to the higher frequency harmonic components used in the simulations.

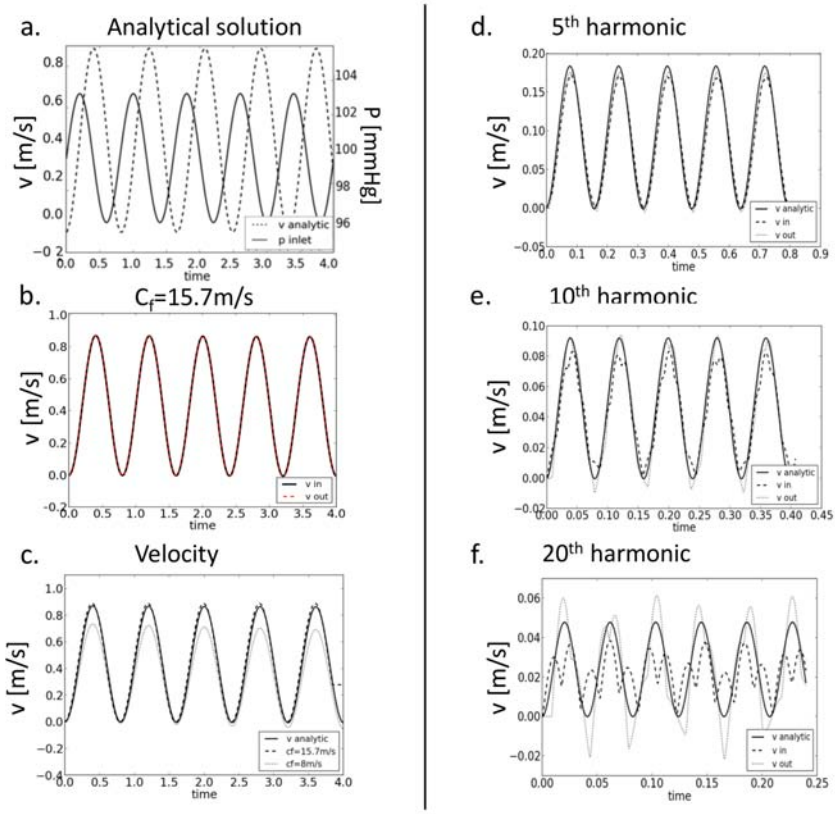

Figure 5.1: Left panel: (a) imposed pressure and analytically calculated solution. (b) Inlet and outlet velocities obtained for $c_f = 15.7m/s$. (c) Comparison between the analytical solution and the results of the simulations with low values of c_f ($c_f = 15.7m/s$ and $c_f = 8m/s$). Right panel: results obtained imposing a sinusoidal pressure curve with the frequency of (d) the 5th, (e) the 10th and (f) the 20th harmonic respectively.

The second case performed was a steady state test, where the Poiseuille solution can be calculated. For a stationary laminar flow of an incompressible viscous fluid, the Navier-Stokes equations can be reduced to:

$$\frac{\partial^2 v_x}{\partial y^2} = -\frac{\Delta P}{L\mu} \tag{5.3}$$

Where v_x is the x-component of the velocity in the channel, ΔP is the pressure drop imposed, L the length of the channel and µ the viscosity of the fluid. A constant pressure difference of 1 mmHg was

applied between the inlet/outlet of the geometry, to evaluate the effects of the viscous term in the equations. With this set of numerical experiments, we wanted to investigate separately the effects of the viscous term of the Navier-Stokes equations solved by Abaqus/CEL. Despite the presence of pressure fluctuations in the tube, the maximum velocity reached in the Abaqus/CEL set-up was 10% smaller than the maximum velocity obtained by Fluent, in a fully developed flow.

5.2.3 Additional considerations over the time delay

Having proven that the use of the compressibility was not the main cause of the time delay shown by the valve in the IB-FSI and having discussed the impact of the element type and number of element layers choice (chapter 4.4.5), further investigations were performed to identify the origin of the time delay. A possible source of error was the contact algorithm used to enforce the interface conditions used in the Abaqus/CEL release 12.0. The interaction between the two domains is enforced via the general contact algorithm, providing no-slip conditions to the fluid and a no-separation constraint for the two domains. To investigate this, a simple tube with rigid walls was simulated. The flow was chosen as viscous ($\mu = 0.0035 Pa \cdot s$), no-slip conditions were imposed at the walls and a sinusoidal inlet pressure curve was imposed, after ramping the pressure at the inlet and outlet to the mean pressure value of 100mmHg, consistent with the procedure used in the IB-FSI simulation of the valve (chapter 4). In the first set-up, the rigid walls were implemented by imposing a velocity constraint on the fluid, no real structural domain was included (therefore the term "no-walls" was used in the results to indicate this type of boundary conditions), resulting in a CFD simulation (Fig. 5.2a). In the second test-case the rigid walls were included in the simulation, the interaction between the fluid and the solid and the no-slip conditions were enforced with the contact algorithm (Fig. 5.2b). The obtained velocity curves are reported in Fig. 5.2c

The results of the simulation with no walls (dotted line) were in agreement with the expected solution. The presence of the fluid-structure interaction introduced some fluctuations in the velocity curve and, most important, a time-shift at the onset of the velocity curve, which then disappeared with the progression of the simulation. The initial delay of the FSI simulation in the test case was t=114ms, comparable to the time-delay obtained in the IB-FSI valve case. As in the IB-FSI simulation of the heart valve it was not possible to simulate multiple cardiac cycles (due to the discussed reasons), this effect could be still present in the results and therefore affect the kinematics of the valve.

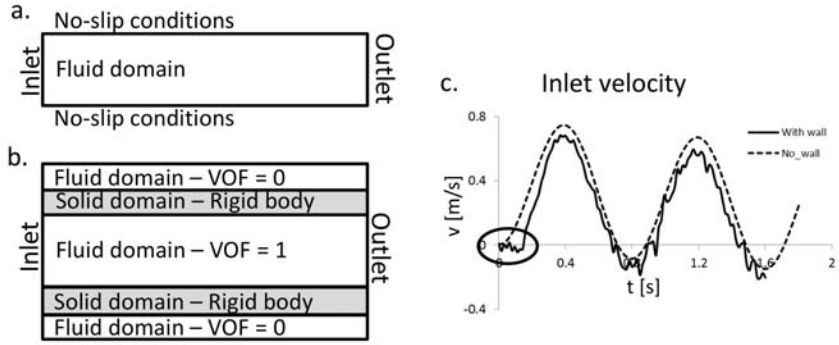

Figure 5.2: (a) First set-up geometry. (b) Second set-up geometry. (c) Inlet velocity profile comparison: with and without walls. The delay is indicated with the circle.

5.2.4 Conclusions

The influence of the compressibility factor was tested in a 2D simplified Abaqus case, in both a steady state and a transient configuration. For the transient simulations, we can conclude that the reduction of the speed of sound did not significantly affect the results of the simulation, as the characteristic wavelength of the set-up was still much longer than the domain. The effects of the harmonics of the signal were also tested, to ensure that their influence was negligible.

The Poiseuille flow test provided good results, with a 10% difference between the Fluent and the Abaqus solution. The viscous terms have a minor impact on the final fluid-dynamics of the set-up compared to the inertial terms. Taking into account the results of the presented simplified test cases, the qualitative considerations over the Mach number and the results obtained from the 2D and 3D simulations, we can conclude that in the case of interest the compressibility did not compromise the overall reliability of the simulation. The inertial terms have been verified up to the 10th harmonic frequency and the steady state simulation provided a solution within an acceptable error range. As a further verification, the kinematics of the 2D valve does not resent of the difference in c_f, as shown in Fig. 4.6a.

In conclusion, the time delay detected in the IB-FSI simulation of the heart valve could be related mainly to two factors: first, the choice of using one layer of elements in the thickness of the valve introduced numerical stiffness to the valve, which resulted in a slightly delayed kinematics. The second and probably main source of delay seemed

to be related with the implementation of the contact algorithm of Abaqus/CEL (release 12.0) for the fluid-structure interaction, which introduced an initial time delay in the flow velocity. In the impossibility of simulating multiple cardiac cycles, the presence of an initial time delay affected the timing of the IB-FSI simulation, resulting in a longer RVOT for the aortic valve.

5.3 Compressibility for the ALE-FSI simulations

5.3.1 Working principles

As reported in chapter 4, with the adopted approach and solvers it was not possible to complete the ALE-FSI simulations on the AV due to the excessive distortion of the fluid domain.
To avoid the occurrence of distorted or inverted elements, it is possible to modify either the grid size or the time-step size. In fact, an inverted-volume element occurs any time a node has a displacement in a direction $\vec{n}$ greater than half of the size of the cell in the same direction $\vec{n}$. Therefore, increasing the cell size or decreasing the time-step should result in a valid mesh. In our case, it was not possible to modify the cell size, in the first place because larger elements would yield to not accurate and not mesh-converged solutions and, second, the mesh is subjected to automatic remeshing, therefore the mesh dimension and quality during the simulation was not known or accurately predictable. Therefore, the time-step size was reduced. However, with quasi-Newton coupling iterations between a thin and flexible structure and a fluid with a similar density, the reduction of the time-step size results in a slower or no convergence of the coupling iterations at the interface [26]. Therefore, in case of FSI simulations on heart valves, decreasing the time-step size does not have a beneficial effect on the convergence of the solution. It is possible speed up the convergence by using an interface compressibility technique which introduces a linearized term to include in the conservation of mass of the NS equation the added mass effect of the problem. For fluid-dynamic problems, the additional term can be interpreted as artificial compressibility of the fluid [43]. The adjective "artificial" is due to the fact that the term is reduced to zero when the convergence of the coupling iterations is reached. If the artificial compressibility term is added only to the cells neighboring the interface Γ_i, the method is referred to as IAC. The IAC method applied to the AV FSI simulations should also temporarily mitigate the fluid incompressibility constraint. In fact, due to the incompressibility hypothesis, a small perturbation of the displacement of the interface results in a global acceleration of

the fluid and therefore a significant pressure gradient in the fluid. As a consequence, larger displacements can be induced in the structure, resulting in the divergence of the coupling iterations. The addition of the source term to the continuity equations wants to mimic the displacement of the structure and reduce the instabilities that might originate in the coupling iterations [43]. To define the amount of compressibility, the deformation of the structure is estimated in the first time-step of the FSI calculation with the structural solver (S). Two different pressure distributions (p_1^a, p_1^b) are applied to Γ_i to calculate the two displacements x_1^a, x_2^b

$$x_1^a = S(p_1^a) \tag{5.4a}$$

$$x_1^b = S(p_1^b) \tag{5.4b}$$

The calculated positions x_1^a, x_1^b from equation 5.4a are transferred to the flow solver, which can compute the volume ΔVol swept by the interface for a displacement from x_1^a to x_2^b, as in Fig. 5.3 (with $\vec{n}_f$ unit normal pointing out of the fluid domain).

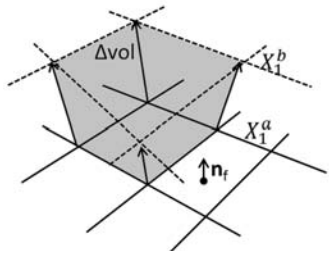

Figure 5.3: Volume swept by the interface for a displacement of Γ_i from x_a^1 to x_b^1 (adapted from [43]).

The artificial compressibility coefficient can be calculated as:

$$c^2 = \frac{p^b - p^a}{\Delta Vol} \cdot \frac{vol}{\rho} \tag{5.5}$$

Where *vol* is the volume of the control volume. The artificial compressibility term can be added to the equation 2.1, for the cells neighboring the fluid-structure interaction interface as:

$$\int_{V_k} \frac{1}{\rho c^2} \cdot \frac{p_{k+1} - p_k}{\Delta t} dV \tag{5.6}$$

Where the index k indicates the coupling iteration number. At convergence, the IAC term disappears as $p_{k+1} = p_k$.

In this work different pressure distribution p^a and p^b of equation 5.4a have been tested (constant or proportional to the cell volume). A uniform compressibility coefficient was also tested.

5.3.2 Methods and results

The 3D model described for the ALE-FSI simulations in chapter 4 has been replicated with the IQN-ILS method and with the IAC method for the coupling iterations. The simulations were started at the beginning of systole after a preconditioning step, the systolic phase was imposed to be 0.2s long and the peak of systole occurred at 0.03s. In table 5.1, the major differences between the two simulations are reported.

The use of the IAC method allowed for the reduction of the time-step size, which was necessary to overcome the generation of negative volume elements in the opening phase of the valve. However, due to the numerical technique which does not require the calculation of the full Jacobians of the solvers, the IQN-ILS coupling algorithm showed a more efficient performance in terms of number of iterations per time-step and duration of each time-step. The reduction of the time-step size and the increased amount of wall clock time required to complete one time-step in the IAC case significantly increased the computational time of the simulation (about 9h for the IQN-ILS versus 11 days for the IAC).

Nevertheless, the introduction of the IAC did not fully solve the problem of the inverted fluid cells: the motion of the walls in the fluid domain could still generate negative volume cells. The further reduction of the time-step lead to non-converged time-steps also for the IAC techinque, therefore the simulation was interrupted.

Table 5.1: Comparison between the IQN-ILS and the IAC methods

	IQN-ILS	IAC
Time-step size	0.1 ms	0.01 ms
Max time reached	0.017s	0.023s
Iterations per time-step (average)	15.6	24.7
Duration 1 time-step (average)	3 min	7 min
Computational time	9h	11d

5.3.3 Conclusions

Regardless of the numerical modifications for the coupling algorithm code, it was not possible to simulate the entire cycle with the ALE-FSI approach. It is significant to note that the average number of iterations per time-step in both the IQN-ILS and the IAC simulations is significantly higher for this heart valve simulation than for vascular FSI applications, where an FSI simulation of a tube with the IAC method requires on average 5 iterations per time-step, with the IQN-ILS method about 7 iterations/time-step [43]. Similarly, the FSI simulation of a carotid bifurcation required about 5.6 iterations with IAC and 8 with IQN-ILS. Furthermore, the IAC technique applied to HV simulations required more coupling iterations than the IQN-ILS to reach convergence. The differences are related to the nature of the analyzed problem. In cardiovascular applications, the fluid domain is enclosed by the structural domain, whose deformations are appreciable but not excessive. In the HV simulation, especially if no elastic aortic wall is considered, the structure is a thin structure completely surrounded by fluid and the two densities (fluid and solid) are (almost) comparable. The high flexibility and the high number of degrees of freedom of the valve result in large displacements/deformations for the structural domain. This results in a slower (if any) convergence of the coupling iterations at the interface for both the techniques. Furthermore, the use of the IAC over the IQN-ILS technique does not increase the speed of the computation, but it allowed for a longer computation before the occurrence of the inverted volumes elements.

Recently, an ALE-FSI study on native AV has been published [61], therefore with adequate modeling choices the ALE technique can be used to study heart valves. In the work of Cao et al.[61], the ALE-FSI module available in the commercial software ANSYS has been used. It uses a partitioned and strongly coupled coupling algorithm between the built-in fluid and structural solver. The algorithm used to solve the coupling iterations is not mentioned. The most evident difference with our approach is the use of a second-order temporal discretization for the fluid solver. In our case, this option was not available, as Fluent 15.0 only allows a first-order temporal discretization for problems with moving mesh. The second difference is the use of a non-linear material model for the valvular leaflets. The time-step size used in [61] is of 0.5ms, therefore larger than the time-step size used in both the IQN-ILS and the IAC simulations proposed here. The use of a linear material instead of a fiber-reinforced or bilinear material [71] could influence the results of the simulations. From the numerical point of

view, the second-order time discretization scheme is more accurate than the first-order we used.

To summarize, among the limiting factors for our ALE-FSI simulations we can enumerate:

1. The high deformation of the fluid grid which resulted in inverted/negative volume elements
2. The impossibility of decreasing the time-step size to improve the mesh motion with the IQN-ILS method
3. Relatively limited advantages in using the IAC technique for the coupling iterations
4. High computational cost for the case (11d for the longest IAC simulation to reach t=0.023s)

III

Intraventricular flow field analysis

Chapters

Chapter 6

Intraventricular flow: visualization techniques and numerical models

6.1 Clinical relevance of intraventricular flows

The human cardiovascular system is thought to be optimized to provide blood to the entire body with minimal energy expenditure of the cardiac muscle. This is visible for example in the in- and outflow into the left ventricle, where the genesis of a vortex in diastole enhances the ventricular filling, reducing the losses due to conversion of the kinetic energy into pressure in this phase [86] [87]. Furthermore, the vortex ameliorates the washout of the LV and facilitates systolic ejection [88]. The occurrence of cardiac diseases may produce intraventricular flow features deviating from what is considered normal and optimal, reducing the cardiac function. Various techniques are available to assess the cardiac function of a patient. The analysis of the structural cardiac components and deformation patterns (e.g. strain imaging) provide fundamental information on the kinematics and contractility of the heart. The analysis of intraventricular flow, on the other hand, may be an even more powerful indicator of abnormal cardiac phenomena, as changes in the blood flow can precede the development of noticeable structural modifications [89]. Therefore, a reliable and quantitative evaluation of cardiac flow may result not

only in a diagnosis of an existing status, but in its prediction, based on an abnormal or sub-optimal cardiac performance [89] [90].

Intraventricular flows can be visualized in vivo with different techniques, ranging from four-dimensional (4D) flow magnetic resonance imaging (MRI), to ultrasound Doppler and particle imaging velocimetry (PIV) among others [87]. In recent years, the use of image-based numerical simulations is providing interesting results and insights in the intraventricular hemodynamics. The combined use of computational simulations and clinical images for research and diagnosis can provide additional information (e.g. quantitative indeces of vortex formation) and is a valuable tool to investigate the relationship between cardiac pathology and the associated abnormal flow pattern [88] [91] [92]. Of particular interest is the vortex structure which dominates the fluid-dynamics of the LV during diastole. This vortex is known to be strictly related to the LV performance and functionality [86][88] [92] [93] [94]. Other hemodynamic indices that have been explored include intraventricular pressure gradients [95] [96]. From a clinical perspective, as heart failure and cardiac dysfunction have an epidemic proportion, especially in the ageing population [97], the assessment of intraventricular filling patterns and hemodynamics can be used to obtain information to better identify subjects at risk for whom a tailored therapy could be required. In the remaining of this section, an introduction on the intraventricular flow is provided, followed by an overview on flow visualization techniques, numerical tools available for intraventricular flow analysis, with a state of the art review on the principal techniques adopted to simulate the ventricular and the valvular motion. In chapter 7, a novel approach to perform CFD simulations with prescribed moving boundaries is described in detail, and the results obtained on a first test-case are reported. The model is fully based on real-time transesophageal ultrasound images. In chapter 8, the model presented in chapter 7 is expanded to three clinical patients, in the first place to test the applicability of the presented model to different cases and in the second place to investigate the altered fluid-dynamics in different pathological conditions.

6.2 Flow visualization techniques

The conventional clinical indexes of cardiac performance mostly provide relevant information for diagnosis only when the symptoms are appreciable, the pathology is at a late stage and morphological changes and remodeling already occurred. It has been hypothesized that visualization and quantification of intraventricular flow might

provide more significant criteria for early diagnosis and therefore early treatment (especially in high-risk subjects), as the flow field immediately reflects the pathology-related changes in the cardiac function as any change in contractility or shape influences the flow field [94] [98]. Valvular pathologies can also have an effect on the direction and magnitude of the flow jet entering the LV. Therefore, flow visualization is an important tool to understand the cardiac patho-physiology and can be used as a predictive index for early diagnosis. There are currently a number of clinical imaging techniques which allow for the direct intraventricular flow visualization. A brief overview based on the work of Sengupta et al.* [87] of the most popular techniques is provided in the following paragraph. For the purposes of this work, the underlying physics is not explained and the reader is referred to more technical papers for details.

- *4D flow cardiac magnetic resonance (CMR) imaging*:
  The blood flow velocities can be measured in any direction and without the use of contrast agent with the CMR phase-contrast technique. Thanks to the use of bipolar gradients, the signal of the moving blood is in a phase proportional to its velocity. To obtain high quality results, the information of several heart beats is combined prospectively or retrospectively using electrocardiography (ECG) and respiratory gating. This technique results in a three-dimensional and three-directional velocity field measured over a control volume covering the complete heart or large vessels and it is commonly known as 4D flow CMR imaging [87]. The use of 4D flow CRM for flow visualization provides interesting information on the vortical properties and on the transit time of the blood in the LV. The most intuitive visualization of the flow field available from the CMR is the 3D pathlines (Fig. 6.1). The technique is affected by resolution limitations, both in time and in space. It also requires a quite long acquisition time and the data obtained are phase-averaged over several cardiac cycles, such that it is not possible to detect small-scale instability phenomena and beat-to-beat variations.

- *Color doppler echocardiography and flow visualization*:
  The color doppler echocardiography has been used over the last 30 years to qualitatively investigate the flow direction and

*P. P. Sengupta, G. Pedrizzetti, P. J. Kilner, A. Kheradvar, T. Ebbers, G. Tonti, A. G. Fraser and J. Narula, 'Emerging trends in CV flow visualization', *JACC: Cardiovascular Imaging*, vol. 5, no. 3, pp. 305–316, 2012

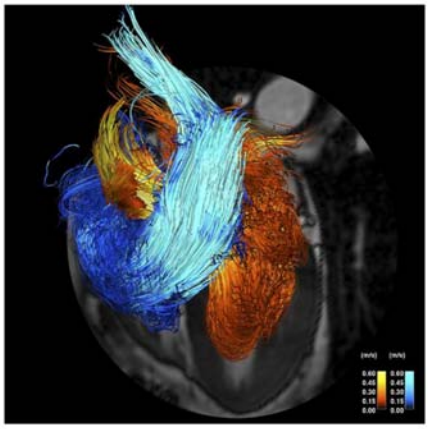

Figure 6.1: CMR pathlines visualization (adapted from [87]).

detect abnormal flow patterns. With color doppler ultrasound, it is possible to measure only axial velocities along the US beam. This technique can be combined with other available measurements to obtain an estimation of the radial velocities and therefore reconstruct a more complete flow field (Fig. 6.2). Among others, the speckle tracking method uses the speckle in the raw ultrasound information retrieved from the blood motion to derive the radial velocity components of the blood. The technique can detect the vortex structures and the main features of the intraventricular flow, but it does not provide details on the small scale velocities.

- *Echo-PIV*:
  A third visualization technique is the echo-PIV. It is the clinical application of the standard PIV, in which the particle velocity is imaged with a laser beam. In cardiology, the particles (i.e. injected contrast micro-bubbles) are imaged with an ultrasound beam which tracks the patterns produced by groups of particles in the region of interest. As a result, the blood flow directions and streamlines are visualized (Fig. 6.3), it is possible to detect the main flow patterns and vortex structures [87]. However, the space resolution of the current echo-PIV acquisition systems is still quite low and the small scale features might not be visualized. Furthermore, the echo-PIV is a 2D technique used to investigate a 3D phenomenon. Currently, the 3D extension based on 3D echocardiographic images is not possible due to

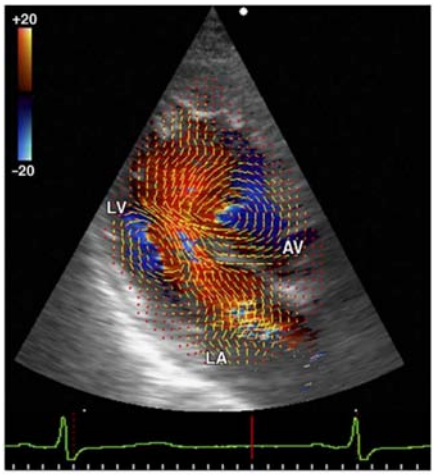

Figure 6.2: Flow velocity vector field (in yellow) superimposed on color Doppler ultrasound (adapted from [87]).

the low time resolution (about 30 frames/cycle), which does not allow for the PIV flow field reconstruction. On the contrary, the multiplanar reconstruction of the 3D flow field is a promising alternative for 3D flow visualization.

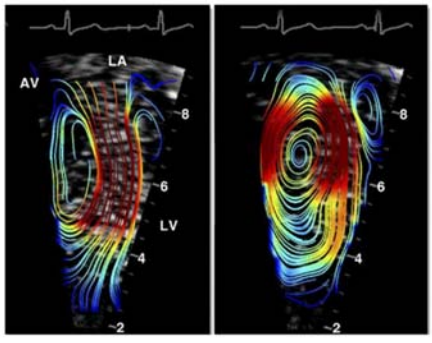

Figure 6.3: Echo-PIV derived streamlines reconstruction (adapted from [87]).

6.2.1 *Excursus* on rt-TEE ultrasound imaging

As the CFD model described in chapter 7 is based on segmented images obtained from real-time transesophageal echocardiographic images (rt-TEE) ultrasound images, a brief *excursus* on the technique is provided. The 3D rt-TEE ultrasound imaging technique allows to

image the cardiac structures during the cardiac cycle and to perform Doppler measurements. The working principles are the same as in regular ultrasounds: very briefly, the ultrasound probe emits high frequency sound waves (ultrasound) which travel through the layers of tissue. Whenever the emitted wave impacts a boundary between layers with different mechanical properties, part of the wave is reflected back to the ultrasound probe and part travels forward in the next layer of tissue until it reaches a new boundary between layers with different properties. The probe records the timing of the reflected wave, such that the position of the impacted boundary can be calculated based on the speed of sound in the tissues and the difference in time between the emitted and the received ultrasound wave. This information is then reconstructed in either a 2D intensity map or a 3D volume.

In regular transthoracic ultrasound imaging, the emitting/receiving probe is located on the outer surface of the chest. Therefore, the ultrasound wave has to travel through the skin, fat, ribs and lungs before reaching the cardiac structure, and the way back before the sensor can detect the reflected wave (Fig. 6.4a).

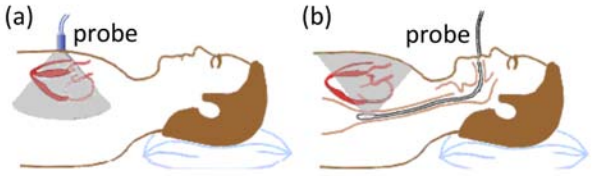

Figure 6.4: Position of the ultrasound probe in (a) transthoracic ultrasound measurements and (b) transesophageal ultrasound images (adapted from [99]).

To have a more accurate ultrasound measurement, the transesophageal ultrasound technique is available: in this case, the probe is inserted in the esophagus of the patient (Fig. 6.4b). The esophagus is a collapsible tube, connecting the upper portion of the digestive system to the stomach. In normal conditions, it is empty and collapsed. During the procedure, the ultrasound probe is introduced through the mouth of the sedated patient until the heart is visualized. The heart is imaged from a much closer position, reducing the distance between the probe and the area of interest to a few millimeters and limiting the layers of tissues between the probe and the heart [100]. In this case, the heart is imaged from the back side, while in transthoracic ultrasounds it is imaged from a frontal view.

The recent advances in ultrasound technology allow for a real-time and three-dimensional acquisition, using specifically designed probes. Analytical software also allow for the off-line reconstruction of 3D models based on the measured data-set, for an improved visualization and quantification of LV and MV functions [101]. The rendering of the 3D LV shown in Fig. 6.5 (a-b) allow for the visualization from multiple perspectives, enhancing the visualization of patient-specific details.

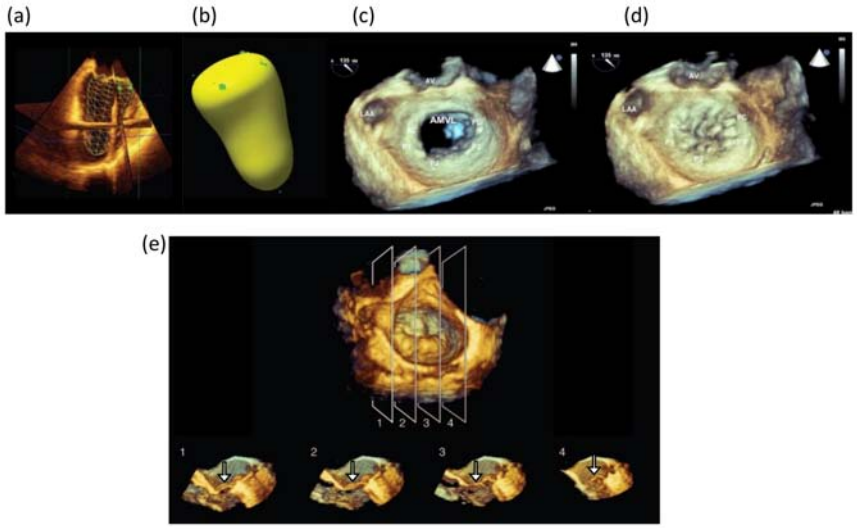

Figure 6.5: (a) Endocardial ventricular cast reconstruction with a wire-frame technique, (b) surface-rendering technique of the LV, which generates a more detailed endocardial surface, (c) mitral valve in the open position, (d) mitral valve in the closed position, (e) mitral valve in the closed position with longitudinal sections (lower panels, valvular leaflet indicated with arrows) (adapted from [101]).

With the rt-TEE ultrasound technique, the level of anatomical details of the valvular structures is significant, as shown in Fig. 6.5 (c-d). The quantification of the leaflet thickness is also possible, as shown in the lower panels of Fig. 6.5e.

6.3 Numerical simulations of intraventricular flow

The use of numerical simulations can be complementary to the clinical analysis for research and diagnostic purposes. In cases where the clinical imaging techniques are too invasive or they provide partial or

inaccurate results, computational simulations of cardiac hemodynamics can fill the gap and provide additional fluid-dynamic information [91]. Simulation-guided surgical planning and therapy could be used to improve the outcome and reduce the burden of the costs of the techniques [91]. Furthermore, the use of computational strategies to optimize the design and the performances of devices (e.g. heart valves, left ventricular assist device (LVAD)) is expanding [102]. Computational simulations can also improve the current outcomes of diagnostic imaging tools. The existing flow visualization techniques are widely used in clinical practice but they still provide limited quantitative information about cardiac function, resulting in a diagnosis based on a small fraction of information. The integration of numerical simulations and visualization techniques could provide additional details about flow patterns and ventricle washout (among others) which would increase the output of the diagnostic techniques [91] [98].

6.3.1 Modelling techniques for deforming ventricles

The hemodynamics in the LV is mainly defined by the motion of the myocardium, which contracts and relaxes pumping blood in and out the cardiac cavities.

In a computational model, the geometry of the LV can be either simplified or derived from clinical images. In simplified models [69] [94] [103] [104] [105], the LV is usually modelled as a truncated ellipsoid (Fig. 6.6 a). For a patient-specific model, the geometry is normally reconstructed from clinical images. High quality imaging modalities ensure a higher level of anatomical details in the geometry reconstruction. In Fig. 6.6 b and c two patient-specific ventricular geometries with a different degree of anatomical details are shown.

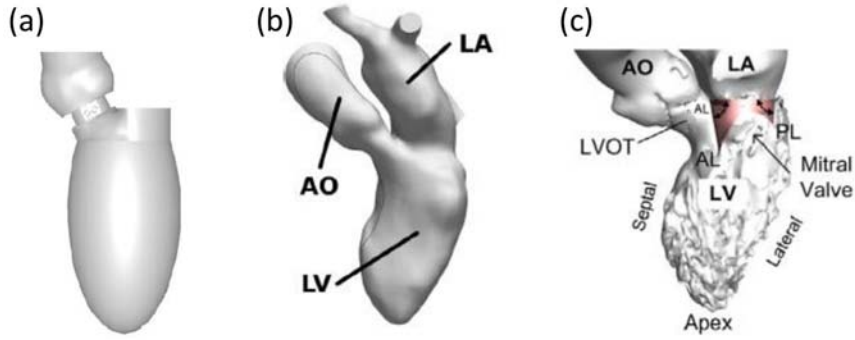

Figure 6.6: (a) Simplified LV(adapted from [81]). (b) LV derived from CT images, without detailed anatomical features (adapted from [106]). (c) LV derived from CT images, with detailed anatomical features (adapted from [91]). Additional abbreviations used in figure: left atrium (LA), aorta (AO)

One of the challenges of simulating intraventricular flows is to reproduce the motion of the LV boundary. Multiple techniques have been explored for this purpose.

In case of simplified LV geometries it is possible to prescribe its kinematics analytically, with a one-parameter model which regulates the dilatation and contraction of the structure [69] [94][103] [104] [105].

For more realistic or patient-specific models, the approach can be based on the segmentation of 4D clinical images (MRI, CT or ultrasound images) to reconstruct a kinematic model of the heart. The displacement of the boundaries is therefore retrieved from the images and transferred to the CFD model, resulting in a prescribed-kinematics model. Commonly, the time resolution of clinical images is too low to enable a numerical simulation, therefore intermediate steps, such as interpolation, are required to generate a CFD-ready model [29] [32] [107]. Additionally, the spatial resolution of the imaging technique is often not sufficient to capture the 3D details of the valvular apparatus during the cardiac cycle, therefore additional assumptions have to be imposed for the valve representation (more details in chapter 6.3.2).

A different approach to generate the motion of the cardiac structures is to implement a multi-physics model, in which an electromechanical and a fluid-dynamic problem are coupled [108] [109] [40]. The motion of the ventricular wall is then generated with an excitation model of the myocardium. The fluid-dynamics of the ventricle

can be calculated with a low-order model [108] or via more complete multi-scale electro-mechanical models which include the orientation of the muscular fibers and solve the hemodynamic problem with the NS equations [109] [40]. On the one hand, such an approach reduces the burden of the limited spatial and temporal resolution of the clinical images and avoids the need of interpolation, but introduces additional unknowns about the mechanical and physical properties of the myocardium. To obtain a reliable multi-physics model, detailed information on the material properties, electrical behaviour, fiber orientation and contractility of the heart are requested, resulting in a costly and time-consuming approach. Examples of fully coupled electro-mechanical problems [102] and one-way coupled problems [109] are reported in literature.

The implementation of a moving ventricle can rely on either the IB method or the ALE method for the mesh discretization (Fig. 2.1). The drawbacks and advantages of the two approaches are similar to those described for the heart valves in chapter 4. In the ALE representation (boundary-conforming techniques), the wall is sharply reproduced and its position exactly known (Fig. 6.7 a). However, the large motion of the ventricular walls can generate distorted elements in the fluid grid, requiring the remeshing of the fluid domain. Previous works on LV hemodynamics relied on the planned remeshing of the fluid domain [29] [32] [107]. Once the deformation of the boundary of the fluid domain is known from images, it is possible to generate a set of conformal grids with a good quality of the elements at predefined time-points. During the simulation, whenever one of the predefined time-points is reached, the computational fluid grid is replaced by the good-quality correspondent mesh. Between two subsequent time-points the mesh is deformed. This results in a user-prescribed remeshing of the domain, to guarantee a good quality of the fluid mesh throughout the entire simulation. However, this technique requires a significant amount of preprocessing operations (generation of the conformal meshes) and it is quite time consuming, as the solution needs to be interpolated from the old to the new grid every time the remeshing occurred. One of the topologically conformal grids of the work of Schenkel et al., [29] is reported in Fig. 6.7 a.

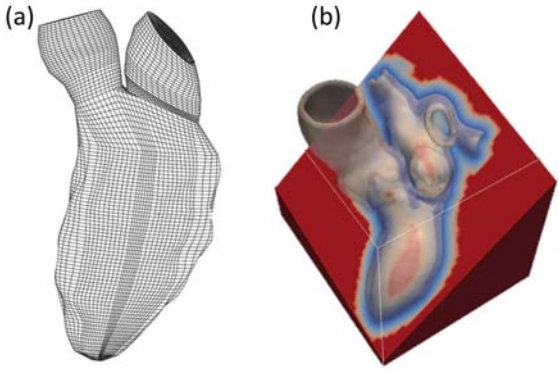

Figure 6.7: (a) One of the topologically conformal grids of the ALE-based CFD simulations (adapted from [29]). (b) Fluid domain of a IB-based simulation. The color scale indicates the level-set function definition for the fluid domain (adapted from [110]).

In the work of Mihalef et al. [110] among others, the simulation is performed with the IB approach (Fig. 6.7 b), where the definition of the fluid domain is based on level-set functions, which define the location of the fluid-solid interface moving on top of a Eulerian grid.

6.3.2 Modelling techniques for a moving mitral valve

The modeling of the mitral valve in a moving ventricle simulation is of great importance to guarantee the reliability of the results [111]. This has been explicitly verified in both simplified 2D [103] and patient-specific [111] models. The mitral leaflets have an important role in the vortex formation and the flow propagation into the LV and the asymmetry of the valve influences the direction of the transmitral blood jet entering the LV, the location of the impact of the flow on the ventricular walls and the 3D orientation of the vortex ring [111]. However, due to its complex and thin structures, its large displacements during the cardiac cycle and the limited availability of high-resolution images, its inclusion in CFD or FSI models is quite challenging. Several techniques have been explored. In the most simplified cases, the valve is omitted, replaced with an on-off orifice [32] [107] [40], which instantaneously opens and closes, synchronous with the LV motion.

In the work of Baccani et al., [103] the mitral orifice is asymmetrically included at the base of a 2D axisymmetric ellipsoid. An additional parameter β (in Fig. 6.8 a, top panel) is defined, to account for the

opening of a virtual and rigid one-leaflet valve. The valvular motion is linearly related to the flow until it reaches the open configuration, as shown in Fig. 6.8 a, lower panel.

In 3D models, a gradual opening orifice can be imposed, to account for the time-varying opening area of the valve [29] [112]. In Fig. 6.8 b, the projection of the mitral valve orifice at four points during the cardiac cycle is shown. The position of the projected orifice is obtained from CMR images and interpolated with spline curves to obtain a smooth opening/closing orifice. With this approach, the gradual opening of the orifice is included, but no information about the 3D orientation of the entering flow jet nor the depth of the vortex formation are provided.

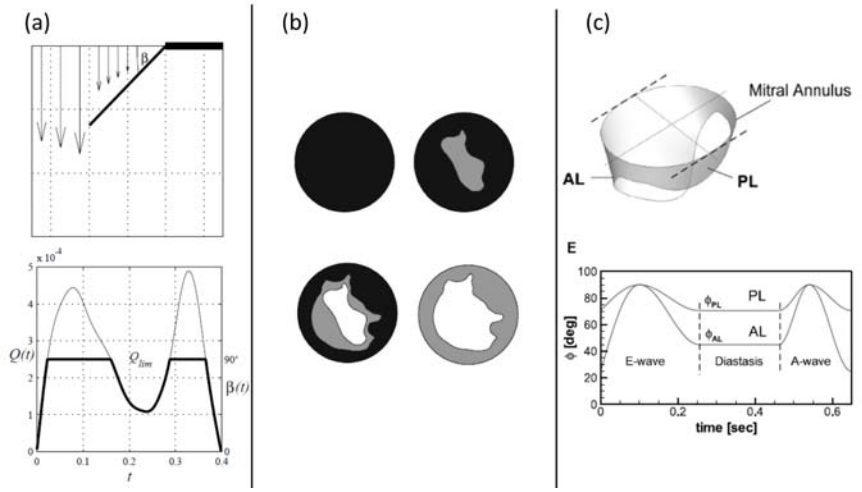

Figure 6.8: (a) 2D model of one-leaflet rigid valve, motion prescribed with the opening angle β, linearly related to the flow (adapted from [103]). (b) gradual opening valvular orifice (adapted from [29]). (c) 3D mitral valve, motion prescribed as a function of the opening angles derived from echocardiographic measurements (adapted from [111]).

In more complex models, a simplified 3D moving valve is introduced. In particular, there are two main approaches: the first is an FSI-based model, while the second relies on the kinematic description of the valve. In the first case, the motion of the valve is calculated with its interaction with the surrounding fluid [113]. However, especially in case of MV modeling, the geometry of the valve and the inclusion of the additional valvular structures such as the chordae and the papillary muscles are extremely complex and cannot easily be

derived from clinical images [91]. Also, the mechanical properties of the valve are not well-known. This results in an FSI valvular model with an elevated number of uncertainties, which makes the use of the FSI approach for MV cumbersome. FSI simulations have been extensively used for aortic valve applications, as the geometry and material properties are relatively easier for computational purposes (e.g. [52] [57]) which have been discussed in chapter 3 and 4.

The second approach is based on the kinematic description of the valvular leaflets. It is possible to obtain information about the valve position from clinical images, which provides the input for simplified kinematic models. In Domenichini et al. [114], the motion of the 3D valve is described with its opening angle, derived dynamically from images. In the works of Seo et al. [111] and Vedula et al. [115] the measurements from cardiac ultrasound images are matched with anatomical atlases to obtain the valvular shape (Fig. 6.8 c, upper panel) and the opening angle of the valve (Fig. 6.8 c, lower panel). The motion is simplified and governed by the opening angle of the valve. In the work of Mihalef et al. [110], the availability of high resolution CT images allowed for the generation of a valvular geometry based on landmark position and statistical models. In the work of Chnafa et al. [106], the position of the valvular annulus and of the free edge is extracted from CMR images, the valve is reconstructed as a 3D volume connecting the annulus and the free edge. The valve is represented either in the open or in the closed position and no transition phase is included in the simulation. In the above-mentioned models, no curvature is considered in the model of the valve. With the exception of the work of Chnafa et al. [106], the thickness of the valve is also not accounted in the computation (e.g. in [114] [111]), as shown in Fig. 6.9.

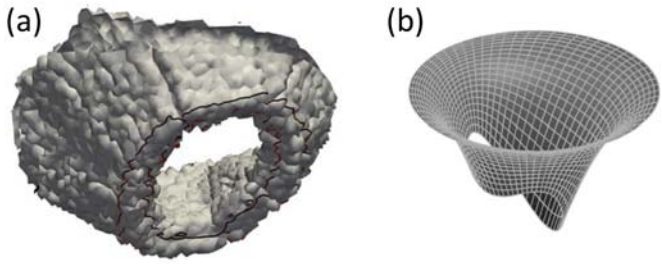

Figure 6.9: (a) Valve model with 3D thickness (adapted from [106]). (b) example of valve model without 3D thickness (adapted from [114]).

In the work presented in chapter 7 and 8, the kinematic approach based on clinical images is adopted to investigate the hemodynamics of pathological LV. The kinematic approach is adopted for both the moving LV and MV. In particular, our model is based on pre-operative, real-time transesophageal images, routinely acquired during cardiovascular surgical procedures. As the described procedure is fully based on the ALE-formulation for the mesh discretization, the remeshing of the fluid domain is required, which is automatically managed within the fluid solver and not planned with the generation of intermediate computational grids. In contrast with the above-mentioned works, the position of the valve is not estimated from atlases or imposed by means of opening angles, but it is obtained from segmented ultrasound images and imposed in the CFD model with the same kinematic technique used for the ventricular motion. The use of an automatic and powerful segmentation technique [44] allowed to extend the approach used for the ventricle to the valve.

CHAPTER 7

Patient-specific CFD simulation of intraventricular hemodynamics based on 3D ultrasound imaging

The goal of this chapter is to present a CFD model with moving boundaries to study the intraventricular flows in a patient-specific framework. Starting from the segmentation of 3D rt-TEE images, a CFD model including the complete left ventricle and the moving 3D mitral valve was realized. Their motion, known as a function of time from the segmented ultrasound images, was imposed as a boundary condition in an ALE framework. The model allowed for a realistic description of the displacement of the structures of interest and for an effective analysis of the intraventricular flows throughout the cardiac cycle. The model provides detailed intraventricular flow features, and highlights the importance of the 3D valve apparatus for the vortex dynamics and apical flow. The proposed method could describe the hemodynamics of the left ventricle during the cardiac cycle. The methodology might therefore be of particular importance in patient treatment planning to assess the impact of mitral valve treatment on intraventricular flow dynamics. The following of this chapter has been adapted from the published paper *"Patient-specific CFD simulation of*

*intraventricular haemodynamics based on 3D ultrasound imaging"**[6].

7.1 Introduction

With the increasing incidence of heart failure, there is a renewed clinical interest in ventricular vortex dynamics that are thought to contribute to the energetically efficient filling and emptying of the heart. Computational models based on patient specific data can contribute to our understanding of ventricular pathophysiology and the efficiency of ventricular dynamics. Based on the currently available imaging techniques of the cardiac structures, it is possible to generate advanced computational models which can, within the limits of the chosen numerical tool, reproduce a realistic scenario and provide additional information on the fluid-dynamics of the LV [116]. The goal of this work is to generate a CFD-based model with moving boundaries using the ALE formulation for the entire domain, to study the intraventricular flow in a 3D patient-specific framework. The model is based on segmented rt-TEE, from which the patient-specific geometry and the position of the LV and fully three-dimensional MV are derived. Compared to the available literature (e.g. [94] [105] [29] [111]), the proposed model and framework has the advantage of being patient-specific in both the LV and MV geometry and kinematics and the model of the valve is three-dimensional, not requiring additional assumptions over its geometry and thickness. The presence of the valve provides more realistic flow patterns during diastole, while during systole the coaptation is provided with a dedicated contact function.

7.2 Materials and methods

7.2.1 Patient selection and ultrasound images segmentation

For this pilot study, one patient was selected on the basis of the clinical information and images available. The selection criteria for the patient were the inclusion of the entire MV and LV structures in the field of view of the pre-operative rt-TEE images and the absence of stitching artifacts. From the clinical point of view, the absence of mitral regurgitation was required. The imaging protocol was approved

*A. M. Bavo, A. M. Pouch, J. Degroote, J. Vierendeels, J. H. Gorman, R. C. Gorman and P. Segers, 'Patient-specific CFD simulation of intraventricular haemodynamics based on 3D ultrasound imaging', *BioMedical Engineering OnLine*, vol. 15, no. 1, p. 107, 2016

by the University of Pennsylvania School of Medicine Institutional Review Board. Major clinical features included severe aortic stenosis, moderate global systolic dysfunction and severe hypokinesis of the LV, the patient was identified for aortic valve replacement. Pre-operative 3D rt-TEE gated images were acquired with an iE33 scanner (Philips Medical Systems, Andover, MA). The frame rate was 17 to 30 Hz with an image depth of 14 to 17 cm. The images were acquired over four consecutive cardiac cycles and reconstructed into one cardiac cycle to obtain the desired full field of view. The 3D rt-TEE images contain the entire LV and MV in the field of view. The segmentation of the MV in these images was performed with a combination of multi-atlas joint label fusion and deformable medial modelling techniques, which generate 3D geometric models of the MV [44]. The model can accurately replicate different geometrical configurations (closed in Fig. 7.1 a, and open in Fig. 7.1b) of the valve and captures the atrial and ventricular surfaces with a high level of detail. Furthermore, the technique represents the valve volumetrically, which enables localized measurement of leaflet thickness. To obtain similar image-derived models of the LV without reference data for multi-atlas label fusion, semi-automated image segmentation of the LV was performed in ITK-SNAP [117] at one frame in systole (Fig. 7.1 c), and deformable registration [118] was used to propagate that segmentation to all the other frames in the image series. Further details on the segmentation technique are beyond the scope of this text, and the reader is referred to [44] for more information.

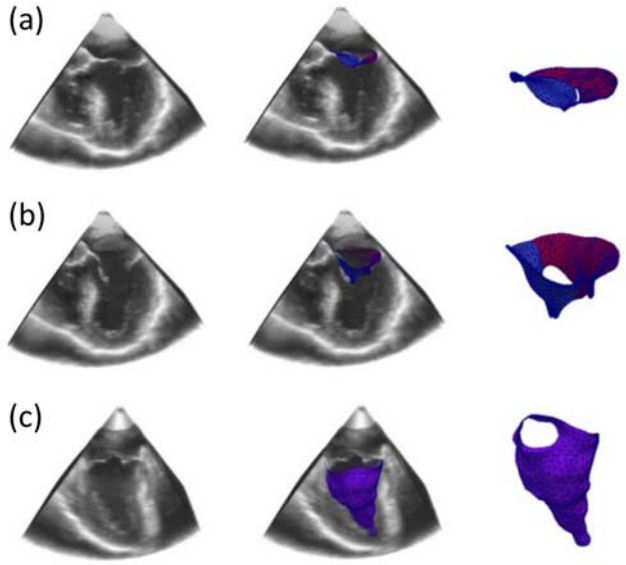

Figure 7.1: From rt-TEE ultrasound images to segmented triangulated surfaces. (a) MV in closed configuration. (b) MV in open configuration. (c) LV during systole.

The results of the segmentation were two sets of segmented geometries, one for the LV and one for the MV, each composed of 18 time frames representing one complete cardiac cycle. Thus, the positions of the structures of interest were known throughout one cardiac cycle. For contact management during systole, an artificial gap was imposed in the coaptation area of the valve, such that the anterior and posterior leaflets of the MV were not in complete closure during systole. In the following we will refer to the segmented geometries as "motion input meshes", as they were used as input to prescribe the motion of the MV and LV during the simulations. The input meshes consist of triangulated surfaces, sharing the same topology (constant node numbers and triangles connectivity) during the cardiac cycle.

7.2.2 Numerical model

The motion of the boundaries has been implemented with extensive own programming in a CFD solver which supports the ALE framework. The details of the implementation are schematically listed in appendix A. All the CFD simulations were performed with the commercially available software Fluent (ANSYS 15.0 Inc., Canonsburg PA, USA),

which allows for the solution of the NS equations with a finite volume approach in an ALE formulation (Equations 2.8a and 2.8b). An implicit, first-order accurate, backward difference method for the time discretization and a second order upwind scheme for the spatial discretization were used.

7.2.3 Boundary conditions and material properties

As a starting point for the simulations, the late diastole was chosen, when the mitral valve was in the open position, the aortic valve was closed and the LV relaxed. At late diastole the valvular leaflets are considered to be in the free-stress configuration [119]. The realization of the patient-specific model was performed starting from the available segmented rt-TEE images at this time-point (Fig. 7.1 b-c). The motion input meshes of the MV and LV at late diastole were imported into pyFormex, an open-source, in-house written and python-based program which allows for the manipulation of large and complex geometries (www.nongnu.org/pyformex/). The final fluid domain consisted of the left ventricle, the left ventricle outflow tract, a simplified atrium (not available from the images) and the mitral valve. The computational domain is shown in Fig. 7.2.

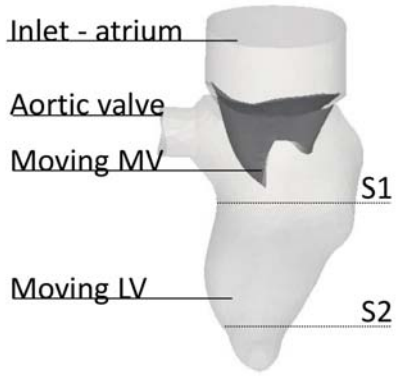

Figure 7.2: Computational domain with boundary conditions. Section S1 and S2 used to calculate the intraventricular pressures in chapter 7.3.3 are shown.

The mesh of the computational domain was realized with about $500K$ tetrahedral cells, resulting in an average element dimension

of $1.2mm$. The dimension of the mesh was assessed with a mesh sensitivity study, reported in appendix B. As boundary conditions, the motion of the LV and MV was mathematically described and implemented in the model with user-defined functions (more details in the following sections and in appendix A). All the remaining surfaces with the exception of the inlet surface are allowed to deform to follow the 3D complex motion of the annulus of the MV. The atrial surface was kept at a constant pressure (0 mmHg) throughout the entire cardiac cycle, as no pressure curves were available from the clinical data. The presence of the aortic valve is included with the on-off procedure, the switch between the open and closed configuration and vice-versa was instantaneous and automatically prescribed based on the flow rate. During systole, the aortic outlet was kept at the constant pressure of $100mmHg$, while during diastole the surface was converted to a wall. The blood was modelled as a homogeneous and Newtonian fluid, the values of density ρ and viscosity μ were chosen according to mean values for healthy subjects ($\rho = 1060Kg/m^2, \mu = 0.0035Pa \cdot s$).

7.2.4 Workflow

To prescribe the displacements of the structures of interest starting from the information available from the rt-TEE ultrasound imaging, three main steps were taken in the model. Prior to the simulation, a time interpolation was required to be able to transfer the displacement information from the time frames of the segmented meshes to the small time steps of the CFD simulations with smooth interpolating curves. As a second step, a space interpolation was required, to couple the motion of the input meshes and the computational mesh. As a last passage, before the solution of the NS equations, a contact detection algorithm was required, to ensure the correct treatment of the mitral leaflets coaptation during systole. The schematic workflow is depicted in Fig. 7.3 a.

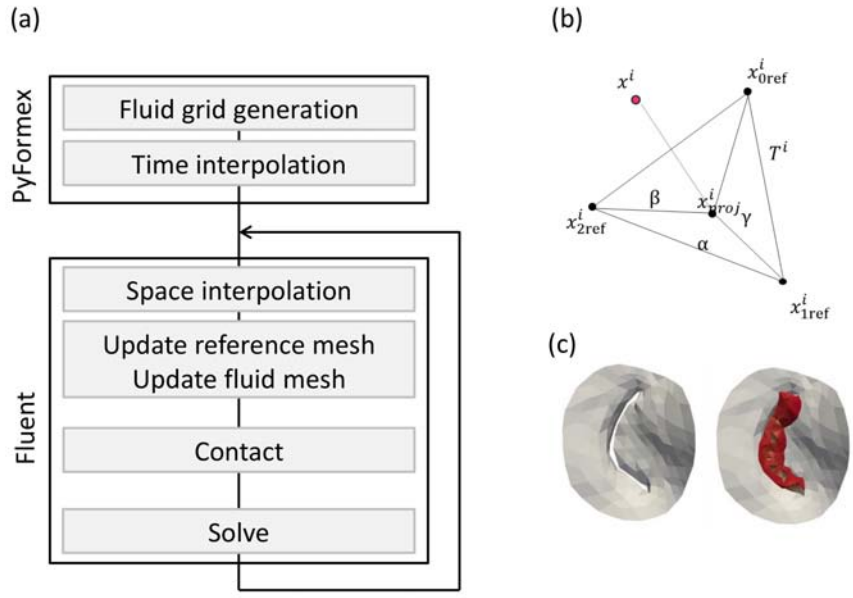

Figure 7.3: (a) Workflow of the implemented model, (b) schematic drawing of the space interpolation, (c) MV in the closed position, without and with the cells identified for contact (in red)

These steps are described in detail in the following sections and were implemented via user-defined functions, to modify the finite-volumes solving code according to the needs of the simulated scenario.

7.2.5 Time interpolation

The results of the segmentation process were two sets (one for the MV and one for the LV) of triangulated surfaces with a frame rate of 18 frames/cycle. This frame rate was not sufficient to replicate the motion of the walls in a CFD model (time-step used for the calculation equal to 0.5ms), therefore a time interpolation was necessary. Natural cubic splines (NCS) and Bezier splines (BS) were selected to interpolate the displacements of the LV and MV respectively. The NCS were chosen for the LV as they ensure the continuity and smoothness of the curve and its derivative. The drawback of the choice of NCS over the BS is that they have less local control on the interpolated points: this could lead to some overshooting in the estimation of the interpolation curve, especially if the points are not widely spaced. For this reason, the motion of the valve was described with third order Bezier splines, which guarantees more local control on the interpolation despite the possible loss of continuity in the derivative. To account for the

periodicity of the solution, the spline curves were calculated as closed curves, by appending the first frame after the last available frame. More considerations over this choice are presented in section 7.4.

7.2.6 Space interpolation

To impose the motion of the LV wall and valve, the position of the nodes of the fluid grid needed to be modified throughout the computation, which can be achieved in Fluent (as well as with other CFD packages) with a specific external function which updates the position of each point independently. Furthermore, it has to be taken into account that the segmented motion input mesh and the computational mesh have different resolutions. In the presented model, the updated position of the moving walls was obtained in three major substeps. As pre-processing step, the coefficients of the third-order interpolating curves are imported in the CFD solver. Then, with reference to Fig. 7.3 b, at each time-step, each point x^i belonging to the moving surfaces of the computational mesh is associated with the three closest points $(x^i_{0ref}, x^i_{1ref}, x^i_{2ref})$ on the input surface. Knowing the correspondent spline coefficients, the position of each input point is updated. The projection (x^i_{proj}) of each computational point on the triangle (T^i) generated by the three nearest points on the input surface is calculated and its barycentric coordinates (α, β, γ) with respect to this triangle are calculated. Finally, the displacement of the computational point is calculated as a linear combination of the displacements of the three points weighted with the barycentric coordinates [120]. Further details about the space interpolation can be found in appendix A.

7.2.7 Contact of mitral leaflets

The coaptation of the valve leaflets during systole is problematic for the ALE formulation as the complete closure of the MV would eventually result in the separation of the domain and consequently failure of the simulation. To overcome this limitation, prior the simulation a gap in the MV motion input meshes during systole was ensured (Fig. 7.3 c). By doing so, the anterior and posterior leaflets never experienced a contact condition. Without any additional measures, this technique introduces an artificial transmitral backflow during systole. This was prevented with the development of a dedicated contact function which identifies the faces considered in contact and the fluid cells lying in the artificial gap. A triangular face and a node (which does not belong to an adjacent face) of the valvular surfaces are considered to be in contact if their distance is smaller than a

predefined threshold based on the dimension of the artificial gap, if their normals are parallel (within a tolerance range) with opposite directions and if the center of one face projected along its normal falls within the second face. If these criteria are fulfilled, the face under consideration and the face to which the node belongs are considered to be in contact and all the fluid cells lying between them are then flagged for contact, with an iterative identification process. Ten iterations were sufficient to completely fill the gap (Fig. 7.3 c). To increase the hydraulic resistance of the cells lying in the gap and therefore reduce the artificial backflow, an external momentum source term $\int \vec{f_f}$ was introduced on the right-hand side of Eq. 2.3 for the identified cells. For each selected j-th cell, this term resulted in:

$$f_j = C_0 v_j \tag{7.1}$$

with v_j the fluid velocity in the j-th cell and C_0 a constant coefficient for the momentum source [121]. A separate set of tests was performed to identify a suitable value for the C_0 coefficient ($0.1 kg/s$). This technique did not intend to mimic any physiological phenomenon and the constant coefficient of the momentum source term was chosen as a trade-off between the reduction of the mitral backflow and the stability of the solution procedure. Further details about the contact algorithm are provided in appendix A.

7.2.8 Fluid-dynamics evaluation criteria

Besides the standard analysis of the flow field, of particular importance is the analysis of the vortex structure formation and evolution. The vortex structure can be identified with the λ_2 criterion [122]. This method relates the vortex formation to the areas where minimum values of pressure are associated to the rotation of the flow field. It has been shown that by taking the symmetric and asymmetric parts ($S_{ij}S_{kj} + \Omega_{ij}\Omega_{kj}$) of the velocity gradient tensor, the condition of the second invariant $\lambda_2 < 0$ provides an indication for the vortex location [122] [123].

As local pressure differences in the ventricular chamber have an influence on the vortex formation and efficient ventricular filling, the intraventricular pressure distribution at significant time-points is reported. Pressure values are relative to the uniform pressure assumed as boundary conditions. The intraventricular pressure difference ΔP is calculated between the section S1 near the base of the LV, and S2 near the apex (see Fig. 7.1 d for the exact locations), with $\Delta P = p_{base} - p_{apex}$. The WSS are also reported.

As a proof of concept, in chapter 7.3.4 we also report a comparison between the complete model and the model where the mitral valve was removed, to explicitly test and discuss the influence of the 3D valvular leaflets on the results of this type of simulation [111].

7.3 Results

Two cardiac cycles have been simulated. The results from the second cycle (starting and concluding at late diastole, such that the influences of the closing valves are visible in the results) are presented in the following, to eliminate the influence of the initialization from the results. The simulations were run on a Dell PowerEdge R620 server (2× Intel Xeon E5-2680v2 CPUs at 2.8Ghz) with one core used, and needed about 8h to complete. The use of one core was required by the contact algorithm, which was not yet optimized for parallel calculation.

7.3.1 Contact management

Without any increase in the hydraulic resistance of the fluid cells in the coaptation zone, the artificial gap between the leaflets in combination with the transvalvular pressure difference ($100 mmHg$) resulted in a significant backflow during systole (61% of the total forward flow). The contact function, with the momentum source term in the NS equations and the selected C_0 coefficient, reduced the unwanted backflow to 6% of the forward flow. This residual transmitral flow during systole could not be, at this stage, further diminished, as additional increase of C_0 led to numerical instabilities. The results shown in the following sections are obtained with the activation of the contact function.

7.3.2 Motion of the boundaries

The described interpolation process, together with an optimal segmentation technique, generated a realistic boundary motion for the model, yielding physiological movement of the structures of interest. In Fig. 7.4, the comparison between rt-TEE ultrasound images, the segmented geometries (Fig. 7.4 a) and the corresponding time-points from the simulations (Fig. 7.4 b) are reported, at four instants throughout the cardiac cycle. In Fig. 7.4 c the artificial gap is visible for the two time-points of diastole (Fig. 7.4 c: i-ii). The mass balance was fulfilled throughout the cardiac cycle, with the mass flow rate entirely defined by the motion of the structure, and the change in volume balanced by the inlet and outlet flows. The volume of the LV obtained from the motion input meshes was realistic. The described time interpolation

did not introduce significant errors, as the maximum difference in the ejection fraction between the input geometries and the interpolated geometries is below 2%.

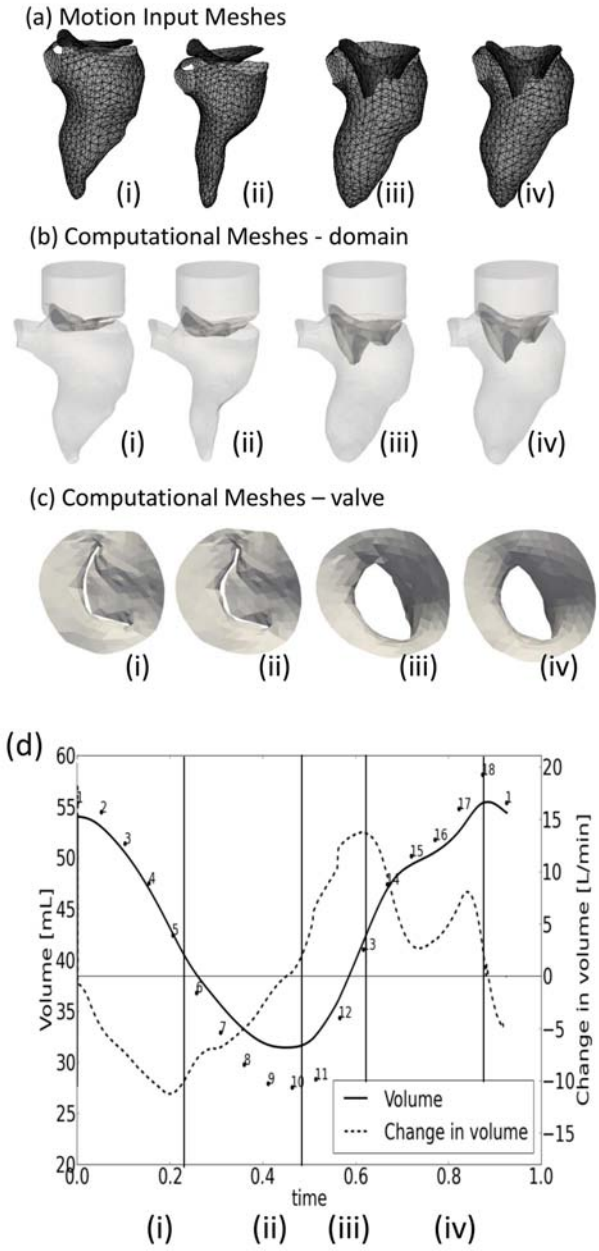

Figure 7.4: Prescribed motion of the boundaries. Comparison between (a) the motion input meshes and (b-c) the computed meshes, complete domain and top view of the MV, in four time-points (d) of the cardiac cycle

7.3.3 Flow field

The main flow field results at 3 significant time points in systole are reported in Figure 7.5 (acceleration in Fig. 7.5 a, peak of systole in Fig. 7.5 b, deceleration in Fig. 7.5) with an overlay of the deformation of the LV, the velocity streamlines and vortex structures. In Fig. 7.5 d, the pressure field and the velocity vectors over a section at the peak of systole are reported, in Fig. 7.5 e the WSS at peak of systole are shown.

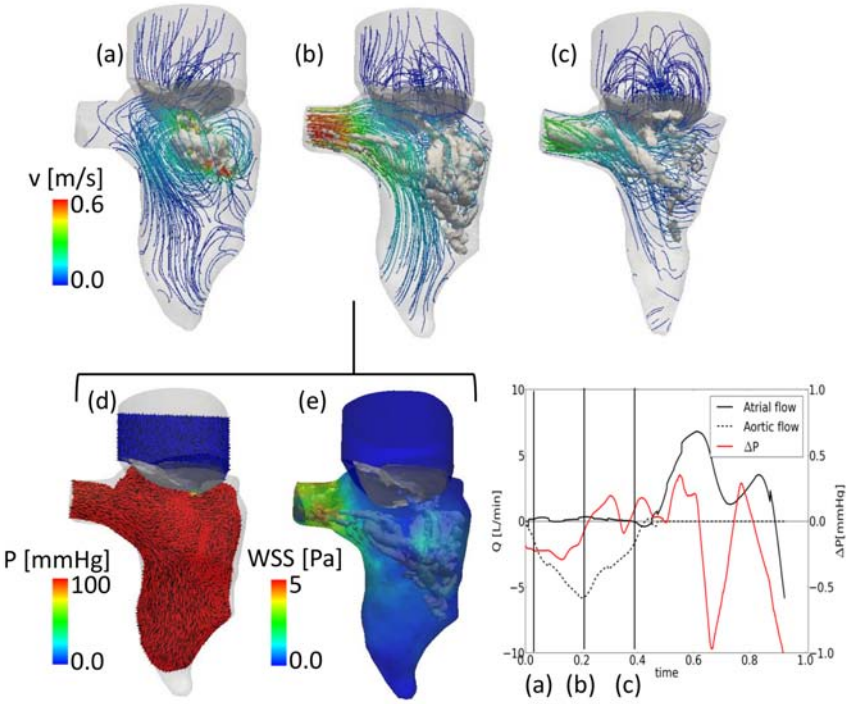

Figure 7.5: Systolic flow field. Streamlines and vortex structure (λ_2) (a-c). Pressure and velocity vectors in the LV (d, e) on a section at peak of systole. Right panel: Flow curve and the intraventricular pressure difference (base – apex) during the cardiac cycle. The time-points used in (a-c) are indicated.

At the beginning of systole (Fig. 7.5 a), a limited flow is present at the aortic outlet, as the MV ended its closing phase and contraction of the left ventricle has yet to occur. A low intensity recirculation area is visible in the center of the LV, in the area below the valvular orifice (Fig. 7.5 a). Due to the periodicity of the solution, this vortex is a residual of the vortex generated during the preceding diastole.

The closure of the mitral valve could also contribute to the formation of this structure and could especially influence its location, close to the lateral wall of the LV. As soon as the contraction of the LV begins, the flow vectors align, culminating at the peak of systole (Fig. 7.5b), when the velocity of the blood leaving the LV is the highest ($v_{max} = 0.6m/s$) and the reduction of the volume of the LV is already significant. At this stage, a complex vortex structure is delineated at the lateral wall of the LV (Fig. 7.5 b). The blood decelerates during the late systole, while the LV concludes its contraction. In Fig. 7.5 c, the LV reaches its minimal volume at the end of the systolic phase, and the deceleration of blood gives rise to a helical flow pattern at the aortic location. The vortex structures are washed out of the ventricle during the late systolic phase. During the entire systolic phase, the atrio-ventricular pressure difference is about $100mmHg$, coherent with the imposed boundary conditions (Fig. 7.5 d). In Fig. 7.5 e, the wall shear stress plot at peak of systole shows high values at the aortic outlet, as the velocity of the blood in this region is the highest. Areas of relatively high WSS are also detected in the region where the vortex structures are present.

The contact implementation guarantees a good sealing of the valve despite the presence of the artificial gap. Smaller intraventricular pressure differences are not visible in the color plot of this cardiac phase, as they are of two/three orders of magnitude smaller than the transvalvular pressure difference. As visible in the graph (Fig. 7.5, right panel), however, the intraventricular pressure (calculated as the average pressure difference between the surface S1 at the base and the surface S2 at the apex of the LV (Fig. 7.1d) shows small pressure variations ($\pm 0.2mmHg$) in the ventricle. In the acceleration phase (until $t = 0.25s$), there is an expected negative intraventricular pressure, while during the deceleration phase the intraventricular pressure difference is inverted due to the blood deceleration.

The results during diastole are shown in Fig. 7.6.

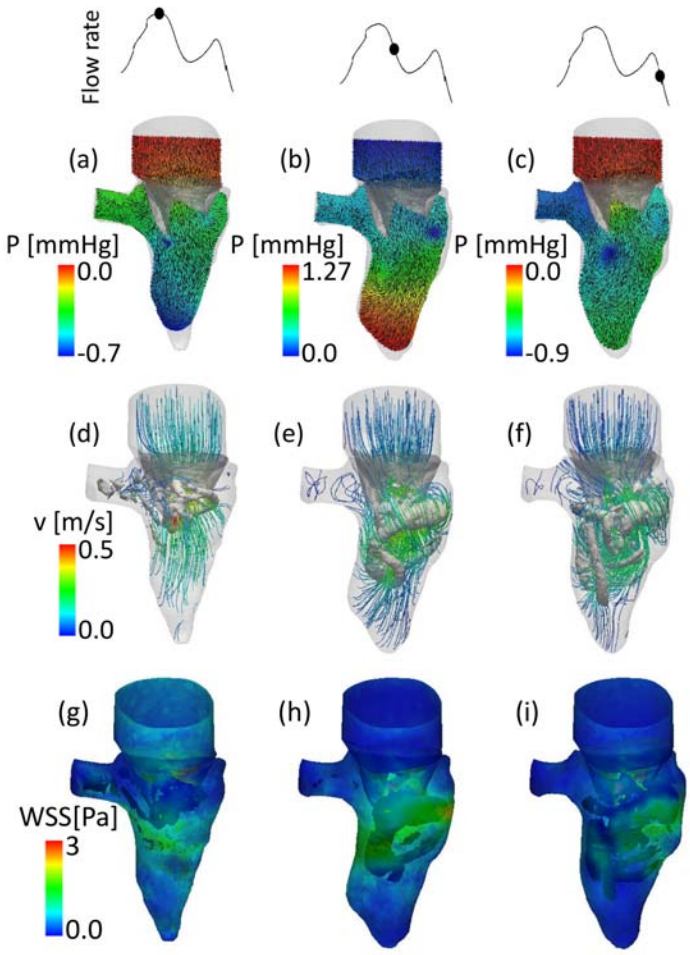

Figure 7.6: Diastolic flow field. Pressure and velocity vectors in the LV (a-c) on a section. Streamlines and vortex structure (λ_2) (d-f). WSS at the walls (g-i). Please note that the color scale for the pressure difference changes in each panel.

Fig. 7.6(a-c) reports the pressure and the velocity vectors on a section, Fig. 7.6(d-f) the velocity streamlines and vortex structures, Fig. 7.6(g-i) the wall shear stress. During the diastolic phase, the pressure in the ventricle decreases to the atrial pressure, in this case $0mmHg$, as imposed from the boundary conditions. At early diastole (Fig. 7.6a), a negative intraventricular pressure is generated (E-peak). The intraventricular pressure is then reversed during the blood deceleration phase (Fig. 7.6 b) to become again negative during the A-peak towards the end of the diastole (Fig. 7.6 c). The variation of

the intraventricular pressure difference (base – apex) throughout the cardiac cycle is reported in Fig. 7.5f. Please note that during diastole, the intraventricular pressure difference is expected to be positive during acceleration and negative during the deceleration phase, due to the location of the planes on which the pressure difference is measured. This is the opposite to what is expected in systole, due to the opposite direction of the blood flow.

The early diastolic flow (E-peak) is characterized by a peak velocity in the valvular orifice area. A vortex structure is generated at the valvular edges, visible both from the small negative pressure areas at the leaflets in Fig. 7.6a and from the vortex and streamlines in Fig. 7.6d. During the deceleration phase, the vortex has significantly increased in size and detached from the valvular edges (Fig. 7.6e). The shape of the vortex becomes complex and it migrates towards lower regions of the LV. At the lateral wall, the vortex impinges on the ventricular wall (fig. 7.6e), starting the dissipation [124]. The dissipation of the vortex continues during the late diastolic phase, as visible in Fig. 7.6f. The second peak (A-peak) is not clearly visible from Fig. 7.6f, as the flow field is chaotic and the vortex structure widespread in the LV. The A-peak is detected in the ventricular motion and in the transmitral flow, but no second re-opening phase of the mitral valve is detected. The WSS is higher in the regions where the vortex reaches the ventricular walls. The mitral leaflets are also subjected to high values of WSS, due to the transmitral flow during diastole.

7.3.4 Influence of the valvular leaflets

As the presence of the valve significantly influences the flow field and the vortex formation in the LV [111], we also compared the same model with and without the MV. An additional model was created with an analogue geometry in which the valve was removed and replaced with an orifice. The orifice was obtained by projecting the widest MV aperture on the valvular plane, to ensure a peak velocity comparable to the velocity measured in the model with the full 3D valve. The aperture of the valve orifice was considered constant in time and the valve operated in an on/off mode as described for the AV. In Fig. 7.7, the results of the model without the valve are shown at peak systole (Fig. 7.7a) and in diastole (Fig. 7.7b-d).

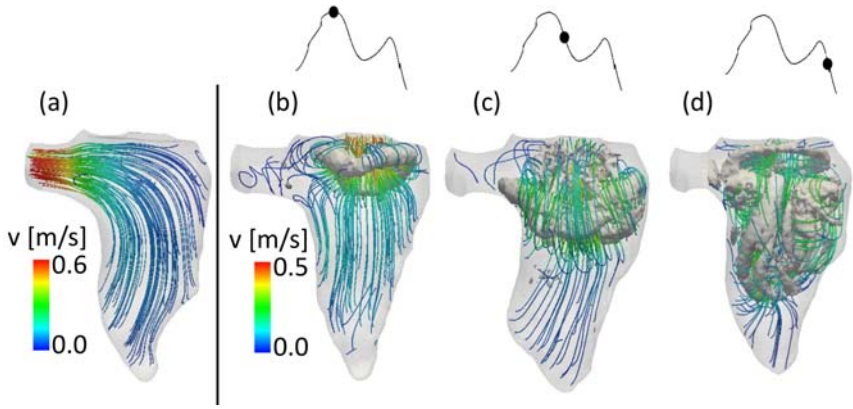

Figure 7.7: Flow field for the model without the valve: vortex and velocity streamlines at peak systole (a) and in three time-points during diastole (b-d).

At peak systole (Fig. 7.7a), the flow is nicely aligned with the outlet and no vortex structures are detected at this point, while in Fig. 7.5b some disturbance of the flow is present and residual vortex structures have accumulated near the lateral wall of the LV. At the beginning of diastole (Fig. 7.7b), the vortex arising from the valvular orifice is much more regular than the vortex that is obtained with the 3D valve (Fig. 7.6). The vortex ring has the saddle shape of the orifice, but the absence of the leaflets prevents the higher velocities at the commissures and therefore the generation of an irregular and curved vortex structure. In Fig. 7.6c-d the difference becomes more clear. In the model with the valve, the vortex is pushed by the valvular leaflets towards the lateral and septal walls, where it impacts leading to the dissipation of the structure. Without the valve, the vortex remains in the central zone of the LV, travelling forward towards the apex without significant dissipation (Fig. 7.7c). With the valve, the flow streamlines are more complex and the fluid structures reach more apical zones of the left ventricle. Without the valve, less blood reaches the apex, leading to a less optimal washout of the area. These findings are in good agreement with [111].

7.4 Discussion

In this section, we have described a patient-specific CFD model of the left ventricle, including the moving ventricular wall and the full three-dimensional mitral valve segmented from rt-TEE images. The methodology offers advantages over the existing works, in particular

for (i) the use of clinically available rt-TEE ultrasound images as a base for the motion, (ii) the inclusion of the full 3D valve in the model and (iii) the use of the ALE technique for the discretization of the NS equation. In particular, the availability of the ultrasound images, routinely acquired during any surgical procedure, cheaper and less invasive for the patient, provide a good ground for the generation of a model with the potential to become a clinical evaluation and/or surgical planning tool. Previous works based on ultrasound have been proposed [124] [125], but the valvular structure was not included in their model.

7.4.1 rt-TEE images

While the rt-TEE echo data offers the advantage of a sufficient spatial resolution to resolve and segment the mitral valve apparatus and leaflets, the frame rate is relatively low, which does not allow to include the iso-volumetric phases of the cardiac cycle and enforces the use of temporal interpolation. As also, the opening and closing time of the valve were determined by the frame rate of the reference meshes, the model does not provide any insights into the opening and closing time of the MV. However, the frame rate of the rt-TEE images was sufficient to capture the significant events of the cardiac cycle in the ventricle, for example the typical two peaks of the transmitral diastolic flow and the transmitral velocity magnitudes which are realistic.

7.4.2 Modelling choices

The use of NCS to interpolate the reference points of the ventricular mesh overcame some of the limitations of the available studies [29] [107] [32] [112]. The choice of NCS for the interpolation of the displacement of the LV resulted in a wall motion and ejected volumes which were coherent and physiologically plausible (Fig. 7.4), yielding more realistic simulation results than previously used interpolation schemes [107] [32] [112] [29]. Nevertheless, the choice of using BS to describe the motion of the leaflets was visible in the flow curve (Fig. 7.4d) where small discontinuities were visible. However, as the bulk flow is defined by the LV motion, and therefore prescribed with a smooth and continuous curve, we expect that this has only a minor effect on the overall fluid dynamics.

The use of the ALE technique for the NS equations requires specific attention for the treatment of distorted cells that inevitably occur in a deforming geometry such as a LV. The use of spring-based deformation methods for the mesh motion and automatic remeshing of the fluid domain are necessary to guarantee a good quality mesh

during the cardiac cycle and removed the need for intermediate meshes, as previously used in intraventricular flow studies based on the ALE method [107] [32] [112] [29].

7.4.3 Intraventricular flow

Given that the presented model is based on imaging data from a patient with aortic stenosis, the results obtained reflect the patho-physiology of the case under investigation. The relatively low magnitude of the volume and flow curves is related to the ventricular pathology of the patient and the small size of the heart, confirmed by the clinical intra-operative report. The capability of the model to capture interesting details of the intraventricular haemodynamics was shown in Figs. 7.5 and 7.6. In particular, the CFD modeling allowed for the analysis of variables which are otherwise not directly available from the clinical images, e.g. 3D vortex visualization, WSS and intraventricular pressures. The structure and the evolution of the vortex structure throughout the cardiac cycle were in agreement with the published data for a similar set up [110] [111] [115]. The patient-specific details of the valvular anatomy played an important role in the vortex formation and the asymmetry of the mitral valve resulted in a saddle-shaped vortex ring [110] [115]. The transvalvular pressure difference during systole is coherent with the imposed boundary conditions, showing the capability of the contact implementation of sealing the valve during this phase. The model also yields physiologically plausible intraventricular pressure variations, which may be of clinical interest especially for the assessment of diastolic function [123]. The analysis of the WSS at the ventricular walls showed the presence of high values of WSS close to the vortex location during the cardiac cycle. In fact, the blood velocities generated at the vortex core become tangential to the walls when the vortex structure approaches it, therefore resulting in areas of high WSS values [124]. The comparison between the model with and without the valvular leaflets (Fig. 7.7) highlights the importance of the presence of the valve in the computational model to achieve realistic features of the vortex field, in particular the penetration depth of the vortex ring to the apical region. These results are in line with observations of [29], comparing CFD model results with MRI flow recordings and with the findings of [111], who studied the impact of the presence of a valve in a CFD model based on LV CT scans and a physiology-inspired model valve.

7.4.4 Limitations and future works

Previous studies have demonstrated that the upstream boundary conditions can have an impact on the ventricular flows [29] [110]. In

our model, the geometry of the atrium was very simplified, as the field of view of the rt-TEE images was limited to the LV and MV. Furthermore, probably due to the low frame rate, the mitral leaflets do not experience an appreciable second opening during the A-peak of diastole. More realistic upstream geometries will be taken into account in the future. The aortic valve and the inner topology of the LV (trabeculae and papillary muscles) were not included in the model yet, while it has been shown they influence the ventricular flow field [115] [126]. The assumption of the Newtonian model for the blood also introduces approximations in the results, as the blood in the ventricle, especially in the apex, can reach very low velocities, at which the Newtonian hypothesis is no longer fully valid [29] [127]. More sophisticated models for the blood will be investigated in the future.

The model can accurately reproduce only the velocities perpendicular to the walls. The in-plane velocities of the moving walls are smaller and do not influence the changes in volume of the ventricle, however, they can produce shear at the walls which could interact with the vortex structures. The segmentation technique adopted might be able to capture the torsion of the LV, as it is performed in 3D over time, but it has not been rigorously tested for the in-plane velocity detection accuracy yet. Due to the interpolation process from the input mesh to the computational mesh,no torsional effects of the ventricle can be discussed.

7.5 Conclusions

In this chapter we have introduced and described a methodology that allows to construct a patient-specific CFD model with imposed moving boundaries, including the three-dimensional mitral valve obtained from real-time transesophageal ultrasound images. The model uses uniquely the ALE framework and, to the best of our knowledge, it is the first time a realistic 3D valve has been included with this approach. Besides the patient-specific and anatomically correct nature of model, the presented interpolation and remeshing methodology is numerically efficient, and compliant with an ALE formulation thanks to the introduction of a leaflet contact detection algorithm. The model provides detailed intraventricular flow features, and highlights the importance of the 3D valve apparatus for the vortex dynamics and apical flow. The methodology might therefore be of particular importance in patient treatment planning to assess the impact of mitral valve treatment on intraventricular flow dynamics.

Chapter 8

Patient-specific CFD models for intraventricular flow analysis: comparison of three clinical cases

8.1 Introduction

In chapter 6 the utility of the intraventricular flow analysis has been explained and the advantages of having powerful computational tools to predict and estimate the fluid dynamics in the LV has been discussed. In chapter 7 a novel CFD approach based on clinical images has been proposed and described, highlighting the methodologies and its drawbacks. In this chapter, the application of the CFD model described in chapter 7 to a set of patients is presented, to verify the abnormal flow patterns in impaired hearts. One case (Patient 1 (P1)) had a normal ejection fraction but a low stroke volume and cardiac output, Patient 2 (P2) showed a low stroke volume and a reduced ejection fraction, Patient 3 (P3) had a dilated ventricle and a reduced ejection fraction. The results suggest that the shape of the ventricle and mitral valve influence the flow field in the left ventricle, leading to distinct flow features depending on the pathology. Of particular interest is the pattern of the vortex formation and evolution, influenced by the valvular orifice and the ventricular shape. The base-to-apex pressure difference of maximum 2 mmHg is consistent with

reported data. The following of this chapter has been adapted from the published paper *"Patient-specific CFD simulation of intraventricular haemodynamics based on 3D ultrasound imaging: comparison of three clinical cases"*[*][7].

8.2 Materials and methods

8.2.1 Patients selection and ultrasound images segmentation

Three patients, scheduled for aortic or mitral valve surgery, were included in the analysis on the basis of their LV characteristics and clinical indications (Table 8.1).

All patients underwent the routine pre-operative rt-TEE ultrasound examination. The imaging protocol was approved by the University of Pennsylvania School of Medicine Institutional Review Board and informed consent was obtained from the patients regarding the use of the imaging data for research purposes. The procedure of acquisition and segmentation is consistent with the procedure described in chapter 7.2.1 and will not be reported here. For the three patients the field of view of the images included the LV and MV, which were segmented with a combination of multi-atlas joint label fusion and deformable medial modeling techniques, as described in chapter 7.2.1, to obtain a 3D geometric model [44]. The segmentation provided two sets of triangulated surfaces per patient, used as a starting point for the CFD model.

8.2.2 CFD model with prescribed moving boundaries

The implemented CFD model has been described in full details in chapter 7.2.4. The Navier-Stokes equations were solved with a finite volume approach in ALE formulation where the motion of the boundaries was implemented with extensive own programming in the CFD solver in use (ANSYS Fluent 15.0, Inc., Canonsburg, PA, USA). The segmented surfaces provide the position of the MV and LV in discrete time-points of the cardiac cycle and this information is used to prescribe their kinematics for the CFD simulation, as described in chapter 8. The simulations were run on a Dell PowerEdge R620 server (2× Intel Xeon E5-2680v2 CPUs at 2.8Ghz) with eight CPUs used.

[*]A. M. Bavo, A. M. Pouch, J. Degroote, J. Vierendeels, J. H. Gorman, R. C. Gorman and P. Segers, 'Patient-specific CFD models for intraventricular flow analysis from 3D ultrasound imaging : comparison of three clinical cases', *Journal of Biomechanics*, 2016

Table 8.1: Clinical pre-operative indications. Abbreviations: Ax1, Ax2: major and minor axis of the LV. EDV: end diastolic volume, SV: stroke volume, EF: ejection fraction, CO: cardiac output, MV: mitral valve, AV: aortic valve, CAD: coronary artery disease.

	LV size	Ax1 [mm]	Ax2 [mm]	EDV [mL]	SV [mL]	EF%	Heart rate	CO [L/min]	MV regurgitation	Clinical indication	Surgical procedure
P1	Normal	73	43	58	30	52%	61bpm	1.83	Trace	Hypokinetic wall Moderate concentric hypertrophy	AV replacement
P2	Normal	81	39	55	20	36%	62bpm	1.24	Mild	Impaired relaxation	AV replacement
P3	Dilated	105	100	250	55	22%	77bpm	4.23	Mild	Severe diastolic dysfunction Severe hypokinesis	MV repair and CAD

8.2.3 Boundary conditions and material properties

For the comparison of the three cases, the simulations are limited to the diastolic phase and the effect of any possible residual systolic flow feature is neglected. The motion of the MV and LV is imposed as a boundary condition, derived from the clinical images and a uniform pressure was imposed at the inlet of the atrium. No outlet was identified: during diastole the aortic valve is closed and no aortic regurgitation is modelled. Blood was considered as a homogeneous and Newtonian fluid, with standard values of density ρ ($1060kg/m3$) and viscosity μ ($0.0035Pa \cdot s$). To include the effects of the opening valve, the simulation was started at late systole, with the mitral valve closed and the LV in its smallest volume configuration. No contact detection algorithm is included in the set-up, as only the diastolic phase is simulated.

8.2.4 Fluid-dynamic evaluation criteria

The criteria used to evaluate the flow field are consistent with those described in chapter 7.2.8. The analysis of the vortex structure formation and evolution in the LV is quantified with the λ_2 criterion [122]. Specifically for this comparison, pressure values are relative to the uniform pressure assumed at the atrial inlet. We calculated the intraventricular pressure difference ΔP throughout diastole between the cross sections CS1 near the base of the LV, and CS2 near the apex (see Fig. 8.1 for the exact locations), with $\Delta P = p_{base} - p_{apex}$.

We calculated the viscous energy dissipation, derived from the Navier-Stokes equation and the conservation of energy combined with the assumption of a homogeneous, incompressible, Newtonian and isotropic fluid as:

$$\Phi = 2\mu[(\frac{\partial u}{\partial x})^2+(\frac{\partial v}{\partial y})^2+(\frac{\partial w}{\partial z})^2]+(\frac{\partial u}{\partial y}+\frac{\partial v}{\partial x})^2+(\frac{\partial u}{\partial z}+\frac{\partial w}{\partial x})^2+(\frac{\partial v}{\partial z}+\frac{\partial w}{\partial y})^2 \tag{8.1}$$

where μ is the fluid viscosity [30].

8.3 Results

8.3.1 Patient-specific data

Fig. 8.1 displays the fluid domains of the three patients from chosen views showing the anterolateral and the posterior side of each geometry at late diastole.

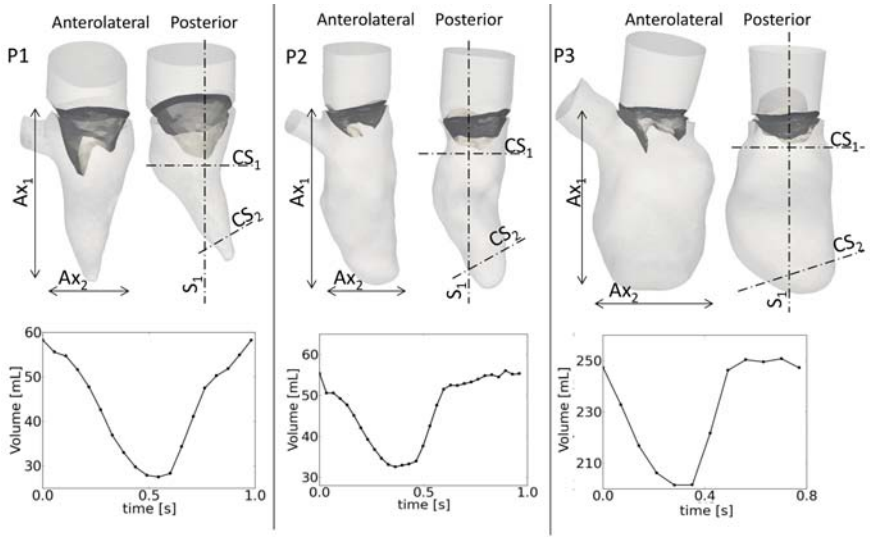

Figure 8.1: Upper panel: patient geometries, showing the anterolateral and posterior walls of the LV. The dimensions of the major (Ax1) and minor (Ax2) axes are reported in table 8.1. Lower panel: LV volume curves calculated from the segmented ventricles. Sections S1, CS1 and CS2 used to report relevant results in Fig. 8.4 and 8.5.

P1 has a moderate concentric hypertrophy, with a preserved EF. The LV volume in the second patient is comparable to P1, but the ejection fraction is reduced and the ventricle has an elongated shape. The third patient has a severe ventricular dilatation, with dimensions substantially larger than the other subjects (Table 8.1). The volume curves during the entire cardiac cycle are reported in the lower panel of Fig. 8.1 for the three cases. The remodeling and enlargement of the ventricle of P3 is evident from the volume curve and the impaired status of the heart is confirmed by an extremely low EF (22%).

The ventricles and valves for the three patients are shown for three time-points (late systole, E-peak and late diastole) in Fig. 8.2.

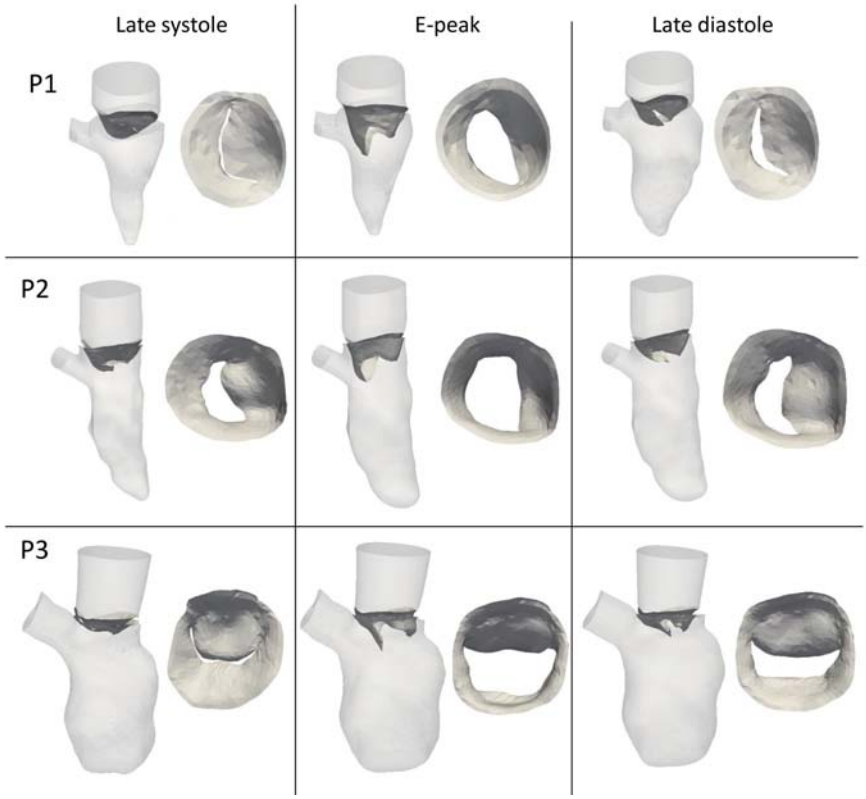

Figure 8.2: Moving walls and valvular leaflets in the three patients at late systole, E-peak and late diastole.

8.3.2 Intraventricular flow and pressure field

In Fig. 8.3, the volume flow rate curve, the base-to-apex pressure difference (left panels) and the viscous energy dissipation (right panels) are reported.

While there was a prominent E-peak in all cases, the A-peak was present for P1 only (flow curve, solid line). The intraventricular pressure difference curves (dotted line, left panels of Fig. 8.3) show a similar trend in the three cases until the end of the E-peak, with a positive base-to-apex pressure difference driving the acceleration, and a reversed difference the deceleration of flow. In all cases, the reversed pressure difference was higher than the forward gradient, but did not exceed 2 mmHg. As P1 was the only patient with a visible A-wave peak in the flow curve, it is also the only patient with a second positive and reversed pressure difference in late diastole. The right panels of Fig. 8.3 display the viscous energy dissipation. The trend

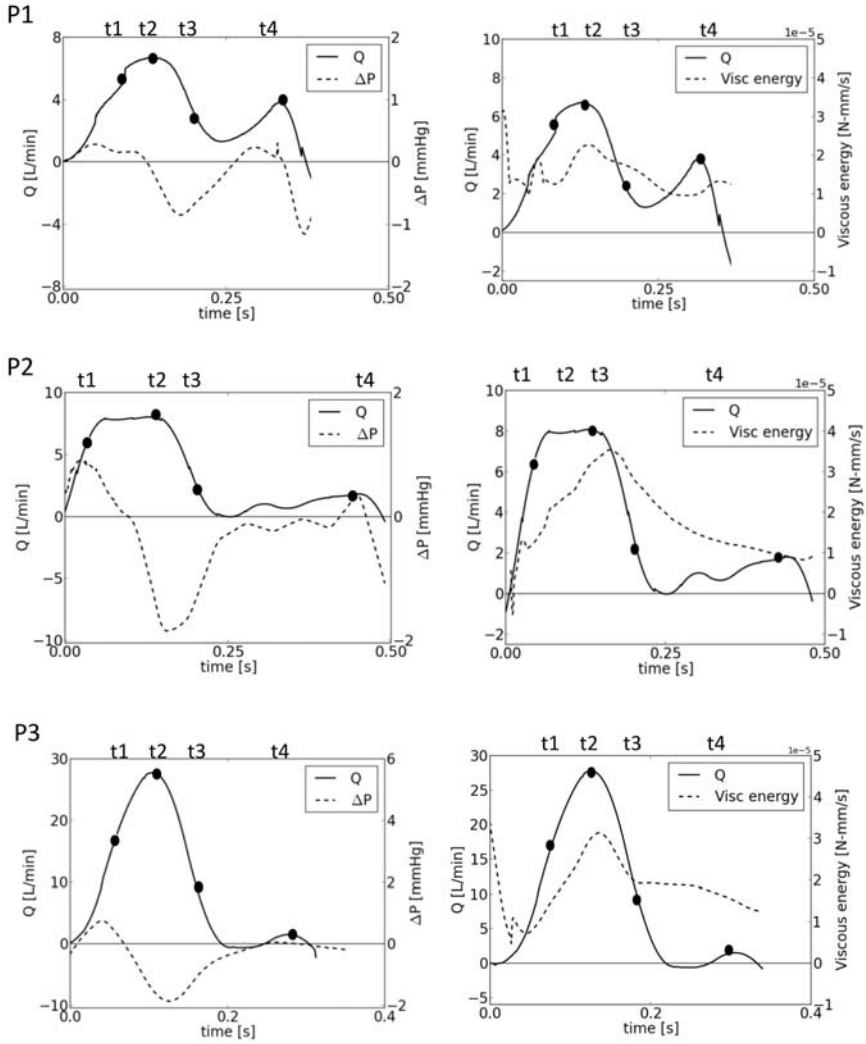

Figure 8.3: Left panels: volume flow rate curve (solid line) calculated at the atrial inlet, and intraventricular pressure difference, calculated as the difference of the average pressure between the average pressure at cross sections 1 and 2 (CS1 and CS2) of Fig. 8.1. Right panels: volume flow rate curve (solid line) and viscous energy dissipation

is consistent in the three patients, with a prominent peak during the deceleration phase.

Figure 8.4 displays the intraventricular velocity vectors and the pressure map during diastole for the three patients. Four significant time-points were selected, i.e. acceleration, peak of early filling (E-peak), deceleration, and peak of atrial filling (A-peak, if any). The

locations of the time-points are visually indicated in Fig. 8.3. Data are displayed in section plane S1 (Fig. 8.1).

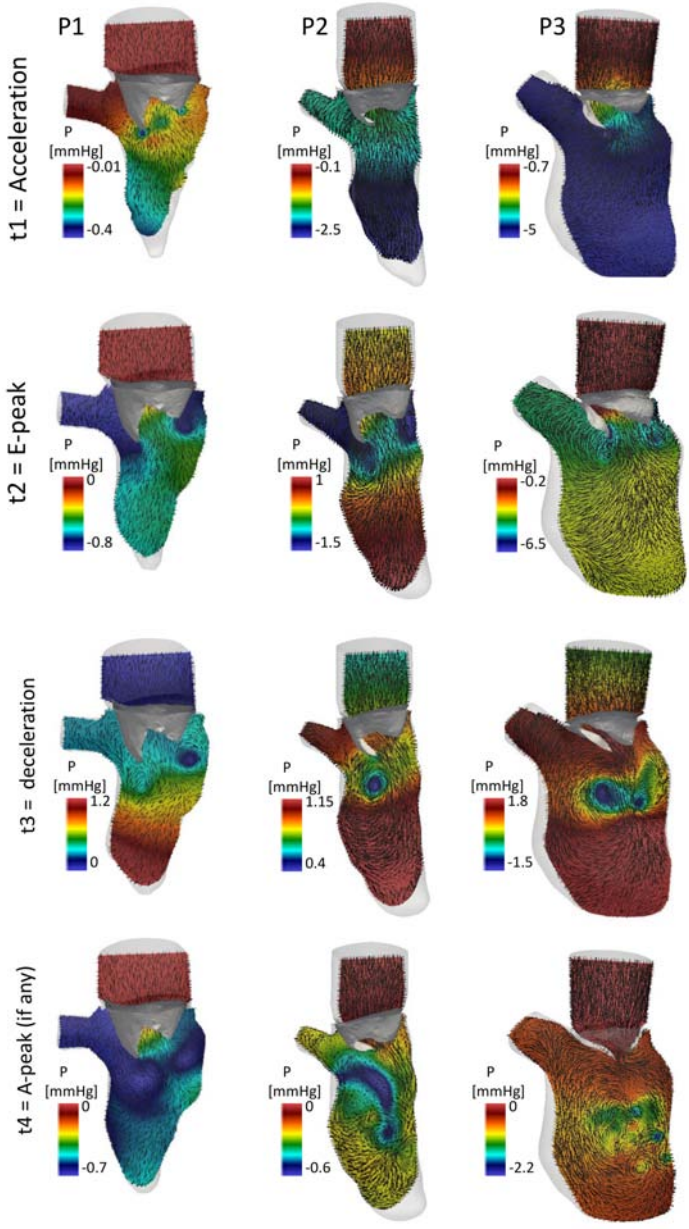

Figure 8.4: Intraventricular flow on a 2D slice and pressure variations (section S1 indicated in fig. 8.1) at four relevant time-points. Note that the scale of the pressure changes in each panel.

During the acceleration phase, in the three subjects, the flow is driven into the LV. At peak filling, the recirculation of the blood becomes an important feature, especially for P1 and P2, in whom the rotational flow structures arising from the edges of the MV are asymmetric and correspond with lower pressure values. The asymmetry is due to the presence of the asymmetric valvular leaflets. In P3 this feature is less evident, due to its larger geometry and more restricted leaflet motion. The deceleration phase enlarged the rotational flow structures, which travelled further and transported blood towards the apical regions of the LV. In this phase, the inversion of the pressure difference between the apical and the basal portion of the LV is visible in the three patients, causing the deceleration of the flow. The deceleration phase also corresponds to lower pressure zones in the central area of the LV below the valve, which are related to the presence of a vortex and recirculation flow path. The extension of this region varies from patient to patient. At the end of diastole, in P1 a second peak is detected in both the flow curve and in the presence of a spatially extended region of low pressures in the LV. However, the presence of an additional rotational flow is not clearly visible. In the remaining two patients the flow field becomes more chaotic and the vortical flows loose intensity.

8.3.3 Vortex analysis

The vortex structures are quite different in the three cases (Fig. 8.5).

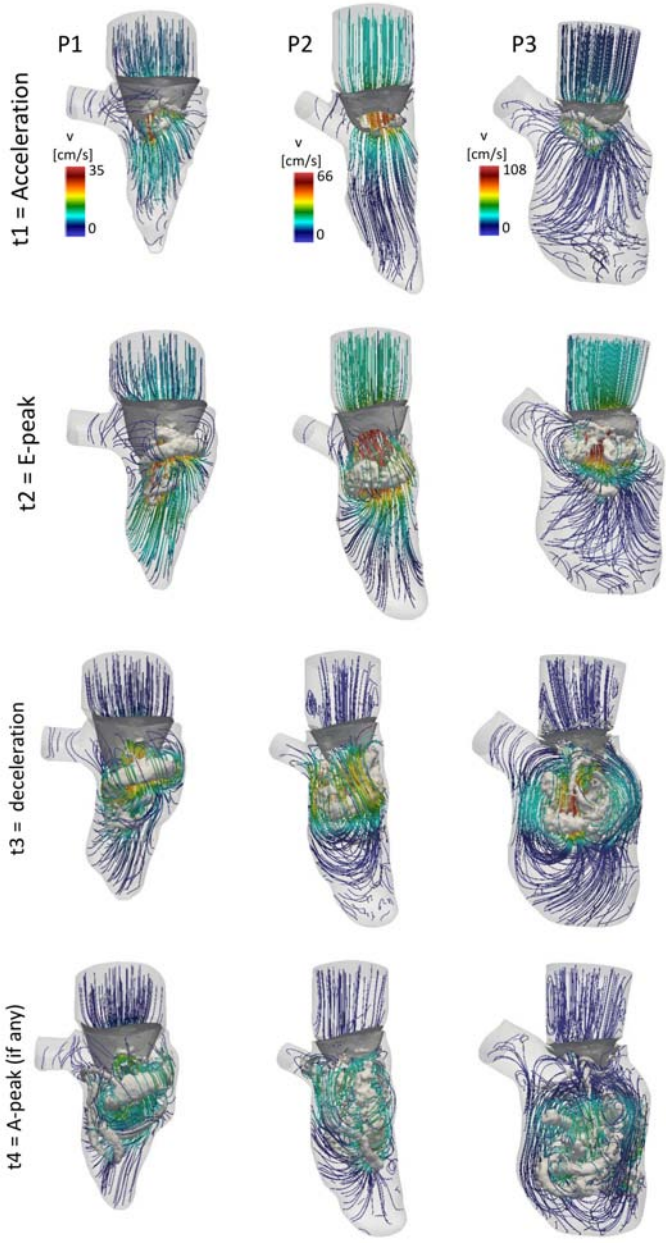

Figure 8.5: Intraventricular vortex visualization (λ_2) and velocity streamlines at four relevant time-points.

In P1 and P2, in early diastole (acceleration) a vortex structure originates in the proximity of the valvular edges (Fig. 8.5). In P3 the vortex of the early diastole is broader than for the other subjects. At

peak mitral inflow (Fig. 8.5, t2), in all the cases the vortex structure has increased its dimensions and occupies a larger portion in the LV. The spatial configuration of the vortex is influenced by the shape of the valvular leaflets: the vortices of P1 and P2 have a saddle-like shape dictated by the valve shape and assume an inclination of about 45 degrees with respect to the vertical plane of the LV when migrating to the apex, while the poorly motile valve of P3 is not able to orient the vortex ring, which remains almost horizontal. During the deceleration phase (Fig. 8.5, t3), the vortices detach from the valvular edge and migrate to more apical regions of the LV. In P1 and P2, the main vortex impacts the anterolateral and lateral ventricular walls, respectively. Due to the impact with the wall, the vortex of P2 twists and it starts dissipating (Fig. 8.4, t3). The motion of the vortex of P1 is less intense and the flow is more organized due to lower velocities. In contrast, the P3 vortex does not impact the dilated LV, therefore it migrates further and it shows secondary structures similar to the trailing vortex tubes reported in [40].

The velocity streamline directions are defined by the motion of the valve in the three cases. In P1, the velocity magnitude shows two maximum peaks in correspondence to the E- and A-peak of the transmitral flow. Due to the different dimensions of the three LVs, the peak velocities differ. In each case, the maximum velocity at E-peak is in agreement with the peak velocity estimated during the surgical procedure with pulsed Doppler.

8.3.4 WSS at wall

The wall shear stresses at E-peak are reported in Fig. 8.6.

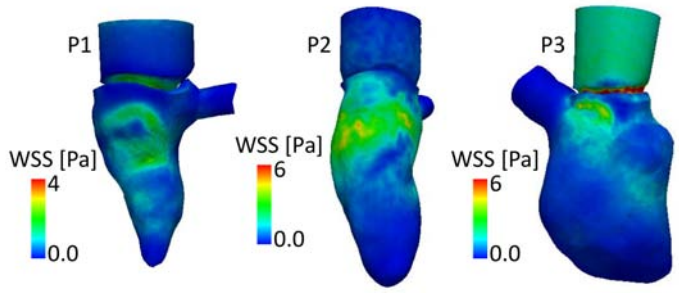

Figure 8.6: Wall shear stress for the three patients. Note that the geometries have been rotated differently, such that the area of highest WSS values is shown in each case.

At E-peak, high WSS values are located on the valvular leaflets (atrial side) and in the basal part of the LV due to the peak of velocity and the vortex formation in this region. During the entire diastole, the areas with higher values of WSS are located in correspondence of the vortex, which depends on the entering jet, the valvular shape and the ventricular shape, resulting in a WSS distribution highly dependent on the patient-specific details of the model. The WSS on the valvular leaflets are not reported here. In P1 and P2 the high values of WSS are located near the free edge of the posterior leaflet, while for P3 the area of high WSS is more distributed over the leaflets as the valve is less motile and has an higher hydraulic resistance.

8.4 Discussion

8.4.1 Clinical considerations

In this work, the comparison of three different clinical cases with the developed computational tool allowed to detect the profound differences that exist between the intraventricular flow fields in patients with different cardiac pathologies. Even though the numerical simulation is an indirect technique to obtain the flow field, the studied cases indicate that pathology-related flow features are consistent with literature data. P1, suffering from aortic stenosis, shows hypokinesis of parts of the ventricular walls, has a preserved EF and a double-peaked-shaped transmitral flow. However, the small geometric dimensions and abnormal motility of the walls do not allow for the development of an important vortex structure and high velocity jet. The dilated ventricle of P3 offers interesting insights into the hemodynamics of dilated cardiomyopathy. As documented in [128], the vortex structure in a dilated LV is broader than in a normal LV as it does not immediately impact the ventricular walls. The larger and persistent vortex structure is more able to transfer the blood to the apical regions of the LV, facilitating transport and ameliorating convective pressure losses, to partially compensate the negative effects of the pathology. Coherent with these findings, the vortex structures of P3 are larger and more persistent during diastole than for the other two patients. In the case of P3, the valve has a less evident influence on the flow field compared with P1 and P2. The limited motion of the leaflets does not orient the direction of the entering blood jet towards the wall of the LV and is not able to push the vortex structures to the apical regions of the LV. During the deceleration phase (t3 and t4) the vortex features are comparable to the cases reported in literature in which no valve is included in the model [40]. The presence of the

dilated ventricle, furthermore, does not allow the vortex to impact on the walls and consequently its dissipation. Due to the absence of the A-peak vortex formation, no considerations can be made on the interaction of the first and second vortices.

Despite the presence of diastolic dysfunction, the inlet flow jet produced a vortex ring in the three patients. The formation of the vortex, its initial growth and the maximum strength reached seem not to be dependent on the size of the ventricle, but only on the diameter and the shape of the valvular orifice, which is consistent with the results obtained by Stewart et al. [129]. After the pinch-off of the vortex from the valvular edges, the evolution of the vortex depends on the ventricular walls, whose position and dimensions determine the impact zone (if any) and the possibility of expansion or dissipation of the vortex [128] [129]. The pressures in the ventricles are strictly connected to the vortex formation and small variations in the pressure gradients influence the velocity field and rotational flow. The correspondence of the pressure distribution and the areas where the vortex is located is in good agreement with the results reported by [130]. Local variations in the ventricular pressures are related to the vortex formation and efficiency of the heart [95] and the availability of pressure maps in the ventricle provides pressure information otherwise not easily measurable in the LV due to the invasiveness of these measurements. Both the shape and magnitude of the intraventricular pressure difference curves in the three cases are comparable to the invasively measured data reported in [95]. The intraventricular pressure differences are lower in P1, despite the fact that the ejection fraction is preserved in this patient. We speculate that it is the slower rate of relaxation in P1, compared to P2, that reduces the intraventricular pressure difference in P1.

The trends of the energy dissipation (Fig. 8.3, lower panels) are consistent in the three patients, with a prominent peak during the early deceleration phase of the blood. The values are lowest in P1, consistent with the visual observation (t3 in figure 8.5) that the vortex breakdown is more noticeable in P2 and P3 than in P1. Compared to the work of Pedrizzetti et al. [123], the peak of dissipated energy occurs earlier in our cases. We speculate that this is due to the presence of the valve in our simulations (the valve was not modeled as a 3D object in [123]), forcing the vortex into a lower position into the LV and consequently an earlier impact (and dissipation) on the ventricular walls.

The WSS patterns at the ventricular walls are highly dependent on the patient-specific geometry details. In the three patients the region

of high WSS in the ventricle is always located in correspondence of the vortex structure.

8.4.2 Methodological considerations

The methodology used for the CFD simulations shows several advantages over existing works, with in particular (i) the use of clinically available rt-TEE ultrasound images as the source of the motion and (ii) the direct incorporation of the patient's 3D valve in the simulations. As shown before, the presence of the MV leaflets in the simulations is crucial, as the leaflets direct the flow and shape the vortex. A correct representation of the valvular apparatus is therefore mandatory to reproduce all features of intraventricular flow field, as verified in chapter 7.3.4 [6] [111].

The presented model has been successfully tested on three different patients, with abnormal ventricular functions and valvular performances, allowing for the comparison of the flow field. In this perspective, after validation, the presented model can be regarded as a tool to predict the hemodynamic conditions of a certain geometry.

8.4.3 Limitations

Despite its aforementioned advantages over other approaches, it is clear that our methodology also suffers from limitations. The main limitations are reported in chapter 7.4.4. On the imaging side, a major limitation is the temporal resolution of rt-TEE. As such, the model cannot provide any useful information on the timing of the cardiac cycle events. For example, no isovolumetric phases are included and the motion of the valve could be limited by the acquisition frequency. The geometries used in this work are patient-specific but do not include details such as papillary muscles and trabeculae, which have an impact on the flow field [115]. In addition to the modeling hypothesis and assumptions (e.g. Newtonian fluid, required time interpolation), the creation of the model relies on user-dependent tasks, especially in the preprocessing phase to generate the input for the simulation. It is mandatory to automate some of the processing steps before the model can be more extensively used in a clinical context for medical applications. As this work was focused on the diastolic phase, only a portion of the cardiac cycle was simulated. The analysis of the influence of simulating only the diastolic phase instead of the complete cardiac cycle is reported in appendix C. Future work will encompass the complete cardiac cycle.

8.5 Conclusions

In this chapter we comparatively studied the intraventricular flow field in three patients with various LV pathologies, making use of patient-specific 3D CFD models derived from clinical 3D ultrasound data. Our results indicate that the morphological changes due to the pathology influence the intraventricular dynamics, producing different patterns in each case. The availability of pressure gradient maps provides important information otherwise not available from clinical measurements. Of particular interest is the dilated ventricle case, in which the limited valve motility and the enlarged ventricle produced a significantly different scenario compared to P1 and P2. The main findings are in agreement with the clinical reports of the subjects and with clinical data on the same patient category.

IV

Conclusions

CHAPTER 9

Conclusions and future perspectives

A final overview on the major findings and achievements of this dissertation is provided here, followed by an outlook on the future perspectives of both FSI on aortic valves and CFD models to study intraventricular flows.

9.1 Conclusions

9.1.1 FSI simulation on aortic valves

FSI simulations on aortic valves have already been performed for decades and the developed models have become increasingly complex and realistic. Nevertheless, assumptions are still made to simplify the modeled scenario and/or to improve the performance of the numerical simulation, which need to be verified to ensure the reliability of the simulated case.

As discussed in chapter 4, both the proposed methods have specific problems in a 3D set-up. The ALE simulation faces significant problems related to the mesh motion and, even in the hypothesis of a good mesh motion management, the computing time is extremely high. The use of an IB method for the FSI simulation of valves is clearly more affordable in terms of computer power and has chances of success, as demonstrated by the increasing number of scientific

publications available on the topic. Unfortunately, in this work, using a commercially available solver (Abaqus/CEL release 12.0, Dassault Systèmes, Providence, RI, USA) to solve the 3D motion of an aortic valve, results were not convincing (in 3D), showing delayed valvular kinematics and an anomalous volume-of-fluid definition during the closing phase. Despite the fact that our study provided important insights into the possibilities and limitations of the tested solver, it was not possible to take a formal position and come to a generic conclusion regarding the IB based technique.

9.1.2 CFD simulation of intraventricular flows

Of interest in this part is the generation of CFD models with patient-specific features, which allow to study the cardiac hemodynamics in cardiomyopathies and the effects of the mitral valve apparatus.
The advantages of the described approach are multiple: as it is a CFD simulation and the motion of the boundaries is known a priori, no calculation of the interaction with the cardiac and valvular walls is required, nor precedent knowledge of the electro-mechanical properties of the ventricle. For this study, the fruitful collaboration with the Gorman Cardiovascular Research group (University of Pennsylvania, Philadelphia, PA) resulted in the availability of segmentations of the LV and MV which were used as input for the model. The use of 3D rt-TEE ultrasound images as a starting point provides an excellent spatial resolution, allowing for the segmentation of both the 3D mitral valve and left ventricle. In addition, this imaging technique is bed-side, fast, non-ionizing and does not require any contrast agent. With a widespread availability of scanners and data, different pathologies can be studied and compared. At the same time, rt-TEE also has disadvantages, such as the presence of noise (if compared to MRI or CT images), the relatively limited temporal resolution and possible limitations to the acquired field of view, especially in the case of dilated ventricles.

As the image sets used in this work were pre-operative acquisitions, the results show the clinical portrait of the diseased heart. We found the proposed method to be robust and ready to be applied to other settings. However, at the same time we do not consider the model to be fully validated. Mainly due to time restrictions, it was possible to verify the model over only a few test cases and compare the results with available literature, but a full validation is mandatory.

9.2 Recommendations and Future perspectives

9.2.1 FSI simulation of aortic valves

The current status of the tested software did not allow to reach a final conclusion on the FSI problem of heart valves. Nonetheless, this portion of the PhD allowed to acquire knowledge and awareness about the steps that have to be taken before and during the realization of an FSI model of valves (listed below), to increase the chances of success and to obtain an adequate result.

- If there is a need of analyzing valvular stresses on the leaflets and localize areas of high and low values of WSS (to detect for example regions prone to physical damages or analyze interface forces), or the pressure field in the aortic root, the use of an ALE-based approach is recommended [62]. These quantities are often not sufficiently accurate with a regular IB approach. Concerning the software choice, in our experience, the issues of the ALE-FSI method described in chapter 4 are mostly related to the mesh deformation automatically managed in Fluent. One of the options to circumvent this issue could be to implement a user-defined management of the mesh deformation, instead of relying of the automatic tools available in Fluent. Not many details are provided about the implementation of ALE-FSI simulations of aortic valves documented in Cao et al. [61], but we assume that currently the commercial software ANSYS (used in this work) can handle the ALE-FSI simulation of heart valves.

- If the interest is not the analysis of the pressures in the vicinitiy of the valve nor valvular stresses, the IB approach could be used. If the scope of the research is, for example, the impact of valvular pathologies on coronary flows (such as in Nobari et al. [52]), the IB approach should not alter the reliability of the results. However, particular care has to be used in the interpretation of the results.
  According to the available literature, the choice of the software mainly depends on the software availability and on the flexibility which is required by the solver. Among the advantages of using an in-house solver, there is the possibility to tailor it to the needs of the case of interest. The use of a commercial software, on the contrary, comes with all the benefits of a (presumed) verified and validated solver, technical guide and support which can significantly help in the simulation process. However, in

our case, the module CEL of Abaqus does not yet seem to be adequate for FSI simulations of heart valves.

9.2.2 CFD simulations with prescribed moving boundary

The described image-based CFD model is based on a number of modeling assumptions, which have been briefly mentioned in chapter 7.4.4 and 8.4.3. In this paragraph, we recall the most important assumptions introduced in our model and indicate the direction of future efforts to ameliorate it.

- Geometrical simplifications: the inclusion of anatomical details of the endocardial wall, such as trabeculae and papillary muscles have an impact on the ventricular fluid dynamics [115] [126], especially in the vortex dissipation, and therefore should be included in the model. However, the ALE implementation of more complex ventricular structures could have a negative effect on the final outcome of the simulation in terms of mesh deformation and distortion.

  In the work of Schenkel et al. [29] the authors show the influence of the upstream boundary conditions on the intraventricular flow field. Even though in our case this influence could be limited by the presence of the 3D valve, tests on the influence of different upstream boundary conditions should be performed.

- Newtonian fluid: even though the blood can be considered to behave as a Newtonian fluid in the large arteries and in the heart chambers as a first approximation, the blood can reach extremely low velocity values in the ventricle, especially in the apex, where the blood is more prone to stagnation. In these regions, the Newtonian fluid assumption made in this work might be no longer fully valid [29] [131] and more adequate rheological models should be investigated [127].

- Periodic solution: the use of a periodic solution is a good-practice procedure to eliminate the influence of the initialization, as such, more than one cardiac cycle should be simulated and the results of the converged simulation should be reported. The comparison proposed in appendix C highlights the (limited) influence that the systolic phase has on the subsequent diastole, for the analysis of the large-scale phenomena in the case of interest. However, the recent study of Chnafa et al. [126] showed the

importance of simulating several cardiac cycles to detect disturbed flow and high frequency flow components (>200Hz), with beat-to-beat differences which are in agreement with in vivo results [132]. The proposed model has an extremely refined computational mesh (10 million elements), a fourth-order non-dissipative numerical scheme and simulated 35 cardiac cycles. The analysis detected large velocity fluctuations in the entire LV, which are the result of the non-linearity of the flow equations, since the computational domain and boundary conditions are fully periodic.

This study [126] and the considerations proposed in appendix C suggest that for the detection of large-scale flow features the hypothesis adopted in our model can be acceptable and provide reliable results. For in-depth analysis of small-scale phenomena, such as fluctuations and cycle-to-cycle differences, a significantly more refined computational grid should be adopted and the numerical dissipation of the solver should be taken into account, as it could spuriously damp or eliminate the energy fluctuations in the LV. Furthermore, the simulation of multiple cardiac cycles will account for transitional phenomena and will include the influence of the previous heart beat in the results.

- Validation: the CFD model for the study of intraventricular flows has been tested in a few cases, but requires a full validation against experimental data. A 3D set-up of a simplified ventricle has been developed within a collaboration between our research group and Campus Schoonmeersen (Ghent University) and the 3D PIV acquisition of the flow field on a simplified set-up performed. For the computational model, the patient-specific geometry and motion can be replaced by the geometry and motion measured in the experimental set-up and the flow field compared for validation.

  Additionally, validation against in vivo measurements is fundamental to verify the reliability of the numerical tool. Due to time restrictions, it was not possible to obtain flow data (Doppler ultrasound or 4D MRI) of the patients in analysis. The availability of clinical flow/velocity measurements derived from relevant imaging methodologies will provide an in vivo validation of the developed tool. Furthermore, the acquisition of pre- and post-operative rt-TEE ultrasound images will allow to simulate the working conditions of the patient before and

after the intervention. The CFD model with prescribed moving boundaries of the mitral valve and left ventricle is the first step for future clinical implementations, where we particularly envision the model as a tool to predict the effect of intervention. With the availability of a higher number of test cases, both pre- and post-operative scans, it will be possible to generate a dataset of results with indications on the short-term effects of the surgical procedure.

9.3 Final remarks

In this work, we investigated several aspects of numerical simulations of moving heart valves and different techniques have been analyzed. Three goals have been defined in the introduction section of this thesis, to which this thesis aimed to provide a scientific answer.

1. *Evaluate the feasibility of the ALE technique for FSI simulations of blood flow through aortic valves and assess the impact of the modeling choices on the final results.*

   It is fundamental to analyze the problem under investigation and weigh the model according to the requirements of the project. Nowadays, performing 3D complex and multi-physics simulations on biological applications is a quite widespread practice. However, it is not always straightforward to assess the performance of the implemented model and the accuracy of the obtained solution. In this work we outlined the principal drawbacks and limitations encountered in our experience for FSI simulations on aortic valves and the advantages/disadvantages of two different techniques available to model the fluid domain.

2. *Develop a new technique for CFD simulations with prescribed moving boundaries based on patient-specific ultrasound images to study intraventricular hemodynamics.*

   The goal was successfully reached with the implementation of the model described in chapter 7. The model fulfills the imposed requirements, as it is patient-specific and based on rt-TEE ultrasound images. It relies on the ALE formulation for all the structures included (MV and LV). The prescribed motion of the boundaries resulted in a realistic set of boundary conditions for the analysis of the intraventricular flows. The preliminary analysis of the results provided expected and realistic results.

3. *Demonstrate the potential clinical use and relevance of such a model by testing it on patient-specific cases.*

   The presented model allowed us to simulate the intraventricular hemodynamics in three test cases, selected for their different cardiomyopathies. The diastolic intraventricular flow field was calculated from pre-operative clinical images, such that the obtained flow field could be compared to the clinical diagnostic portrait of the patient. The model provided the major flow features of the three different cases, such as intraventricular pressure field and quantitative details on vortex formation. This is the first step towards the verification and validation of the computational model and its possible future applications. However, we are still far from the applicability of the computational tool to the clinical practice, as validation against both in vitro experiments and flow visualization images is mandatory.

V

Appendices

Chapters

APPENDIX A

Pseudo-code for UDF.c

Algorithm 1: Initialization

```
   Data: Input files (spline coefficients)
1  foreach Input surface do
2  |  foreach Input points do
3  |  |  read the spline coefficients for the position of this input
   |  |    point as calculated in pyFormex;
4  |  end
5  end
```

Algorithm 2: Space Interpolation: find the nearest points on the input surface

```
1  foreach Moving computational surface do
2  |  foreach Face do
3  |  |  foreach Node do
4  |  |  |  calculate the distance with all the points (at time=t)
   |  |  |    of the corresponding input surface ;
5  |  |  |  identify the 5 nearest points of the corresponding
   |  |  |    input surface ;
6  |  |  |  store the IDs of these closest input points ;
7  |  |  end
8  |  end
9  end
```

Algorithm 3: Update of the Fluent Mesh

```
1  foreach Input surface do
2      foreach Input point do
3          update the position of this point using the spline
           coefficients stored in Fluent ;
4          calculate the displacement with respect to the previous
           time step ;
5      end
6  end
7  foreach Moving computational surface do
8      foreach Face do
9          foreach Node do
10             retrieve the 5 nearest input points stored in the
               space interpolation step ;
11             check the quality of the triangle formed by the
               nearest input points (select the 3 closest points
               which generate a not-skewed triangle) ;
12             project the node on this input triangle ;
13             calculate barycentric coordinates of projection ;
14             if projection is outside the triangle then
15                 force the projection of the Fluent point on the
                   closest edge or point of the input triangle ;
16             end
17             update the position of the Fluent point as linear
               combination of the displacements of the 3 closest
               input points ;
18         end
19     end
20 end
```

Algorithm 4: Contact detection

```
1  set thresholds for contact detection ;
2  foreach faces f1 which can possibly be in contact do
3  |  calculate the face normal ;
4  |  foreach Node n1 do
5  |  |  check distance of node (n1) from center of face (f1);
6  |  |  if projection of the node along its normal falls within the
   |  |   original face then
7  |  |  |  set flag for contact on the face (f1) ;
8  |  |  |  set flag for contact on the node (n1) ;
9  |  |  |  set flag for contact on the faces (f2) to whom the
   |  |  |   node n1 also belongs ;
10 |  |  end
11 |  end
12 end
```

Algorithm 5: Fill the gap

```
1  foreach computational surfaces of the valve do
2  |  foreach face do
3  |  |  retrieve the flags for contact ;
4  |  |  foreach cell neighboring the flagged faces do
5  |  |  |  set contact-flag in this cell ;
6  |  |  |  repeat
7  |  |  |  |  loop over the cells sharing one face with this
   |  |  |  |   contact-flagged cell ;
8  |  |  |  |  set contact-flag in this cell;
9  |  |  |  until wall is found or a max number of iterations is
   |  |  |   reached;
10 |  |  end
11 |  end
12 end
```

APPENDIX B

Grid sensitivity analysis

Referring to the model presented in chapter 7, a sensitivity analysis was performed, to identify the most suitable dimensions for the computational mesh. Four different meshes were generated (from 50K to 500K cells) and the dimensions are reported in table B.1. An identical simulation was performed for the 4 cases, coherent with the parameters and working conditions described in chapter 7.2. The computing time for each case is reported in table B.1. The time-step size was chosen for each simulation such that the mesh motion was always leading to a valid mesh (no inverted elements). The chosen time-step size was 1ms for the 50K, 100K and 160K cells, while a time-step size of 0.5ms was adopted for the 500K cells simulation.

Various performance indexes were evaluated and are reported in figure B.1. First, integral quantities over the entire domain were

Table B.1: Grid dimensions, time-step size and computing time

Average element number	**Time-step size**	**Computing time**
50K	1ms	5h
100K	1ms	8h
160K	1ms	12h
500K	0.5ms	5d

calculated. We report the average velocity (Fig. B.1a), the vorticity (Fig. B.1b) and the (viscous) energy dissipation (Fig. B.1c). The latter quantity is derived from the NS equation and the conservation of energy combined with the assumption of an homogeneous, incompressible, Newtonian and isotropic fluid [30] as:

$$\Phi = 2\mu[(\frac{\partial u}{\partial x})^2+(\frac{\partial v}{\partial y})^2+(\frac{\partial w}{\partial z})^2]+(\frac{\partial u}{\partial y}+\frac{\partial v}{\partial x})^2+(\frac{\partial u}{\partial z}+\frac{\partial w}{\partial x})^2+(\frac{\partial v}{\partial z}+\frac{\partial w}{\partial y})^2 \tag{B.1}$$

As a clinically relevant quantity, we report the intraventricular pressure difference (base – apex, surfaces location indicated as S1 and S2 in Fig. 7.1d) during the entire cycle (Fig. B.1d). As high values of wall shear stress could be indicators of damage on the ventricular walls or valvular leaflets, in Fig. B.1e we report the surface area of the LV and MV subjected to high shear values (calculated as the area with a WSS value higher than the 80% of the peak shear stress on the coarsest mesh). In Fig. B.1f the surface area of the vortex structures is reported for the four cases.

From Fig. B.1(a-d) no significant differences are visible in the global features of the flow field. The high peak visible in the viscous energy plot is due to the sudden closure of the aortic valve. The most significant differences are visible in Fig. B.1f, in which the surface of the vortex significantly increases with the degree of refinement of the mesh. Having a finer mesh, the vortex structure and vortex breakup is more represented and smaller flow features are captured by the simulations. Consistently, a larger region of high WSS is detected in more refined meshes especially during diastole, as the area close to the walls occupied by the vortex is larger (Fig. B.1e). As a visual example, we report the differences in the vortex structure in Fig. B.2 during the deceleration phase of diastole (t=0.65s), at which the vortex structure is the largest.

All grids capture the main vortex structure during diastole. However, only the more refined meshes can capture the secondary structures of the flow. For the results in chapter 7, the 500K cells mesh was selected. Given the small dimensions of the ventricle under investigation, for the 500K cells grid the average cell size is of 1.2 mm. The obtained grid is not uniform in space, as a more refined mesh is required in the neighborhood of the valve. The dimension of the cells (especially in the valvular region) is comparable to the size reported in Chnafa et al., 2014 [106] (0.8mm average value for an almost uniform

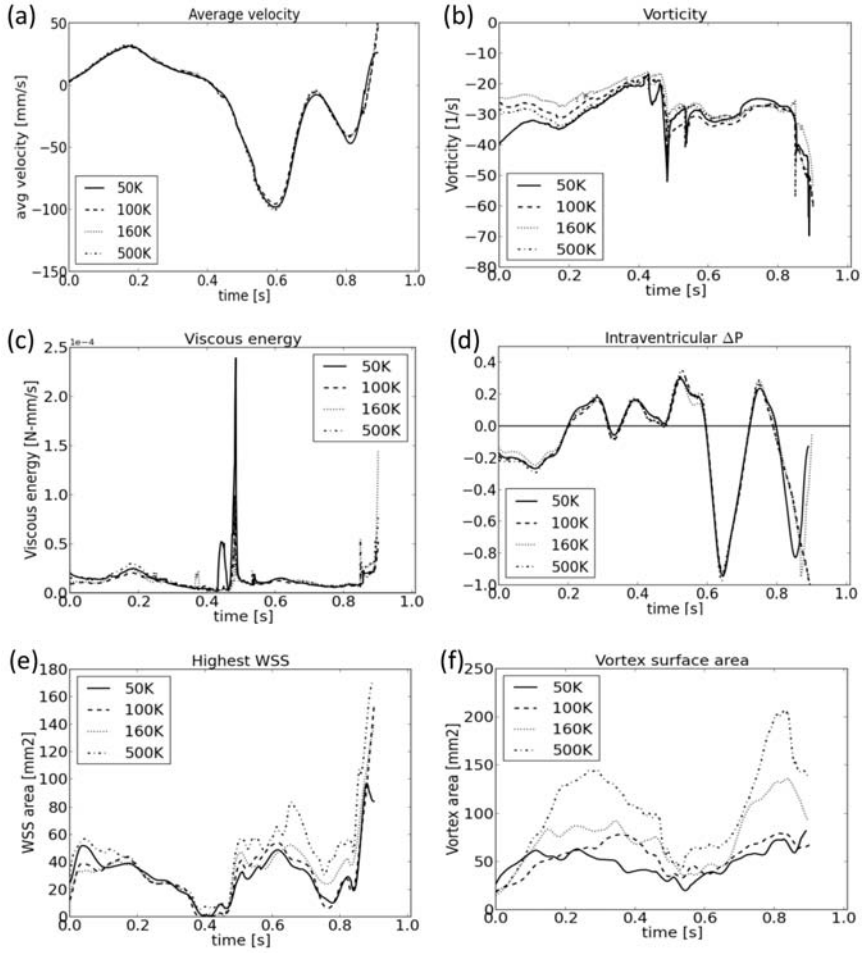

Figure B.1: (a) Average velocity, (b) vorticity, (c) viscous energy, (d) intraventricular pressure difference, (e) surface area of highest WSS values, (f) surface area of vortex structures in the four different meshes.

grid) for the entire and physiological left heart including the atrium and the vessels.

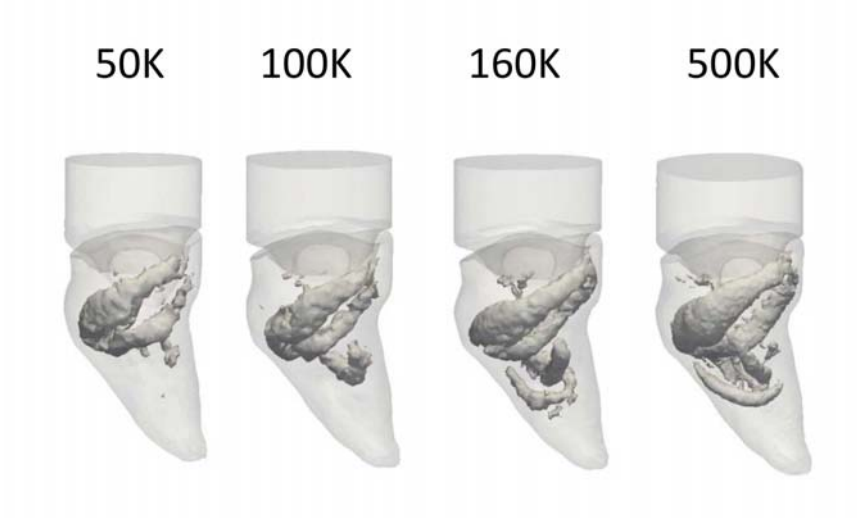

Figure B.2: Vortex structures in the 4 analyzed cases during deceleration(t=0.65s).

APPENDIX C

Impact of simulating only diastole

The intraventricular flow is defined by the periodic beating of the heart and considering only part of a cycle from an initialized (to zero) state might have an impact on the simulated data. For P1 it was possible to simulate the entire cardiac cycle (chapter 7) as well as the diastolic phase only (chapter 8), which allows for a direct assessment of the impact of considering the diastolic phase alone. A comparison of the most relevant results is reported here, to investigate how simulating of part of the cycle affects the results. All other numerical settings (mesh, boundary conditions) were identical.

In Fig. C.1, the curves of mitral inflow (at the inlet), intraventricular pressure difference ($p_{apex} - p_{base}$, with respect to the planes CS1 and CS2 of Fig. 8.1) and the viscous energy dissipation (calculated with equation B.1) are reported. For the full-cycle simulation (solid line), both systole and diastole are reported, while for the simulation limited to the diastolic phase only this section is reported (dotted line). The diastolic phase is highlighted in Fig. C.1.

In the flow curve, a limited difference is detected from the beginning of diastole until the E-peak. This difference is due to the spline interpolation used to obtain the motion of the LV and MV. In fact, in the full-cycle simulation the splines at the beginning of diastole are influenced by the last frames of the systolic phase, while this effect is

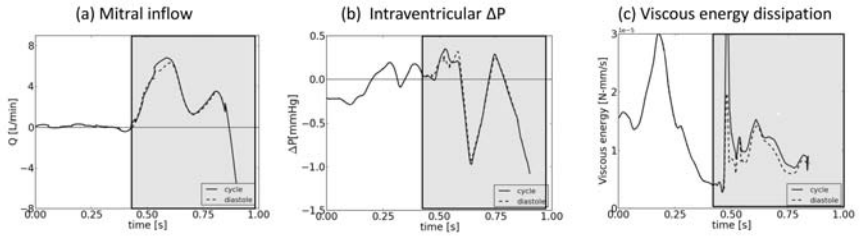

Figure C.1: Comparison of (a) mitral inflow, (b) intraventricular pressures and (c) viscous energy dissipation in the full-cycle and in the diastolic simulations.

not present in the splines used for the simulation of the diastole only. After the E-peak, the two curves are superimposed, as the splines curves used in the two cases are no longer influenced by the systole. Similarly, the intraventricular pressure difference curve shows small differences at early diastole, but the magnitude, trend and overall behavior is consistent. From E-peak until the end of diastole the two curves are superimposed. Larger differences are visible in the energy dissipation curve, where the full-cycle simulation curve shows larger values than the diastolic simulation curve.

A visual comparison of the pressures on the S1 section (location reported in Fig. 8.1) is proposed in Fig. C.2. Results are reported for early diastole, E-peak and deceleration phase. This qualitative comparison does not reveal important differences between the two cases, consistent with the intraventricular pressure curve reported in Fig. C.1.

The comparison of the vortex structures is reported in Fig. C.3. In the early diastolic phase, larger vortex structures are present in the full-cycle simulation, especially in the region of the aortic outlet. This result is expected, as in the full-cycle case residual systolic vortex formations are still present in the LV at the beginning of diastole (see Fig. 7.6). The shape of the vortex is quite comparable in the two cases, even though in the full-cycle simulation the structure assumes more complex shapes than in the case limited to the diastole. In the full-cycle simulation, even though the net flow field is almost zero at the beginning of diastole (<0.03L/min at inlet), the blood has some residual motion from the systolic phase and residual systolic vortex structures still present can interact with the diastolic vortex (local v_{max} in the LV of 0.5m/s in the vicinity of the valvular leaflets).

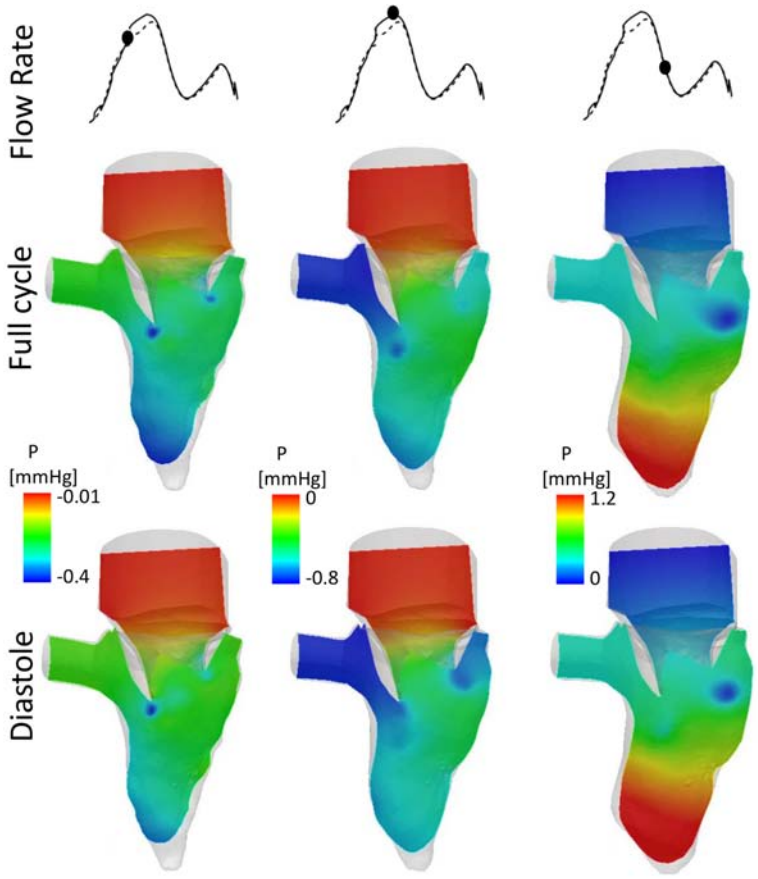

Figure C.2: Comparison of the pressure distribution on a vertical section in the full-cycle and in the diastolic simulations.

We hypothesize that the difference in the vortex shape and the global viscous energy curve is related to the interaction of the diastolic flow features (i.e. the diastolic vortex) with the pre-existing systolic vortical structures in the ventricle, which are obviously not detected in the simulation limited to the diastolic phase, as the entire flow field is initialized to zero at the beginning of diastole.

Nevertheless, the differences found between the two types of simulation are, at least for the analyzed case, not very significant and mainly related to the spline interpolation required by the methodology. The diastolic phase can be considered, in good approximation, as decoupled from the previous systolic phase, as the latter has a limited fluid-dynamic influence on the diastolic flow field. This statement

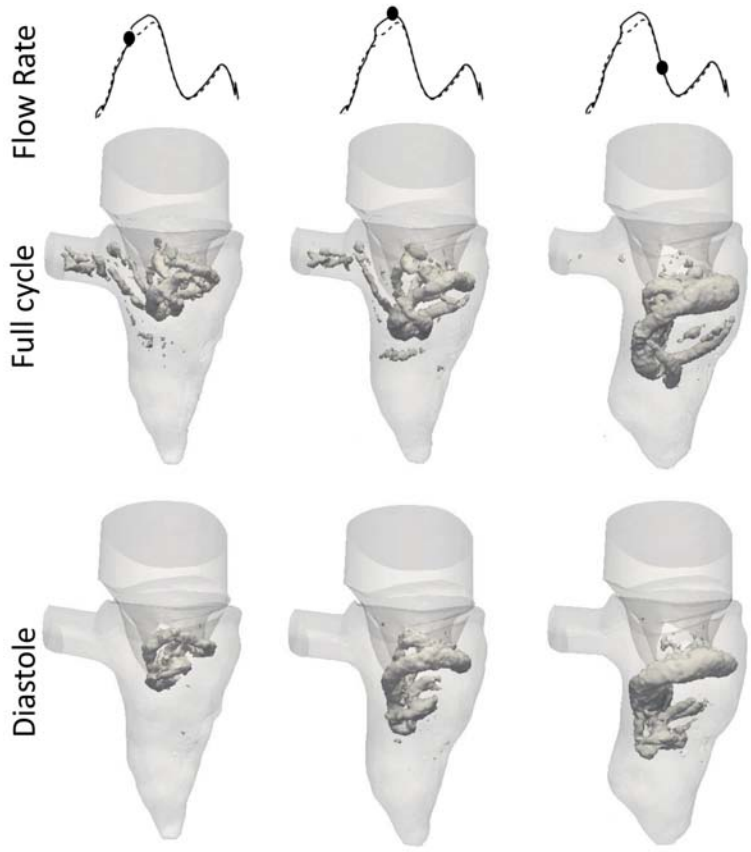

Figure C.3: Comparison of the vortex structures in the ventricle in the full-cycle and in the diastolic simulations.

is not necessarily true for the systole, as it was not possible to test the full sequence diastole-systole with our model, as it is currently implemented.

List of Figures

List of Tables

Bibliography

[1] C. M. Otto, 'Timing of aortic valve surgery.' *Heart (British Cardiac Society)*, vol. 84, no. 2, pp. 211–8, 2000.

[2] B. Stewart, D. Siscovick, B. K. Lind, J. M. Gardin, J. S. Gottdiener, V. E. Smith, D. W. Kitzman and C. M. Otto, 'Clinical Factors Associated With Calcific Aortic Valve Disease', *Journal of the American College of Cardiology*, vol. 29, no. 3, pp. 630–634, 1997.

[3] A. Yoganathan, Z. He and S. Casey Jones, 'Fluid Mechanics of Heart Valves', *Annual Review of Biomedical Engineering*, vol. 6, no. August, pp. 331–362, 2004.

[4] A. Cribier, H. Eltchaninoff, A. Bash, N. Borenstein, C. Tron, F. Bauer, G. Derumeaux, F. Anselme, F. Laborde and M. B. Leon, 'Percutaneous transcatheter implantation of an aortic valve prosthesis for calcific aortic stenosis: First human case description', *Circulation*, vol. 106, no. 24, pp. 3006–3008, 2002.

[5] A. M. Bavo, G. Rocatello, F. Iannaccone, J. Degroote, J. Vierendeels and P. Segers, 'Fluid-Structure Interaction Simulation of Prosthetic Aortic Valves: Comparison between Immersed Boundary and Arbitrary Lagrangian-Eulerian Techniques for the Mesh Representation', *Plos One*, vol. 11, no. 4, e0154517, 2016.

[6] A. M. Bavo, A. M. Pouch, J. Degroote, J. Vierendeels, J. H. Gorman, R. C. Gorman and P. Segers, 'Patient-specific CFD simulation of intraventricular haemodynamics based on 3D ultrasound imaging', *BioMedical Engineering OnLine*, vol. 15, no. 1, p. 107, 2016.

[7] A. M. Bavo, A. M. Pouch, J. Degroote, J. Vierendeels, J. H. Gorman, R. C. Gorman and P. Segers, 'Patient-specific CFD models for intraventricular flow analysis from 3D ultrasound imaging : comparison of three clinical cases', *Journal of Biomechanics*, 2016.

[8] Guyton and Hall, 'Textbook of Medical Physiology', 11th Editi. Philadelphia, PA: Elsevier Inc., 2006.

[9] M. J. Underwood, G. E. Khoury, D. Deronck, D. Glineur and R. Dion, 'The aortic root: structure, function, and surgical reconstruction', *Heart*, vol. 83, pp. 376–380, 2000.

[10] R. H. Anderson, 'Clinical anatomy of the aortic root.' *Heart (British Cardiac Society)*, vol. 84, no. 6, pp. 670–673, 2000.

[11] G. J. Tortora and B. Derrickson, 'Principles of Anatomy and Physiology', 13th editi. John Wiley & Sons, Inc., 2012.

[12] J. P. Dal Blanco and R. A. Levine, 'Anatomy of the Mitral Valve Apparatus - Role of 2D and 3D Echocardiography', *Cardiology Clinics*, vol. 31, no. 2, pp. 1–23, 2013.

[13] L. J. Spreeuwers, S. J. Bangma, R. J. H. W. Meerwaldt, E. J. Vonken and M. Breeuwer, 'Detection of trabeculae and papillary muscles in cardiac MR images', *Computers in Cardiology*, vol. 32, pp. 415–418, 2005.

[14] T. Claessens, 'Model-Based Quantification of Systolic and Diastolic Left Ventricular Mechanics', PhD thesis, Ghent University.

[15] R. Rhoades and J. Tanner, 'Medical Physiology', Fourth ed. Lippincott Williams and Wilkins, 2013.

[16] *www.allinahealth.org/Health-conditions-and-treatments/.*

[17] *Www.summitmedicalgroup.com/library/adult_health/car_artificial_heart_valves.*

[18] A. Kulik, P. Bedard, B. K. Lam, F. D. Rubens, P. J. Hendry, R. G. Masters, T. G. Mesana and M. Ruel, 'Mechanical versus bioprosthetic valve replacement in middle-aged patients', *European Journal of Cardio-thoracic Surgery*, vol. 30, no. 3, pp. 485–491, 2006.

[19] V. T. Nkomo, J. M. Gardin, T. N. Skelton, J. S. Gottdiener, C. G. Scott and M. Enriquez-Sarano, 'Burden of valvular heart diseases: a population-based study', *Lancet*, vol. 368, no. 9540, pp. 1005–1011, 2006.

[20] B. Iung and A. Vahanian, 'Epidemiology of acquired valvular heart disease', *Canadian Journal of Cardiology*, vol. 30, no. 9, pp. 962–970, 2014.

[21] J. J. Thaden, V. T. Nkomo and M. Enriquez-Sarano, 'The Global Burden of Aortic Stenosis', *Progress in Cardiovascular Diseases*, vol. 56, no. 6, pp. 565–571, 2014.

[22] H. Sisakian, 'Cardiomyopathies: Evolution of pathogenesis concepts and potential for new therapies.' *World journal of cardiology*, vol. 6, no. 6, pp. 478–94, 2014.

[23] *Www.merkmanuals.com.*

[24] D. Phelan, G. R. Wilson, P. A. James and P. J. Lockhart, 'The genetics of cardiomyopathy , new technologies and the path to personalised medicine', *OA Genetics*, vol. 01, no. 1, pp. 1–9, 2013.

[25] J. Donea, A. Huerta, J. Ponthot and A. Rodriguez-Ferran, 'Arbitrary Lagrangian–Eulerian Methods', in *Encyclopedia of Computational Mechanics*, E. Stein, R. de Borst and T.J.R. Hughes, Wiley & sons, 2004, ch. 14, Chapter 14, Vol. 1.

[26] J. Degroote, 'Partitioned Simulations of Fluid-Structure Interaction', *Arch Comput Methods Eng*, vol. 20, pp. 185–238, 2013.

[27] A. Quarteroni and L. Formaggia, 'Mathematical Modelling and Numerical Simulation of the Cardiovascular System', in *Modelling of Living Systems, Handbook of Numerical Analysis Series*, P. Ciarlet and J. Lions, Eds., Amsterdam: Elsevier, 2004, pp. 3–127.

[28] D. Katritsis, L. Kaiktsis, A. Chaniotis, J. Pantos, E. P. Efstathopoulos and V. Marmarelis, 'Wall Shear Stress: Theoretical Considerations and Methods of Measurement', *Progress in Cardiovascular Diseases*, vol. 49, no. 5, pp. 307–329, 2007.

[29] T. Schenkel, M. Malve, M. Reik, M. Markl, B. Jung and H. Oertel, 'MRI-Based CFD analysis of flow in a human left ventricle: Methodology and application to a healthy heart', *Annals of Biomedical Engineering*, vol. 37, no. 3, pp. 503–515, 2009.

[30] H. K. Versteeg and W. Malalasekera, 'An Introduction to Computational Fluid Dynamics, the Finite Volume Method', II edition. Harlow, Essex, England: Pearson Education Limited, 2007.

[31] 'Ansys Inc.15.0, ANSYS Fluent User guide'. Canonsburg, PA, USA.

[32] Q. Long, R. Merrifield, X. Y. Xu, P. Kilner, D. N. Firmin and Y. G-Z, 'Subject-specific computational simulation of left ventricular flow based on magnetic resonance imaging.' *Proceedings of the Institution of Mechanical Engineers. Part H, Journal of engineering in medicine*, vol. 222, no. 4, pp. 475–485, 2008.

[33] C. S. Peskin, 'Flow patterns around heart valves: A numerical method', *Journal of Computational Physics*, vol. 10, no. 2, pp. 252–271, 1972.

[34] R. Glowinski, T. W. Pan and J. Periaux, 'A Lagrange multiplier / fictitious domain method for the numerical simulation of incompressible viscous flow around moving rigid bodies : (I) case where the rigid body motions are known a priori', *Mathematical Problems in Mechanics*, vol. 1, pp. 361–369, 1997.

[35] F. P. T. Baaijens, 'A fictitious domain / mortar element method for fluid – structure interaction', *International Journal for Numerical Methods in Fluids*, vol. 36, no. May 1999, pp. 743–761, 2001.

[36] I. Borazjani, 'Fluid-structure interaction, immersed boundary-finite element method simulations of bio-prosthetic heart valves', *Computer Methods in Applied Mechanics and Engineering*, vol. 257, pp. 103–116, 2013.

[37] R. van Loon, P. D. Anderson, J. de Hart and F. P. T. Baaijens, 'A combined fictitious domain/adaptive meshing method for fluid-structure interaction in heart valves', *International Journal for Numerical Methods in Fluids*, vol. 46, no. 5, pp. 533–544, 2004.

[38] A. Gilmanov and F. Sotiropoulos, 'A hybrid Cartesian/immersed boundary method for simulating flows with 3D, geometrically complex, moving bodies', *Journal of Computational Physics*, vol. 207, no. 2, pp. 457–492, 2005.

[39] L. Ge and F. Sotiropoulos, 'A numerical method for solving the 3D unsteady incompressiblge Navies-Stokes equations in curvilinear domains with complex immersed boundaries', *Journal of Computational Physics*, vol. 225, no. 2, pp. 1782–1809, 2007.

[40] T. B. Le and F. Sotiropulos, 'On the Three-Dimensional vortical structure of early diastolic flow in a patient-specific left ventricle', *European Journal of Mechanics B Fluids*, vol. 35, pp. 20–24, 2012.

[41] R. Mittal, H. Dong, M. Bozkurttas, F. Najjar, A. Vargas and A. von Loebbecke, 'A Versatile Sharp Interface Immersed Boundary Method for Incompressible Flows With Complex Boundaries', *Journal of Computational Physics*, vol. 227, no. 10, pp. 4825–4852, 2008.

[42] W. A. Wall, P. Gamnitzer and A. Gerstenberger, 'Fluid-structure interaction approaches on fixed grids based on two different domain decomposition ideas', *International Journal of Computational Fluid Dynamics*, vol. 22, no. 6, pp. 411–427, 2008.

[43] J. Degroote, A. Swillens, P. Bruggeman, R. Haelterman, P. Segers and J. Vierendeels, 'Simulation of fluid-structure interaction with the interface artificial compressibility method', *International journal for numerical methods in biomedical engineering*, vol. 26, pp. 276–289, 2010.

[44] A. M. Pouch, H. Wang, M. Takabe, B. M. Jackson, J. H. Gorman, R. C. Gorman, P. A. Yushkevich and C. M. Sehgal, 'Fully automatic segmentation of the mitral leaflets in 3D transesophageal echocardiographic images using multi-atlas joint label fusion and deformable medial modeling', *Medical Image Analysis*, vol. 18, no. 1, pp. 118–129, 2014.

[45] J. Degroote, K. J. Bathe and J. Vierendeels, 'Performance of a new partitioned procedure versus a monolithic procedure in fluid-structure interaction', *Computers and Structures*, vol. 87, no. 11-12, pp. 793–801, 2009.

[46] P. Segers, L. Taelman, J. Degroote, J. Bols and J. Vierendeels, 'The aortic reservoir-wave as a paradigm for artedial haemodynamics: insights from the fluid-structure interaction simulations in a model of aortic coarctation', *Journal of Hypertension*, vol. 33, no. 3, pp. 554–63, 20015.

[47] L. Taelman, J. Degroote, P. Verdonck, J. Vierendeels and P. Segers, 'Modeling hemodynamics in vascular networks using a geometrical multiscale approach: Numerical aspects', *Annals of Biomedical Engineering*, vol. 41, no. 7, pp. 1445–1458, 2013.

[48] 'Abaqus documentation'. Dassault Systemes, Providence, RI, USA.

[49] J. Peiro and S. Sherwin, 'Finite Difference, Finite Element and Finite Volume Methods for Partial Differential Equations', in *Handbook of Material Modeling*, S. Yip, Ed., Dordrecht: Springer Netherlands, 2005, pp. 2415–2446.

[50] J. A. Gravel, 'Surgical treatment of aortic insufficiency.' *Canadian Medical Association journal*, vol. 72, no. 8, pp. 599–601, 1955.

[51] B. E. Griffith, 'Immersed boundary model of aortic heart valve dynamics with physiological driving and loading conditions', *International Journal for Numerical Methods in Biomedical Engineering*, vol. 00, no. 1, pp. 1–29, 2011.

[52] S. Nobari, R. Mongrain, R. Leask and R. Cartier, 'The effect of aortic wall and aortic leaflet stiffening on coronary hemodynamic: A fluid-structure interaction study', *Medical and Biological Engineering and Computing*, 2013.

[53] F. Sturla, E. Votta, M. Stevanella, C. A. Conti and A. Redaelli, 'Impact of modeling fluid-structure interaction in the computational analysis of aortic root biomechanics', *Medical Engineering and Physics*, vol. 35, no. 12, pp. 1721–1730, 2013.

[54] G. Marom, H. S. Kim, M. Rosenfeld, E. Raanani and R. Haj-Ali, 'Fully coupled fluid-structure interaction model of congenital bicuspid aortic valves: Effect of asymmetry on hemodynamics', *Medical and Biological Engineering and Computing*, vol. 51, no. 8, pp. 839–848, 2013.

[55] N. Diniz dos Santos, J. F. Gerbeau and J. F. Bourgat, 'A partitioned fluid-structure algorithm for elastic thin valves with contact', *Computer Methods in Applied Mechanics and Engineering*, vol. 197, no. 19-20, pp. 1750–1761, 2008.

[56] J. De Hart, G. W. M. Peters, P. J. G. Schreurs and F. P. T. Baaijens, 'A three-dimensional computational analysis of fluid-structure interaction in the aortic valve', *Journal of Biomechanics*, vol. 36, no. 1, pp. 103–112, 2003.

[57] W. Wu, D. Pott, B. Mazza, T. Sironi, E. Dordoni, C. Chiastra, L. Petrini, G. Pennati, G. Dubini, U. Steinseifer, S. Sonntag, M. Kuetting and F. Migliavacca, 'Fluid–Structure Interaction Model of a Percutaneous Aortic Valve: Comparison with an In Vitro Test and Feasibility Study in a Patient-Specific Case', *Annals of Biomedical Engineering*, vol. 44, no. 2, pp. 590–603, 2016.

[58] P. Sucosky, K. Balachandran, A. Elhammali, H. JO and A. Yoganathan, 'Altered shear stress stimulated upregulation of endothelial VCAM-1 and ICAM-1 in a BMP-4- and TGF-beta1-dependent pathway.' *Arteriosclerosis, Thrombosis and Vascular Biology*, vol. 29, no. 2, pp. 254–260, 2009.

[59] R. van Loon, P. D. Anderson and F. N. van de Vosse, 'A fluid-structure interaction method with solid-rigid contact for heart valve dynamics', *Journal of Computational Physics*, vol. 217, no. 2, pp. 806–823, 2006.

[60] S. Chandra, N. M. Rajamannan and P. Sucosky, 'Computational assessment of bicuspid aortic valve wall-shear stress: Implications for calcific aortic valve disease', *Biomechanics and Modeling in Mechanobiology*, vol. 11, no. 7, pp. 1085–1096, 2012.

[61] K. Cao, M. BukaČ and P. Sucosky, 'Three-dimensional macro-scale assessment of regional and temporal wall shear stress characteristics on aortic valve leaflets', *Computer Methods in Biomechanics and Biomedical Engineering*, pp. 1–11, 2015.

[62] R. van Loon, P. D. Anderson, F. N. van de Vosse and S. J. Sherwin, 'Comparison of various fluid-structure interaction methods for deformable bodies', *Computers and Structures*, vol. 85, no. 11-14, pp. 833–843, 2007.

[63] M. Astorino, J. F. Gerbeau, O. Pantz and K. F. Traoré, 'Fluid-structure interaction and multi-body contact: Application to aortic valves', *Computer Methods in Applied Mechanics and Engineering*, vol. 198, no. 45-46, pp. 3603–3612, 2009.

[64] J. De Hart, G. W. M. Peters, P. J. G. Schreurs and F. P. T. Baaijens, 'A two-dimensional fluid-structure interaction model of the aortic value', *Journal of Biomechanics*, vol. 33, no. 9, pp. 1079–1088, 2000.

[65] R. Van Loon, P. D. Anderson, F. P. T. Baaijens and F. N. Van De Vosse, 'A three-dimensional fluid-structure interaction method for heart valve modelling', *Comptes Rendus - Mecanique*, vol. 333, no. 12, pp. 856–866, 2005.

[66] P. Crosetto, P. Reymond, S. Deparis, D. Kontaxakis, N. Stergiopulos and A. Quarteroni, 'Fluid-structure interaction simulation of aortic blood flow', *Computers and Fluids*, vol. 43, no. 1, pp. 46–57, 2011.

[67] E. J. Weinberg, P. J. MacK, F. J. Schoen, G. García-Cardeña and M. R. Kaazempur Mofrad, 'Hemodynamic Environments from Opposing Sides of Human Aortic Valve Leaflets Evoke Distinct Endothelial Phenotypes in Vitro', *Cardiovascular Engineering*, vol. 10, no. 1, pp. 5–11, 2010.

[68] H. Reul, V. A, G. M, S.-R. Th, H. V and E. S, 'The geometry of the aortic root in health, at valve distease and after valve replacement', *Journal of Biomechanics*, vol. 23, no. 2, pp. 181–191, 1990.

[69] S. Annerel, J. Degroote, T. Claessens, S. K. Dahl, B. Skallerud, L. R. Hellevik, P. Van Ransbeeck, P. Segers, P. Verdonck and J. Vierendeels, 'A fast strong coupling algorithm for the partitioned fluid–structure interaction simulation of BMHVs', *Computer Methods in Biomechanics and Biomedical Engineering*, vol. 15, no. 12, pp. 1281–1312, 2012.

[70] J. A. Stella, J. Liao and M. S. Sacks, 'Time-dependent biaxial mechanical behavior of the aortic heart valve leaflet', *Journal of Biomechanics*, vol. 40, no. 14, pp. 3169–3177, 2007.

[71] H. Mohammadi, F. Bahramian and W. Wan, 'Advanced modeling strategy for the analysis of heart valve leaflet tissue mechanics using high-order finite element method.' *Medical engineering & physics*, vol. 31, no. 9, pp. 1110–1117, 2009.

[72] K. S. Kunzelman, D. R. Einstein and R. P. Cochran, 'Fluid-structure interaction models of the mitral valve: function in normal and pathological states.' *Philosophical transactions of the Royal Society of London. Series B, Biological sciences*, vol. 362, no. 1484, pp. 1393–1406, 2007.

[73] L. Taelman, 'Fluid-structure interaction simulation of (repaired) aortic coarctation', PhD thesis, Ghent University, 2015.

[74] P. Wriggers, J. Schröder and A. Schwarz, 'A finite element method for contact using a third medium', *Computational Mechanics*, vol. 52, no. 4, pp. 837–847, 2013.

[75] K. D. Lau, V. Diaz-Zuccarini, P. Scambler and G. Burriesci, 'Fluid-structure interaction study of the edge-to-edge repair technique on the mitral valve', *Journal of Biomechanics*, vol. 44, no. 13, pp. 2409–2417, 2011.

[76] H. Kim, J. Lu, M. S. Sacks and K. B. Chandran, 'Dynamic simulation of bioprosthetic heart valves using a stress resultant shell model', *Annals of Biomedical Engineering*, vol. 36, no. 2, pp. 262–275, 2008.

[77] P. N. Jermihov, L. Jia, M. S. Sacks, R. C. Gorman, J. H. Gorman and K. B. Chandran, 'Effect of Geometry on the Leaflet Stresses in Simulated Models of Congenital Bicuspid Aortic Valves', *Cardiovascular Engineering and Technology*, vol. 2, no. 1, pp. 48–56, 2011.

[78] R. Gnyaneshwar, R. K. Kumar and K. R. Balakrishnan, 'Dynamic analysis of the aortic valve using a finite element model', *The Annals of thoracic surgery*, vol. 73, no. 4, pp. 1122–9, 2002.

[79] G. Rocatello, 'Fluid-Structure Interaction Simulation of aortic valves: from a 2D towards a 3D case', Master thesis, Politecnico di Milano, 2015.

[80] I. K. Dumont, 'Experimental and numerical modeling of heart valve dynamics', PhD thesis, Ghent University, 2005.

[81] S. Annerel, 'Numerical Simulation of Aortic Bileaflet Mechanical Heart Valves', PhD thesis, Ghent University, 2012.

[82] F. Bakhtiary, O. Dzemali, U. Steinseiffer, C. Schmitz, B. Glasmacher, A. Moritz and P. Kleine, 'Opening and closing kinematics of fresh and calcified aortic valve prostheses: An in vitro study', *Journal of Thoracic and Cardiovascular Surgery*, vol. 134, no. 3, pp. 657–662, 2007.

[83] P. Kleine, F. Bakhtiary, O. Dzemali, U. Steinseifer, C. Schmitz, B. Glasmacher and A. Moritz, 'Hemodynamic performance and leaflet kinematics of porcine versus pericardial aortic valve prostheses', *The Thoracic and Cardiovascular Surgeon*, vol. 55, no. S 1, p. 967 361, 2007.

[84] R. G. Leyh, C. Schmidtke, H. H. Sievers and M. H. Yacoub, 'Opening and closing characteristics of the aortic valve after different types of valve-preserving surgery.' *Circulation*, vol. 100, no. 21, pp. 2153–2160, 1999.

[85] J. Melorose, R. Perroy and S. Careas, 'Handbook of Cardiac anatomy, physiology and devices', P. A. Iaizzo, Ed. Springer, 2009, vol. 1.

[86] P. Martinez-Legazpi, J. Bermejo, Y. Benito, R. Yotti, C. Perez Del Villar, A. Gonzalez-Mansilla, A. Barrio, E. Villacorta, P. L. Sanchez, F. Fernandez-Aviles and J. C. Del Alamo, 'Contribution of the diastolic vortex ring to left ventricular filling', *Journal of the American College of Cardiology*, vol. 64, no. 16, pp. 1711–1721, 2014.

[87] P. P. Sengupta, G. Pedrizzetti, P. J. Kilner, A. Kheradvar, T. Ebbers, G. Tonti, A. G. Fraser and J. Narula, 'Emerging trends in CV flow visualization', *JACC: Cardiovascular Imaging*, vol. 5, no. 3, pp. 305–316, 2012.

[88] M. Gharib, E. Rambod, A. Kheradvar, D. J. Sahn and J. O. Dabiri, 'Optimal vortex formation as an index of cardiac health.' *Proceedings of the National Academy of Sciences of the United States of America*, vol. 103, no. 16, pp. 6305–6308, 2006.

[89] G. Pedrizzetti and F. Domenichini, 'Left Ventricular Fluid Mechanics: The Long Way from Theoretical Models to Clinical Applications', *Annals of Biomedical Engineering*, vol. 43, no. 1, pp. 26–40, 2014.

[90] G. Pedrizzetti, A. R. Martiniello, V. Bianchi, A. D'Onofrio, P. Caso and G. Tonti, 'Cardiac fluid dynamics anticipates heart adaptation', *Journal of Biomechanics*, vol. 48, no. 2, pp. 388–391, 2015.

[91] R. Mittal, J. H. Seo, V. Vedula, Y. J. Choi, H. Liu, H. H. Huang, S. Jain, L. Younes, T. Abraham and R. T. George, 'Computational modeling of cardiac hemodynamics: Current status and future outlook', *Journal of Computational Physics*, vol. 305, pp. 1065–1082, 2016.

[92] T. B. Le, F. Sotiropoulos, D. Coffey and D. Keefe, 'Vortex formation and instability in the left ventricle', *Physics of Fluids*, vol. 24, no. 9, pp. 2–3, 2012.

[93] P. J. Kilner, G. Z. Yang, A. J. Wilkes, R. H. Mohiaddin, D. N. Firmin and M. H. Yacoub, 'Asymmetric redirection of flow through the heart.' *Nature*, vol. 404, no. 6779, pp. 759–61, 2000.

[94] G. Pedrizzetti and F. Domenichini, 'Nature optimizes the swirling flow in the human left ventricle', *Physical Review Letters*, vol. 95, no. 10, pp. 1–4, 2005.

[95] N. L. Greenberg, P. M. Vandervoort, M. S. Firstenberg, M. J. Garcia and J. D. Thomas, 'Estimation of diastolic intraventricular pressure gradients by Doppler M-mode echocardiography.' *American journal of physiology. Heart and circulatory physiology*, vol. 280, no. 6, H2507–15, 2001.

[96] K. C. Stewart, R. Kumar, J. J. Charonko, T. Ohara, P. P. Vlachos and W. C. Little, 'Evaluation of LV diastolic function from color M-mode echocardiography', *JACC: Cardiovascular Imaging*, vol. 4, no. 1, pp. 37–46, 2011.

[97] M. M. Redfield, S. J. Jacobsen, J. C. Burnett, D. W. Mahoney, K. R. Bailey and R. J. Rodeheffer, 'Burden of Systolic and Diastolic Ventricular', *Internal Medicine*, vol. 289, no. 2, pp. 194–202, 2003.

[98] I. Borazjani, J. Westerdale, E. M. McMahon, P. K. Rajaraman, J. J. Heys and M. Belohlavek, 'Left ventricular flow analysis: recent advances in numerical methods and applications in cardiac ultrasound.' *Computational and mathematical methods in medicine*, vol. 15, no. 2, p. 395 081, 2012.

[99] *Http://heartsite.com/html/tee.html*.

[100] M. Handke, G. Heinrichs, U. Moser, F. Hirt, F. Margadant, F. Gattiker, C. Bode and A. Geibel, 'Transesophageal Real-Time Three-Dimensional Echocardiography. Methods and Initial In Vitro and Human In Vivo Studies', *Journal of the American College of Cardiology*, vol. 48, no. 10, pp. 2070–2076, 2006.

[101] A. Vegas and M. Meineri, 'Three-dimensional transesophageal echocardiography is a major advance for intraoperative clinical management of patients undergoing cardiac surgery: A core review', *Anesthesia and Analgesia*, vol. 110, no. 6, pp. 1548–1573, 2010.

[102] M. McCormick, D. A. Nordsletten, D. Kay and N. P. Smith, 'Simulating left ventricular fluid-solid mechanics through the cardiac cycle under LVAD support', *Journal of Computational Physics*, vol. 244, pp. 80–96, 2013.

[103] B. Baccani, F. Domenichini and G. Pedrizzetti, 'Model and influence of mitral valve opening during the left ventricular filling', *Journal of Biomechanics*, vol. 36, no. 3, pp. 355–361, 2003.

[104] J. J. Shi, M. Alenezy, I. V. Smirnova and M. Bilgen, 'Construction of a two-parameter empirical model of left ventricle wall motion using cardiac tagged magnetic resonance imaging data', *BioMedical Engineering OnLine*, vol. 11, no. 1, p. 1, 2012.

[105] H. Watanabe, S. Sugiura, H. Kafuku and T. Hisada, 'Multiphysics simulation of left ventricular filling dynamics using fluid-structure interaction finite element method.' *Biophysical Journal*, vol. 87, no. 3, pp. 2074–2085, 2004.

[106] C. Chnafa, S. Mendez and F. Nicoud, 'Image-based large-eddy simulation in a realistic left heart', *Computers and Fluids*, vol. 94, pp. 173–187, 2014.

[107] N. R. Saber, N. B. Wood, A. D. Gosman, R. D. Merrifield, G. Z. Yang, C. L. Charrier, P. D. Gatehouse and D. N. Firmin, 'Progress towards patient-specific computational flow modeling of the left heart via combination of magnetic resonance imaging with computational fluid dynamics', *Annals of Biomedical Engineering*, vol. 31, no. 1, pp. 42–52, 2003.

[108] B. Baillargeon, N. Rebelo, D. D. Fox, R. L. Taylor and E. Kuhl, 'The living heart project: A robust and integrative simulator for human heart function', *European Journal of Mechanics, A/Solids*, vol. 48, no. 1, pp. 38–47, 2014.

[109] Y. J. Choi, J. Constantino, V. Vedula, N. Trayanova and R. Mittal, 'A New MRI-Based Model of Heart Function with Coupled Hemodynamics and Application to Normal and Diseased Canine Left Ventricles.' *Frontiers in bioengineering and biotechnology*, vol. 3, no. September, p. 140, 2015.

[110] V. Mihalef, R. I. Ionasec, P. Sharma, B. Georgescu, I. Voigt, M. Suehling and D. Comaniciu, 'Patient-specific modelling of whole heart anatomy, dynamics and haemodynamics from four-dimensional cardiac CT images', *Interface Focus*, vol. 1, no. 3, pp. 286–296, 2011.

[111] J. H. Seo, V. Vedula, T. Abraham, A. C. Lardo, F. Dawoud, H. Luo and R. Mittal, 'Effect of the mitral valve on diastolic flow patterns', *Physics of Fluids*, vol. 26, no. 12, 2014.

[112] T. Doenst, K. Spiegel, M. Reik, M. Markl, J. Hennig, S. Nitzsche, F. Beyersdorf and H. Oertel, 'Fluid-Dynamic Modeling of the Human Left Ventricle: Methodology and Application to Surgical Ventricular Reconstruction', *Annals of Thoracic Surgery*, vol. 87, no. 4, pp. 1187–1195, 2009.

[113] B. Griffith, X. Luo, D. McQueen and C. Peskin, 'Simulating the fluid dynamics of natural and prosthetic heart valves using the immersed boundary method', *International Journal of Applied Mechanics*, vol. 1, no. 1, pp. 137–177, 2009.

[114] F. Domenichini and G. Pedrizzetti, 'Asymptotic Model of Fluid-Tissue Interaction for Mitral Valve Dynamics', *Cardiovascular Engineering and Technology*, vol. 6, no. 2, pp. 95–104, 2015.

[115] V. Vedula, J. H. Seo, A. C. Lardo and R. Mittal, 'Effect of trabeculae and papillary muscles on the hemodynamics of the left ventricle', *Theoretical and Computational Fluid Dynamics*, vol. 30, no. 1-2, pp. 3–21, 2016.

[116] A. Lopez-Perez, R. Sebastian and J. M. Ferrero, 'Three-dimensional cardiac computational modelling: methods, features and applications', *BioMedical Engineering OnLine*, vol. 14, no. 1, p. 35, 2015.

[117] P. A. Yushkevich, H. Zhang and J. C. Gee, 'Continuous medial representation for anatomical structures', *IEEE Transactions on Medical Imaging*, vol. 25, no. 12, pp. 1547–1564, 2006.

[118] B. Avants, C. Epstein, M. Crossman and J. Gee, 'Symmetric diffeomorphic image registration with cross-correlation: evaluating automated labeling of elderly and neurodegenerative brain', *Medical Image Analysis Journal*, vol. 12, pp. 26–41, 2008.

[119] E. Votta, T. B. Le, M. Stevanella, L. Fusini, E. G. Caiani, A. Redaelli and F. Sotiropoulos, 'Toward patient-specific simulations of cardiac valves: State-of-the-art and future directions', *Journal of Biomechanics*, vol. 46, no. 2, pp. 217–228, 2013.

[120] W. Heidrich, 'Computing the Barycentric Coordinates of a Projected Point', *Journal of Graphics, GPU, and Game Tools*, vol. 10, no. 3, pp. 9–12, 2005.

[121] J. Vande Voorde, 'Numerical flow calculations in rotary positive-displacement machines', PhD thesis, Ghent University, 2006.

[122] J. Jeong and F. Hussain, 'On the identification of a vortex', *Journal of Fluid Mechanics*, vol. 285, pp. 69–94, 1995.

[123] G. Pedrizzetti, F. Domenichini and G. Tonti, 'On the left ventricular vortex reversal after mitral valve replacement', *Annals of Biomedical Engineering*, vol. 38, no. 3, pp. 769–773, 2010.

[124] C. Q. Lai, G. L. Lim, M. Jamil, C. N. Z. Mattar, A. Biswas and C. H. Yap, 'Fluid mechanics of blood flow in human fetal left ventricles based on patient-specific 4D ultrasound scans', *Biomechanics and Modeling in Mechanobiology*, pp. 1–14, 2015.

[125] A. Pasipoularides, 'Evaluation of right and left ventricular diastolic filling', *Journal of Cardiovascular Translational Research*, vol. 6, no. 4, pp. 623–639, 2013.

[126] C. Chnafa, S. Mendez and F. Nicoud, 'Image-Based Simulations Show Important Flow Fluctuations in a Normal Left Ventricle: What Could be the Implications?', *Annals of Biomedical Engineering*, pp. 1–13, 2016.

[127] S. N. Doost, L. Zhong, B. Su and Y. S. Morsi, 'The numerical analysis of non-Newtonian blood flow in human patient-specific left ventricle', *Comput. Methods Programs Biomed*, vol. 7, pp. 232–247, 2016.

[128] J. Bermejo, Y. Benito, M. Alhama, R. Yotti, P. Martínez-Legazpi, C. Pérez Del Villar, E. Pérez-David, A. González-Mansilla, C. Santa-Marta, A. Barrio, F. Fernández-Avilés and J. C. Del Alamo, 'Intraventricular vortex properties in non-ischemic dilated cardiomyopathy.' *American journal of physiology. Heart and circulatory physiology*, pp. 718–729, 2014.

[129] K. C. Stewart, J. C. Charonko, C. L. Niebel, W. C. Little and P. P. Vlachos, 'Left ventricle filling vortex formation is unaffected by diastolic impairment', *AJP: Heart and Circulatory Physiology*, pp. 1255–1262, 2012.

[130] J. Vierendeels, K. Riemslagh, E. Dick and P. Verdonck, 'Computer Simulation of Intraventricular Flow and Pressure gradient during diastole', *Journal of Biomechanical Engineering*, vol. 122, no. December 2000, pp. 667–674, 2000.

[131] B. M. Johnston, P. R. Johnston, S. Corney and D. Kilpatrick, 'Non-Newtonian blood flow in human right coronary arteries: Transient simulations', *Journal of Biomechanics*, vol. 39, no. 6, pp. 1116–1128, 2006.

[132] J. Zajac, J. Eriksson, P. Dyverfeldt, A. F. Bolger, T. Ebbers and C. J. Carlhäll, 'Turbulent kinetic energy in normal and myopathic left ventricles', *Journal of Magnetic Resonance Imaging*, vol. 41, no. 4, pp. 1021–1029, 2015.